Canadian
Journal of Physics

Canadian Journal of Physics

PILE NEUTRON CAPTURE CROSS SECTIONS OF Co60* (10.5 MIN.) AND Co60 (5.25 YR.)[1]

BY F. BROWN, J. L. WOLFSON,
AND L. YAFFE[2]

ABSTRACT

Activity of approximately 105 min. half-life has been detected in samples of Co59 irradiated at high neutron fluxes in the NRX reactor. By a study of the yield as a function of neutron flux and time of irradiation this activity was demonstrated to be due to Co61 (105 min.) formed by neutron capture in Co60. The pile neutron capture cross sections were found to be 95 ± 45 barns and 6.0 ± 1.4 barns for the Co60* (10.5 min.) and Co60 (5.25 yr.) isomers respectively.

I. INTRODUCTION

In determinations of the thermal neutron capture cross section of Co59 (1, 3, 11, 14) it has been assumed that the thermal neutron capture cross sections of the Co60* (10.5 min.) (7) and Co60 (5.25 yr.) (12) isomers are negligibly small. Large values of the capture cross sections of these isomers would have a pronounced effect on the value for the Co59 capture cross section determined by either the activation method or the pile oscillator method. In the former case the value obtained would be spuriously low, and in the latter case spuriously high. The pile oscillator method might be expected to give a more reliable value since the neutron fluxes employed are usually low. The fact that the results obtained by both methods are in agreement provides some evidence that the Co60* (10.5 min.) and Co60 (5.25 yr.) capture cross sections are both small.

This conclusion is supported by the results of the present experiment, in which measurements have been made of the pile neutron capture cross sections of the two isomers for formation of Co61 (105 min.). The values obtained were 95 ± 45 barns and 6.0 ± 1.4 barns for the short and long lived Co60 isomers respectively.

These cross sections were determined from a study of the production of Co61 in Co59 samples irradiated in the NRX reactor, and information as to the disintegration of Co61 was therefore required. The half-life of Co61 has been measured by several observers and values reported ranging from 99 min. to 108 min. (6, 9, 10, 13). Parmley *et al.* (9) found the β-ray end point to be 1.3 ± 0.1 Mev. but detected no γ-rays. Smith *et al.* (13) found two groups of

---

β-rays and in addition detected a γ-ray of approximately 0.5 Mev. They conclude that Co^{61} decays by negative β-ray emission, 55% of energy 1.42 $\pm$ 0.02 Mev. to the ground state of Ni^{61}, and 45% of energy 1.00 $\pm$ 0.02 Mev. to an excited state in Ni^{61} at 0.42 Mev., followed by emission of a γ-ray of the same energy.

In the present work the half-life has been taken to be 105 min. since the data obtained agree best with this value. Nevertheless the data do not provide an accurate measure of the half-life and would not be inconsistent with a somewhat shorter or longer value. The errors assigned to the cross sections take into account the uncertainty in the lifetime. The disintegration scheme proposed by Smith et al. (13) has been adopted. Choice of a simple beta spectrum, as indicated by the results of Parmley et al. (9), would have the effect of reducing the measured values of the cross sections by about 10%.

II. APPARATUS AND METHOD

Samples of spectroscopically pure Co^{59} sponge or wire of known mass were irradiated in the "rabbit" of the Chalk River reactor for periods of time ranging from 1.5 to 12 hr. After irradiation, a sample was dissolved in nitric acid, made up to a known volume, and an accurately measured aliquot deposited on thin aluminum foil. The nitric acid was evaporated under heat to leave a thin layer of the nitrate about 1 cm. in diameter and about 0.3 mgm./cm.² thick. The sample was then covered with a solution of polystyrene in benzene, which after drying left a thin covering layer about 0.1 mgm./cm.² thick.

The activity was counted with an anthracene scintillation spectrometer, consisting of a piece of anthracene approximately 1.3 cm. $\times$ 1.3 cm. $\times$ 0.3 cm. thick applied to the face of a 5819 photomultiplier with DC 200 silicone fluid. The anthracene was covered with an aluminum reflector 0.15 mgm./cm.² thick. The assembly was housed in a light-tight container with an aluminum window about 0.5 mgm./cm.² thick. The sources were placed 4 cm. above the window, resulting in an effective solid angle of about 0.9%.

The spectrometer was calibrated with a source of Cs^{137} (37 yr.) of known activity, using a single channel pulse height analyzer. The activity of the Cs^{137} source was determined by comparison with a standardized source which had been measured in a 4π proportional counter. The position of the 624 kev. line due to the internally converted 661.6 kev. γ-ray (8) provided the energy calibration. The intensity of the line, i.e. the integrated number of electrons per second counted in the line, along with the conversion coefficients (4) and β-branching ratio for Cs^{137} (5) gave the solid angle. Width of the conversion line was 15% at half maximum intensity.

A typical experiment involved calibration of the spectrometer, followed by replacement of the Cs^{137} source with the cobalt source. The lower discriminator of the pulse height analyzer was then set to a pulse height corresponding to 410 kev. and all pulses of heights larger than this were taken from the "integral" output of the analyzer and fed into a scaler. The output of the scaler was arranged to record pips every 1,000 or 10,000 counts, depending on counting rate, on the chart of an Esterline Angus recorder. Counts were

recorded in this manner for approximately 20 hr., after which the spectrometer was calibrated again to determine whether drifts in the electronic apparatus had altered the effective bias setting. Corrections were applied to the data where changes in the position of the Cs^{137} conversion line indicated bias changes larger than 1%. Fig. 1 illustrates the type of decay curve obtained.

The high background is due to the 1.17 and 1.33 Mev. γ-rays from Co^{60}. In addition there is the 1.56 Mev. β-ray transition of intensity 0.28% (2) from the 10.5 min. isomeric state in Co^{60}, which is detected in the initial period of counting. However the 320 kev. β-rays from the 5.25 yr. Co^{60} isomer are not counted since the discriminator was set to reject pulses of height lower than that corresponding to 410 kev. After subtraction of the background there remains a component with a half-life of roughly 105 min. In every case this component has been fitted with a line of slope corresponding to a half-life of exactly 105 min. This procedure assumes that the activity is due to Co^{61}. Justification for this assumption is given below. The fraction of the β-spectrum counted assuming the disintegration scheme of Smith *et al.* (13) is 53%.

In all, eight trials were made: one at an irradiation time of 1.54 hr., three at an irradiation time of 3 hr., one of which was done at reduced neutron flux, one at an irradiation time of 6 hr., and three at an irradiation time of 12 hr.

The amount of Co^{61} activity formed by successive neutron capture in Co^{59} is given in the following expression, for $\lambda_2 t \gg 1$:

$$[1] \quad \frac{\lambda_4 N_4}{\phi^2 N_1} = \sigma_{34} \left[(e^{-\lambda_4 t} - 1) \left(\frac{\sigma_{12}}{\lambda_2} + \frac{\sigma_{12} + \sigma_{13}}{\lambda_4} \right) - \frac{\sigma_{12}}{\lambda_2} \frac{\lambda_4}{(\lambda_4 - \lambda_2)} e^{-\lambda_4 t} \right.$$
$$\left. + (\sigma_{12} + \sigma_{13}) t \right] + \sigma_{24} \left[\frac{\sigma_{12}}{\lambda_2} (1 - e^{-\lambda_4 t}) + \sigma_{12} \frac{\lambda_4}{\lambda_2} \frac{e^{-\lambda_4 t}}{(\lambda_4 - \lambda_2)} \right]$$

where the subscripts 1, 2, 3, 4 refer respectively to Co^{59}, Co^{60*} (10.5 min.), Co^{60} (5.25 yr.), and Co^{61} (105 min.), and the other symbols have the following meaning:

> λ—disintegration constant (sec.$^{-1}$)
> t—time of irradiation (sec.)
> N—number of atoms present at time t
> ϕ—thermal neutron flux (cm.$^{-2}$ sec.$^{-1}$)

σ_{12} and σ_{13}—refer to the effective neutron capture cross sections of Co^{59} (at the position of the "rabbit" in the NRX reactor) to form the isomers Co^{60*} (10.5 min.) and Co^{60} (5.25 yr.) respectively. These are derived from the corresponding thermal neutron cross sections, σ_{12}' and σ_{13}', by the addition of terms to each which take into account the contribution to the activities by the capture of fast neutrons.

From other data it is estimated that approximately 2.5% of the total Co^{60} (5.25 yr.) activity produced (after decay of the 10.5 min. activity) is due to capture of epicadmium neutrons. This leads to a value of 35.1 barns for $(\sigma_{12} + \sigma_{13})$ using the value 34.2 barns (14) for the corresponding thermal neutron capture cross sections $(\sigma_{12}' + \sigma_{13}')$. It is however not known

how the difference of 0.9 barns is to be divided between σ_{12}' and σ_{13}'. The procedure followed here has been to divide the 0.9 barns between σ_{12}' and σ_{13}' in the ratio of their magnitudes. Since the measured value of σ_{12}' is 18.3 ± 1.7 barns (7), any error introduced on account of incorrect assignment of these terms will be less than 3% in each of σ_{12} and σ_{13}. The value of σ_{13}' is obtained from $(\sigma_{12}' + \sigma_{13}')$ and σ_{12}' by subtraction.

σ_{24} and σ_{34}—refer respectively to the pile neutron capture cross sections of Co^{60*} (10.5 min.) and Co^{60} (5.25 yr.) to form Co^{61} (105 min.). They are the effective neutron capture cross sections at the position of the "rabbit" in the NRX reactor. At this position the ratio of fast to thermal neutrons is 0.589.

Approximations made in the derivation of equation [1] are:

(a) the number of Co^{59} atoms (N_1) does not change during the irradiation,

(b) 100% of the Co^{60*} (10.5 min.) disintegrations lead to the Co^{60} (5.25 yr.) state,

(c) the rate of loss of both Co^{60} isomers by neutron capture is small compared with the rate of loss of Co^{60*} (10.5 min.) by decay,

(d) the rate of loss of Co^{60} (5.25 yr.) by decay is small compared with the rate of loss of Co^{60*} (10.5 min.) by decay,

(e) the rate of loss of Co^{61} (105 min.) by neutron capture is small compared with the rate of loss of Co^{61} by decay.

The following values have been employed for the constants in equation [1]:

$$\lambda_2 = (1.10 \pm 0.02) \times 10^{-3} \text{ sec.}^{-1},$$
$$\lambda_4 = (1.10 \pm 0.066) \times 10^{-4} \text{ sec.}^{-1},$$
$$\sigma_{12} = 18.8 \pm 1.8 \text{ barns},$$
$$\sigma_{13} = 16.3 \pm 2.3 \text{ barns},$$
$$\sigma_{12} + \sigma_{13} = 35.1 \pm 1.4 \text{ barns}.$$

The thermal neutron flux was determined by comparison of the sample with a calibrated Co^{60} (5.25 yr.) source after the experiment.

From equation [1] it can be seen that the yield, $\lambda_4 N_4$, differs, as a function of neutron flux and time of irradiation, from the yield which would be expected from single neutron capture in an impurity. Firstly, for sufficiently large σ_{34}, the activity will not approach saturation with increasing time of irradiation, but will increase almost linearly (for $\lambda_2 t \gg 1$) owing to the term $(\sigma_{12} + \sigma_{13})t$. Secondly, the activity is proportional not to the first power but rather to the square of the neutron flux. Both of these characteristics have been utilized to demonstrate that the activity detected is due to Co^{61} formed by successive capture of two neutrons in Co^{59}. Finally, the activities measured at the various irradiation times were inserted in equation [1] and values obtained for σ_{24} and σ_{34}.

III. RESULTS

Two samples were irradiated, each for 3 hr., one at a neutron flux approximately one-half that employed for the other. The results of these trial runs are shown in Figs. 1 and 2, and in Tables I and II. In the tables, the estimated

FIG. 1. Decay curve obtained from Co^{59} sample irradiated for three hours at thermal neutron flux of 5.3×10^{13} cm.$^{-2}$ sec.$^{-1}$ The background is due to Co^{60} γ-rays. The component of half-life $\sim$ 11 min. is due to β-rays from the Co^{60*} (10.5 min.) isomer. Discriminator bias has been set to reject pulses from the Co^{60} (5.25 yr.) β-rays. Where not denoted by vertical bars, the standard deviations are less than the radii of the circles.
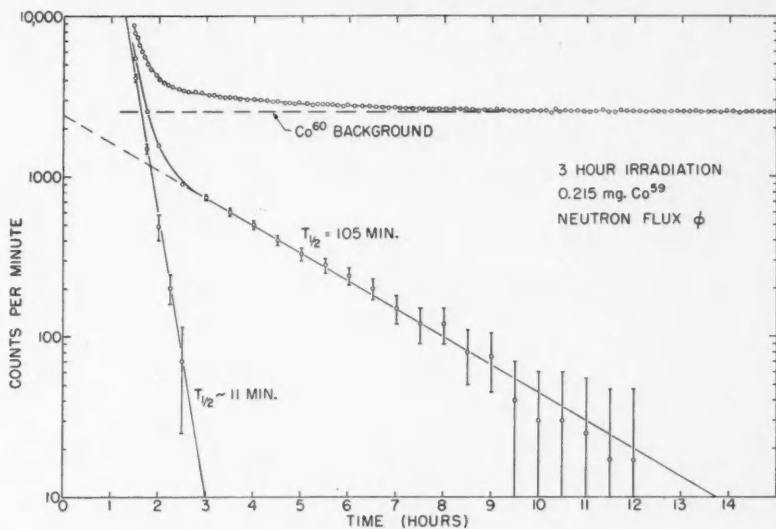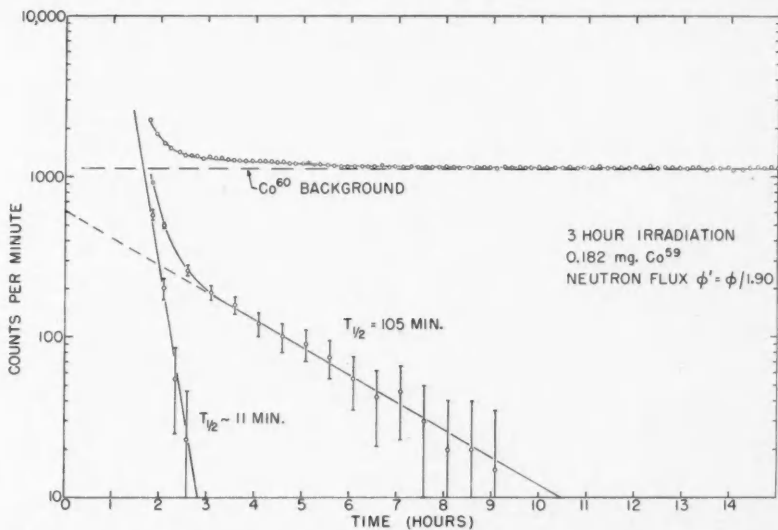

FIG. 2. Decay curve obtained from Co^{59} sample irradiated for three hours at thermal neutron flux of 2.8×10^{13} cm.$^{-2}$ sec.$^{-1}$ Comparison with Fig. 1 indicates that the yield of the 105 min. activity is proportional to the square of the neutron flux. Where not denoted by vertical bars, the standard deviations are less than the radii of the circles.

TABLE I

VARIATION IN AMOUNT OF 105 MIN. ACTIVITY FORMED WITH CHANGE
IN NEUTRON FLUX. THE SYMBOLS ARE DEFINED IN THE TEXT.

Trial	t (hr.)	M (mgm.)	$\lambda_3 N_3$ (10^4 dis./sec.)	$\lambda_4 N_4$ (dis./sec.)	$\dfrac{[(\lambda_4 N_4)/(\lambda_3 N_3)]_2}{[(\lambda_4 N_4)/(\lambda_3 N_3)]_3}$	$\left(\dfrac{\lambda_3 N_3}{N_1}\right)_2 \Big/ \left(\dfrac{\lambda_3 N_3}{N_1}\right)_3$
2	3.00	0.215	18.46	40.5 ± 4.1	1.75 ± 0.29	1.90 ± 0.07
3	3.00	0.182	8.21	10.3 ± 1.3		

TABLE II

AMOUNT OF 105 MIN. ACTIVITY FORMED AS A FUNCTION OF TIME OF
IRRADIATION. THE SYMBOLS ARE DEFINED IN THE TEXT.

Trial	t (hr.)	M (mgm.)	$\lambda_3 N_3$ (10^4 dis./sec.)	ϕ (10^{13}/cm.^{2}/sec.)	$(\lambda_4 N_4)/(\phi^2 N_1)$ (10^{-42} cm.^{4} sec.)	Weighted mean
1	1.53	0.318	11.31	4.32	1.4 ± 0.3	1.4 ± 0.3
2	3.00	0.215	18.46	5.30	1.7 ± 0.3 ⎫	
3	3.00	0.182	8.21	2.79	1.9 ± 0.3 ⎬	1.7 ± 0.2
4	3.00	0.156	12.16	4.82	1.5 ± 0.2 ⎭	
5	6.00	0.285	44.4	4.81	4.8 ± 1.1	4.8 ± 1.1
6	12.00	0.340	100.7	4.59	8.0 ± 1.9 ⎫	
7	12.00	0.243	67.6	4.30	9.4 ± 1.4 ⎬	8.5 ± 0.8
8	12.00	0.332	93.0	4.33	7.8 ± 1.2 ⎭	

error in the mass, M, of Co^{59} is 2%; in $\lambda_3 N_3$, 2%; and in the neutron flux ϕ, 6.5%. As shown in the last column of Table I, the ratio of the flux during trial 2 to that during trial 3 was 1.90 ± 0.07. This was determined after the experiment by comparison of the two samples. The subscripts 2 and 3 refer to the trial number. If the activity $\lambda_4 N_4$ were due to absorption of neutrons in an impurity, or to any process depending on the first power of the flux, then the ratio $(\lambda_4 N_4/N_1)_2/(\lambda_4 N_4/N_1)_3$ should also be the ratio of the fluxes. In this event the ratio shown in column 6 of Table I would be unity. On the other hand, if the activity $\lambda_4 N_4$ is due to Co^{61}, then $(\lambda_4 N_4/N_1)_2/(\lambda_4 N_4/N_1)_3$ will be the ratio of the squares of the fluxes, so that the quantity shown in column 6 of Table I should be the ratio of the fluxes, i.e. 1.90.

The results for all trials are set forth in Table II, and a plot of the weighted mean values of $(\lambda_4 N_4)/(\phi^2 N_1) \times 10^{42}$ against time of irradiation is shown in Fig. 3. The mean values of $(\lambda_4 N_4)/(\phi^2 N_1)$, when inserted in equation [1], yield four equations in the two unknowns σ_{24} and σ_{34}. Solution of these equations, weighting each according to the error assigned to the values of $(\lambda_4 N_4)/(\phi^2 N_1)$, yields the values:

$$\sigma_{24} = 95 \pm 45 \text{ barns,}$$
$$\sigma_{34} = 6.0 \pm 1.4 \text{ barns.}$$

These values were then inserted into equation [1] and the function $(\lambda_4 N_4)/(\phi^2 N_1) \times 10^{42}$ vs. t plotted as the solid line in Fig. 3. Although not a straight line, the curve agrees very closely with the straight line derived by
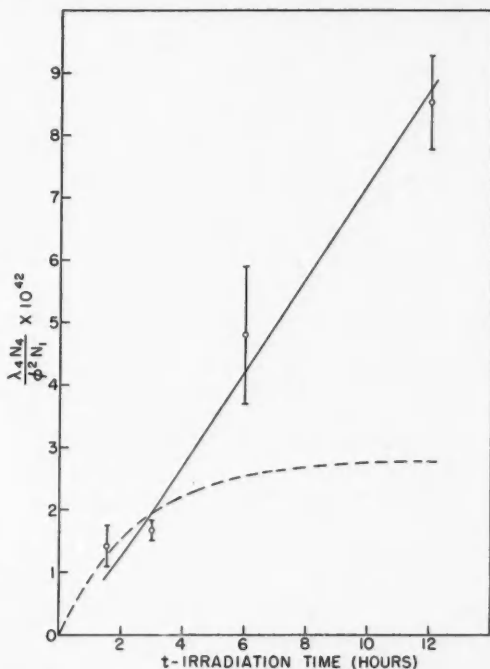
FIG. 3. $(\lambda_4 N_4)/(\phi^2 N_1) \times 10^{42}$ as a function of time of irradiation. The experimental points are shown as circles. The vertical bars represent the probable errors. The solid curve is the computed function using the values $\sigma_{24} = 95$ barns, $\sigma_{34} = 6.0$ barns. The dashed curve illustrates the growth of activity of 105 min. half-life to be expected from single neutron absorption or any process depending on the first power of the neutron flux. The curve has been normalized to the solid curve at $t = 3$ hr.

a least squares fitting of the experimental points. The dashed curve illustrates, for comparison, the growth of activity of 105 min. half-life to be expected for single neutron absorption or any process depending on the first power of the neutron flux. The curve has been normalized to the solid curve at $t = 3$ hr.

IV. DISCUSSION

Within the estimated errors, the results shown in Table I indicate that the activity detected is due to absorption of two successive neutrons in Co^{59} to form Co^{61}. The same conclusion is reached from a consideration of the results of Table II as plotted in Fig. 3. The results of Table I do not however preclude the possibility that some small part of the activity detected is due to activation of impurities with lifetimes comparable with that of Co^{61}. Manufacturer's estimates of the sample impurities indicate that perhaps a few per cent of the activity after 3 hr. irradiation, and considerably less after 12 hr. irradiation, may be due to Mn^{56}(2.6 hr.). Mn however appears to be the only impurity with a lifetime comparable to Co^{61} which can conceivably cause any

difficulty. Cu also occurs as an impurity (0.0001%–0.003%), but the half-life of Cu^{64} is 12.9 hr. and that of Cu^{66} is 5 min., both markedly different from the 105 min. half-life of the Co^{61} activity. Also, the thermal neutron capture cross sections of both Cu^{63} and Cu^{65} are quite low (4.3 barns for the former and 2.1 barns for the latter), so that the presence of Cu in the estimated amounts does not introduce appreciable error in the measurement of the intensity of the 105 min. activity.

It will be noted that the fractional error in σ_{24} is much larger than that in σ_{34}. This is due to the fact that on the whole the measured values depend on experiments done at relatively long irradiation times. From equation [1] it can be seen that for lengthy irradiations, the yield is sensitive to the value of σ_{34} but insensitive to the value of σ_{24}. Thus for an irradiation time of 12 hr. over 80% of the activity is due to capture in the 5.25 yr. isomer. For irradiations of several days capture in the 10.5 min. isomer may be neglected entirely with small error.

ACKNOWLEDGMENTS

REFERENCES

1. COLMER, F. C. W. and LITTLER, D. J.   Proc. Phys. Soc. (London), A, 63: 1175.   1950.
2. DEUTSCH, M. and SCHARFF-GOLDHABER, G.   Phys. Rev. 83: 1059.   1951.
3. HARRIS, S. P., MUEHLHAUSE, C. O., and THOMAS, G. E.   Phys. Rev. 79: 11.   1950.
4. KELLY, W. C.   Phys. Rev. 85: 101.   1952.
5. LANGER, L. M. and MOFFAT, R. J. D.   Phys. Rev. 82: 635.   1951.
6. MILLER, D. R., THOMPSON, R. C., and CUNNINGHAM, B. B.   Phys. Rev. 74: 347.   1948.
7. MOSS, N. and YAFFE, L.   Can. J. Chem. 31: 391.   1953.
8. MULLER, D. E., HOYT, H. C., KLEIN, D. J., and DuMOND, J. W. M.   Phys. Rev. 88: 775. 1952.
9. PARMLEY, T. J., MOYER, B. J., and LILLY, R. C.   Phys. Rev. 75: 619.   1949.
10. PERLMAN, M. L. and FRIEDLANDER, G.   Phys. Rev. 74: 442.   1948.
11. POMERANCE, H.   Phys. Rev. 83: 641.   1951.
12. SINCLAIR, W. K. and HOLLOWAY, A. F.   Nature, 167: 365.   1951.
13. SMITH, L. A., HASLAM, R. N. H., and TAYLOR, J. G. V.   Phys. Rev. 84: 842.   1951.
14. YAFFE, L., HAWKINGS, R. C., MERRITT, W. F., and CRAVEN, J. H.   Phys. Rev. 82: 553. 1951.

THE INTENSITIES OF ATOMIC AND MOLECULAR FEATURES IN THE AURORAL SPECTRUM[1]

By W. Petrie[2] and R. Small[3]

ABSTRACT

A considerable number of auroral spectrograms (dispersion 85–28 Å/mm.) have been analyzed with a recording microphotometer, and integrated intensities obtained for the main features. Relative population rates of the relevant levels are determined from the measured intensities. Excitation mechanisms are discussed and the absence from the spectra of certain low level atomic lines does not appear to be anomalous. It seems that atomic lines are emitted as the results of several processes, while the ionic lines are produced during simultaneous ionization and excitation through electron exchange. Vibrational temperatures of First Negative, First Positive, and Second Positive nitrogen bands are computed.

INTRODUCTION

A considerable number of moderate dispersion spectra of the aurora have been secured at Saskatoon, and all features of appreciable intensity identified. The majority of the spectra were from arc and band displays, and the greater part of the radiation originated from near the 100 km. level. A report on these spectra has already been published (18). In this paper we compare measured and calculated intensities of the permitted atomic lines and a number of nitrogen bands.

MEASURED INTENSITIES

The spectra were secured with an instrument which employed a step-slit of 11 steps, ranging in width from 0.02 to 2.0 mm. This type of slit has certain advantages for several spectroscopic problems. Both weak and strong features may be measured on the same plate. The "characteristic curve" of the emulsion and its variation with wave length may be determined by microphotometering selected lines in the spectrum. The wave length variation of the emulsion sensitivity, and radiation losses in the spectrograph due to absorption and scattering, may be evaluated by measuring the intensity distribution in the spectrum of a standard lamp, and comparing with the theoretical distribution as given by Planck's law.

It was not feasible to superimpose the standard lamp spectrum on the auroral spectra owing to the small size of the plates used by the Schmidt camera; hence the lamp spectrum was recorded on separate plates. This procedure is satisfactory when using a step-slit, since "characteristic curves" may be determined for each individual plate. The auroral and standard lamp spectra were analyzed with a Jarrell-Ash recording microphotometer. The line and band profiles were converted from a logarithmic to a direct intensity scale, the areas under the profiles measured with a planimeter, and corrections

made for the varying wave length sensitivity of the emulsion and losses in the spectrograph. Finally, a correction must be made to remove the effects of atmospheric extinction; this point has been discussed in an earlier paper (17). In view of the uncertainty of this latter correction, it is well to check on the final intensities. This may be realized as follows. The relative intensities of bands in a v'' progression are independent of excitation conditions, and may be computed if the relevant transition probabilities are available. Hence, for such a progression computed and measured intensities should agree. Considering the uncertainties in the A values from which the computed intensities are obtained, the tables given later in the paper show that the agreement is reasonably good.

CALCULATED INTENSITIES OF ATOMIC FEATURES

In order to compute the intensity of a spectral feature it is necessary to know the Einstein A value or some related quantity. Information on the A values of atomic oxygen and nitrogen transitions is now available, as the result of recent calculations. Since the expressions which must be evaluated include the radial wave-functions, it is necessary to have acceptable functions for all the states of the atoms in which one is interested. One approach is to adopt Slater wave-functions, and these have been used by Petrie (16) to calculate OI intensities. More accurate wave-functions have been derived by Bates and Damgaard (3), and these authors compute data from which A values may be obtained. Using their notation, $A = 2.02 \times 10^{18} \, s/g_2\lambda^3 \, \text{sec.}^{-1}$, where s is the "line strength", g_2 the statistical weight of the upper level of the transition, and λ the wave length of the spectral line. The "line strength" is the product of the factors $aS\sigma^2s/\Sigma s$. The meaning and method of obtaining these factors have been discussed in an earlier paper (14). In this paper we use the σ^2 values as obtained from the tables given by Bates and Damgaard (3). Although these are as accurate as can be obtained at present, it must be realized that there are uncertainties in the values, when the arguments which follow later in the discussion are being considered. The term values necessary for the use of the tables were taken from "Atomic Energy Levels" by Moore (12). In the case of a few transitions the tables had to be extended by extrapolation in order to obtain σ^2. The accuracy of the resulting A values is very questionable, especially for the transitions to the ground configuration. In this paper we discuss multiplet rather than line intensities, hence we have summed over all lines of each multiplet in the case of both measured and calculated intensities.

When dealing with a source in thermal equilibrium, the populations of the various levels are given by the Boltzmann law, and the intensity of a spectral line may be expressed as

[1] $$I = N_n A_{nn'} h\nu_{nn'} = N_0 \frac{\omega_n}{\omega_0} e^{-E_n/kT} A_{nn'} h\nu_{nn'}$$

where

N_n = the number of atoms in the upper level involved in the transition,

N_0 = the number of atoms in the ground level of the atom,

ω_n = the statistical weight of level n,

ω_0 = the statistical weight of the ground level,

E_n = the excitation potential of level n,

T = the temperature of the source.

If the source is not in thermal equilibrium, we cannot say what are the relative populations of the various levels, but must instead consider the rate of excitation to these levels. One approach to the problem is to compute the relative intensities of lines assuming that all the relevant levels are populated at the same rate. Since a "cascade" process will follow the excitation of an atom to a certain level, the rate of population will be the sum of the rates due to the direct excitation and "cascade" processes. As an example, suppose that N atoms enter the levels A, B, C, D, and E per second, from the ground level. If transitions ED, EC, DB, and CB are allowed, then the population rate of level B is
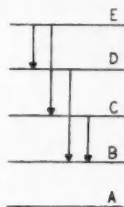
$$N + \frac{A_{CB}}{\sum A_{CX}}\left(N + \frac{A_{EC}}{\sum A_{EX}}N\right) + \frac{A_{DB}}{\sum A_{DX}}\left(N + \frac{A_{ED}}{\sum A_{EX}}N\right).$$

The intensity of the line arising from the transition BA is

[2] $\quad I = \left[N + \frac{A_{CB}}{\sum A_{CX}}\left(N + \frac{A_{EC}}{\sum A_{EX}}N\right) + \frac{A_{DB}}{\sum A_{DX}}\left(N + \frac{A_{ED}}{\sum A_{EX}}N\right)\right]\frac{A_{BA}}{A_{BX}}h\nu_{BA}.$

It is also possible to proceed in the reverse manner, that is to determine the population rates of the levels from which the observed lines arise, from the relative intensities of these lines. This procedure has been followed here, and each set of calculations will be discussed separately.

(a) OI

The highest level line found in the auroral spectrum (18) is from the transition $2p^33p(^5P) - 2p^36d(^5D^0)$. All levels between $^5D^0$ and the ground level, as well as the permitted transitions, are shown in Fig. 1. This scheme assumes that all levels between the ground and $^5D^0$ levels are populated by the excitation mechanism. The transitions giving lines in the spectral range mentioned, the computed A values to the nearest whole number, measured intensities, and calculated relative population rates are given in Table I. These latter data are determined from the equation which expresses the intensity of a line, that is,

[3] $\qquad\qquad\qquad\qquad I = N\frac{A}{\sum A}h\nu$

where N is the total population rate of the levels concerned, from direct excitation and cascade processes. In this and following tables only one line of each multiplet has been listed, whereas the intensities refer to the complete multiplets. The multiplets which we believe are present in the auroral spectrum are those assigned a measured intensity.

TABLE I

OI intensities

Transition	Wave length (Å)	Excitation potential (e.v.)	A value	Measured intensity	Relative population rate
$2p^33s(^5S^0)-2p^33p(^5P)$	7774	10.69	3×10^7	100	1.0
$2p^33p(^3S^0)-2p^33p(^3P)$	8446	10.94	3×10^7	150	1.6
$2p^33s(^5S^0)-2p^34p(^5P)$	3947	12.23	4×10^5		
$2p^33s(^3S^0)-2p^34p(^3P)$	4368	12.31	9×10^6	25	0.23
$2p^33p(^3P)-2p^33s(^3D^0)$	7995	12.49	2×10^7		
$2p^33p(^5P)-2p^35s(^5S^0)$	6456*	12.61	1×10^7		
$2p^33p(^3P)-2p^35s(^3S^0)$	7254*	12.64	6×10^6		
$2p^33p(^3P)-2p^34d(^3D^0)$	7002	12.70	3×10^6		
$2p^33p(^5P)-2p^34d(^5D^0)$	6156	12.70	8×10^6	12	0.18
$2p^33s(^3S^0)-2p^35p(^3P)$	3692	12.82	4×10^5		
$2p^33p(^5P)-2p^36s(^5S^0)$	5436	12.96	4×10^6	10	0.07
$2p^33p(^3P)-2p^36s(^3S^0)$	6046*	12.98	3×10^6		
$2p^33p(^3P)-2p^35d(^3D^0)$	5958*	13.01	8×10^5		
$2p^33p(^5P)-2p^35d(^5D^0)$	5330	13.01	3×10^6	8	0.08
$2p^33p(^5P)-2p^37s(^5S^0)$	5020	13.15	2×10^6		
$2p^33p(^3P)-2p^37s(^3S^0)$	5555*	13.16	2×10^5		
$2p^33p(^5P)-2p^36d(^5D^0)$	4968	13.18	2×10^6	7	0.06

*   *Obscured by other spectral features.*

It has long been considered anomalous that certain low level OI lines appear to be missing from the auroral spectrum. Of the multiplets listed in Table I which are not in the spectrum, only those with wave lengths 3947, 7995, 7002, 3692, and 5020Å are in regions unobscured by other features. Of these λλ 3947, 3692 have relatively small A values. In addition, by considering the transitions illustrated in Fig. 1 and the A values associated with them, it can be seen that the levels from which the missing lines originate will be populated relatively slowly from the cascade process. Hence the absence of these lines is to be expected. It should be mentioned that Meinel (10) has observed part of the 7995Å multiplet in his spectra. We should also note the anomalous intensities of the lines 7774 and 8446Å. The intensity ratio of these lines varies considerably from one spectrum to another. The latter is always the stronger of the two, and the intensity ratio may be as great as 3:1. It would be instructive to compare the intensity ratio of these lines and the intensity of one of the Balmer lines, but the authors have not yet been able to do this.

We will now consider the manner in which the permitted oxygen levels can be excited. Oxygen atoms in the ground ^3P levels will experience collisions with incoming protons, and undergo transitions to higher triplet levels. It is important to realize that a change of electron spin is very unlikely during the collision with a proton (9). Hence, if the excitation resulted solely from this process, only the triplet levels would be excited, but such is not the case. A few oxygen atoms, relative to the total number, will at any given time be in the excited metastable levels ^1D and ^1S, and may be raised to higher singlet levels by collisions with protons. However, this process will be of negligible importance. The hydrogen atoms which result from the capture of electrons by protons may by collision with oxygen atoms in the ground ^3P levels excite
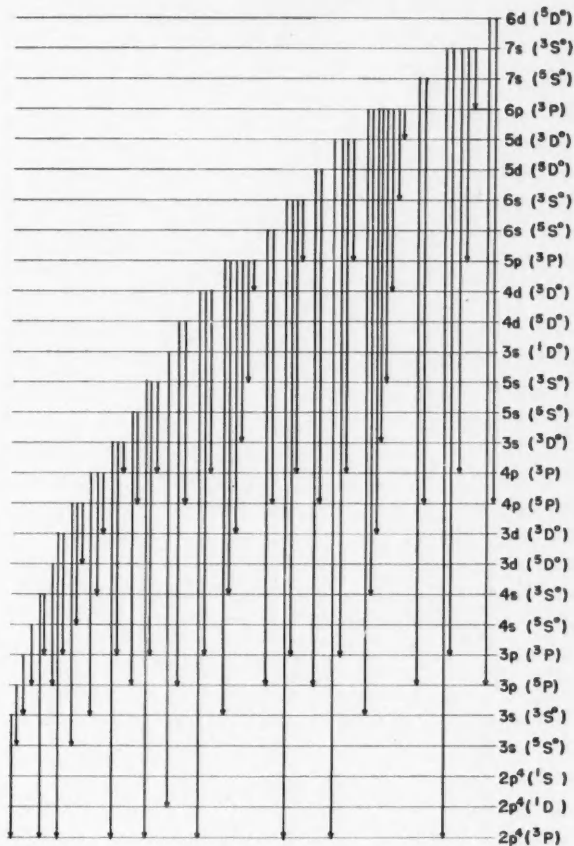
FIG. 1.   OI levels and transitions.

both singlet, triplet, and quintet levels. We can only give a crude estimate as to how effective this process will be. Suppose at the 100 km. level we have an incoming hydrogen atom density of 0.1 per cm.³; a velocity of 10^8 cm./sec.; an oxygen atom density of 10^{13}/cm.³; and a collisional cross section for the excitation of permitted oxygen levels of 10^{-18} cm.² Then the number of excitations/cm.³/sec. is $\sim 10^2$. Oxygen atoms will also be excited by electron collisions. If electrons accompany the protons and have the same velocities, the former particles will be stopped in the atmosphere above the region from which the major part of the auroral light is emitted. It has been pointed out elsewhere (15) that if a proton is to penetrate to the 100 km. level, its energy and velocity of entry must be of the order of 3 Mev. and 2.4×10^9 cm./sec. An electron of the same velocity has energy of 1640 e.v. The range of such an

electron will be much less than that of the proton and the electron will be
stopped near the 200 km. level (5). However, even if primary electrons cannot
reach the main auroral region, fast protons produce electrons of a wide range
of velocity, and these particles will be able to excite a number of oxygen levels.
Bates (4) has shown that for any given spectral series the excitation cross
section falls off rapidly with increase of the principal quantum number. For
both electron and proton excitation the cross section is approximately pro-
portional to σ^2 (2). We would then expect the population rate of the higher
levels to be small, and reference to Table I will indicate that this is indeed the
case. A noticeable feature of the OI data is the presence of lines from several
high d levels and the absence of lines from higher s levels. The identifications
cannot of course be considered final until the multiplet structure is resolved,
and present equipment is not able to do this. At any rate, the lower level lines
which are certainly due to OI are likely excited by the several collisional
processes discussed above.

(b) OII

Data on the low level OII transitions are given in Fig. 2 and Table II. The
line at 6641Å, although near the (6,3) First Positive band, appears to be
absent. The line at 3973Å also appears to be absent. Superimposed on $H\gamma$ are
two features which are likely the lines $\lambda\lambda$ 4347, 4351 of the $(^2D-\ ^2D^0)$ multiplet.
The line at 4072Å, although weak, seems to add to the emission of the VK
(2,13) band. The line at 4415Å may be anomalously intense owing to an over-
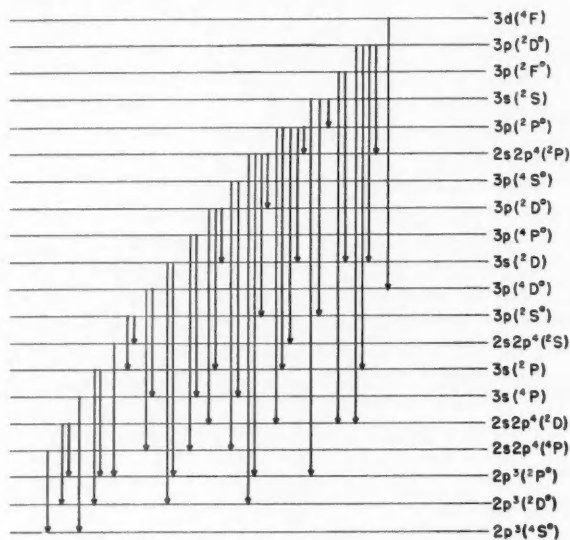lapping (3,8) Second Positive band.

FIG. 2.   OII levels and transitions.

TABLE II
OII INTENSITIES

Transition	Wave length (Å)	Excitation potential (e.v.)	A value	Measured intensity	Relative population rate
$2p^33s(^2P)-2p^33p(^2S^0)$	6641	25.18	3×10^7		
$2p^33s(^4P)-2p^33p(^4D^0)$	4639	25.55	9×10^7	200	1.0
$2p^33s(^4P)-2p^33p(^4P^0)$	4317	25.74	1×10^8	175	0.8
$2p^33s(^2P)-2p^33p(^2D^0)$	4415	26.14	1×10^8	250	1.6
$2p^33s(^4P)-2p^33p(^4S^0)$	3713	26.19	2×10^8	65	0.5
$2p^33s(^2P)-2p^33p(^2P^0)$	3973	26.45	1×10^8		
$2p^33s(^2D)-2p^33p(^2F^0)$	4591	28.24	9×10^7	80	0.4
$2p^33s(^2D)-2p^33p(^2D^0)$	4347*	28.39	1×10^8		
$2p^33p(^4D^0)-2p^33d(^4F)$	4072*	28.58	2×10^8		

* *Obscured by other spectral features.*

In view of these uncertainties, little can be said about the interpretation of the OII intensities. However, it is apparent that the excitation process or processes will differ from those operating in the case of OI. There are relatively few O⁺ particles, and hence the direct excitation of the ion will not be important. An alternative process is that oxygen atoms are simultaneously ionized and excited. This can only effectively occur through the process of the removal of one electron and the exchange of a second with the incident electron. By considering the possible spin changes during these processes, it can be seen that both doublet and quartet levels of OII will be excited. The probability of a proton capturing one electron from the atom and exciting a second is very small. The capture process is most effective at low proton energies ($\sim$ 2800 e.v.) and it requires much higher energy hydrogen atoms to be effective in inelastic collisions. In view of these remarks, it seems likely that OII permitted levels are excited as oxygen atoms are simultaneously ionized and excited through the process of electron exchange.

(c) NI

Data on the relevant NI transitions are given in Fig. 3 and Table III. There are few observed NI lines of appreciable intensity.

TABLE III
NI INTENSITIES

Transition	Wave length (Å)	Excitation potential (e.v.)	A value	Measured intensity	Relative population rate
$2p^33s(^4P)-2p^33p(^4D^0)$	8680	11.70	3×10^7	100	1.0
$2p^33s(^4P)-2p^33p(^4P^0)$	8186	11.79	3×10^7	30	0.29
$2p^33s(^4P)-2p^33p(^4S^0)$	7468*	11.94	4×10^7		
$2p^33s(^2P)-2p^33p(^2P^0)$	8629	12.07	3×10^7		
$2p^33s(^2P)-2p^34p(^2S^0)$	4915	13.14	4×10^6	25	0.22
$2p^33s(^4P)-2p^34p(^4D^0)$	4253*	13.19	2×10^6		
$2s2p^4(^4P)-2p^34p(^4D^0)$	5329	13.19			
$2s2p^4(^4P)-2p^34p(^4P^0)$	5281	13.21			
$2p^33s(^4P)-2p^34p(^4P^0)$	4223	13.21	7×10^6		
$2p^33s(^4P)-2p^34p(^4S^0)$	4151	13.26	3×10^6		

* *Obscured by other spectral features.*
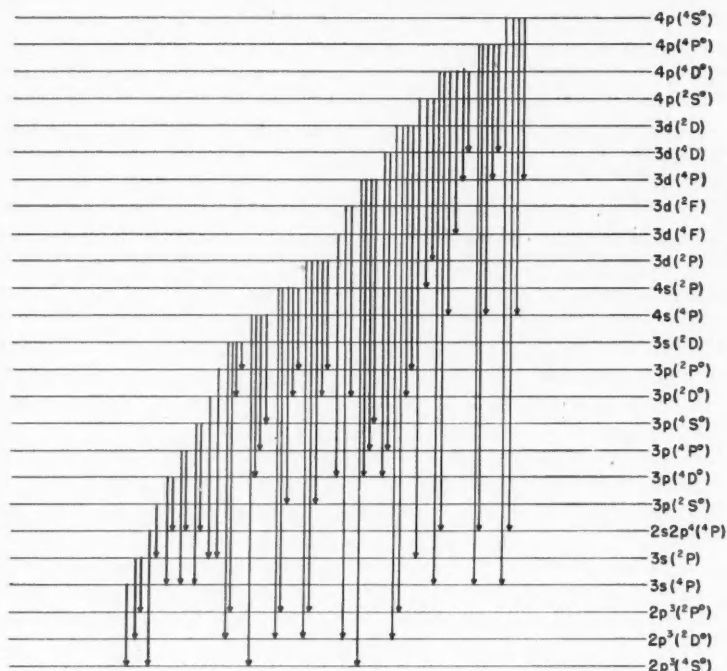
FIG. 3.   NI levels and transitions.

The excitation process of NI and OI levels may differ. Atomic nitrogen lines may be produced during collisions with the molecule, and since the concentration of NI in the atmosphere is unknown, we cannot say whether the major part of the atomic radiation is produced by collisions with nitrogen atoms or nitrogen molecules. Investigations in progress at the Queen's University of Belfast (2) indicate that certain atomic nitrogen lines are readily produced during collisions with the molecules. The writers have carried out an investigation of the spectra of low pressure air discharges at the University of Saskatchewan. The four low level infrared multiplets given in Table III appeared with considerable intensity in the spectra of uncondensed, condensed, and electrodeless discharges through air. The available evidence (8) suggests that a nitrogen molecule dissociates into a neutral and ionized nitrogen atom, rather than two neutral nitrogen atoms. The reaction is

$$N_2 + e \rightarrow N + N^+ + 2e.$$
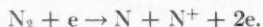
Hence, neutral and ionized atomic lines may be produced in a collision with the molecule. On the other hand, it is almost certain that nitrogen atoms are constituents of the normal night atmosphere, and atomic lines will be produced during collisions with these particles. The arguments presented re-

garding the excitation of oxygen atoms will also apply to the nitrogen atoms. It appears then that the production of nitrogen lines is a complex problem.

(d) NII

Data on the relevant NII transitions are given in Fig. 4 and Table IV. The line at 3995Å overlaps the (1,4) Second Positive band, but from the appearance
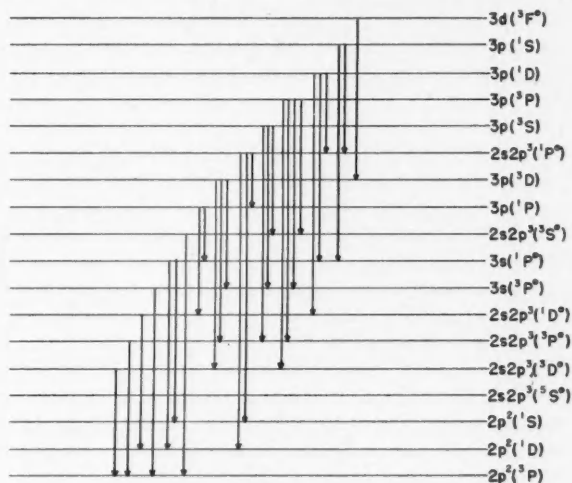
Fig. 4.   NII levels and transitions.

TABLE IV

NII INTENSITIES

Transition	Wave length (Å)	Excitation potential (e.v.)	A value	Measured intensity	Relative population rate
$2p3s(^1P^0)-2p3p(^1P)$	6482	20.32	3×10^7	100	1.0
$2s2p^3(^1D^0)-2p3p(^1P)$	4895	20.32		30	0.68
$2p3s(^3P^0)-2p3p(^3D)$	5667	20.58	5×10^7	180	1.3
$2p3s(^3P^0)-2p3p(^3S)$	5011	20.85	8×10^7	20	1.6
$2p3s(^3P^0)-2p3p(^3P)$	4601	21.07	1×10^8	50	0.35
$2p3s(^1P^0)-2p3p(^1D)$	3995*	21.51	1×10^8		
$2p3s(^1P^0)-2p3p(^1S)$	3437	22.01	2×10^8		
$2p3p(^3D)-2p3d(^3F^0)$	5001	23.04	1×10^8	150	0.87

*   Obscured by other spectral features.

of the blended feature the line must be weak. The line at 3437Å is in the region of the (1,10) VK band, but may be seen although it is very weak.

Arguments regarding the excitation of NII levels parallel those presented in the discussion of OII intensities, and if nitrogen atoms are involved in the excitation, the most likely process is the simultaneous ionization and excitation of nitrogen atoms through electron exchange. In addition, as we have pointed out, collisions with nitrogen molecules may produce excited N^+ ions.

As this discussion has indicated, an analysis of the intensities of oxygen and nitrogen lines in the auroral spectrum does not lead to an unambiguous explanation of the excitation processes operating. It is apparent, as has long been realized, that the excitation is complex in nature. It appears that the ionic lines are produced largely as the result of inelastic collisions between the neutral atoms and electrons whereas the atomic lines are emitted as the result of several processes. It is still desirable that spectra of sufficient dispersion to resolve multiplet structures be secured, since only then can the identifications of some of the atomic features be considered certain.

Unidentified Features

There are a number of weak, but clearly seen sharp features, which appear to be atomic in origin. The wave lengths of these features are given in Table V.

TABLE V

UNIDENTIFIED FEATURES OF POSSIBLE ATOMIC ORIGIN
Wave length (Å)

4042	4358	4950	6137
4047	4684	4958	6141
4180	4687	5916	6402
			6414

A number of these features have been measured by Vegard (22) and attributed to NII and OII multiplets and NO bands. Nicolet (13) has drawn attention to coincidences between the wave lengths of a number of auroral features and NO bands. On the whole, the identifications are not too convincing for a number of reasons, and further discussion at this time does not seem profitable. The features in the red region of the spectrum may be portions of OH airglow bands.

Nitrogen Bands in the Auroral Spectrum

(a) *Negative Group Bands*

Relevant data on these bands are given in Table VI. The transitions listed here are those with the greatest theoretical strengths (21). The ones marked with an A are definitely present in the auroral spectrum, those denoted by P are probably present, and the remainder seem to be absent or obscured. The same notation is used with the tables which describe the other band systems. All the bands in Table VI have been observed in laboratory discharges (6). Notes regarding a number of these features and others which might be expected to appear are given as footnotes to the table. As these notes indicate, there are relatively few of the stronger bands which are unobscured and suitable for intensity measurement. Those which have been measured and their relative intensities are given in Table VII. It is to be noted that these intensities fall to smaller values with increasing v'' than do those of Vegard and Kvifte (22). The same result was found in an earlier discussion of the intensities of the Second Positive bands (17). This is at least partly due to the fact that we have measured spectra of higher resolution, and have given a different

TABLE VI
NEGATIVE GROUP BANDS

v' \ v''	0	1	2	3	4	5	6	7	8	9
0	3914A	4278A	4709A	5228A						
1	3582A[1]	3884A	4236A	4652A	5149A	5754P[2]				
2	3308P[3]	3564A	3858A[4]	4199P[3]	4600A	5076P[3]	5653			
3		3299P[5]	3549A		4167	4554A[6]	5012[7]	5564[8]		
4			3293P[5]	3538P[3]		4141P[3]	4516A	4958A	5486[9]	
5					3533P[2]		4121	4486A[3]	4913[10]	5421P[11]

[1]   The (3,12) VK band has the same wave length, but since it is weak, the N.G. band will not be appreciably affected.
[2]   This band is in the region of a 1 P.G. band.
[3]   This band is in the region of a 2 P.G. band.
[4]   This band is likely blended with a P.G. (4,7).
[5]   There is a weak feature in the spectrum centered at λ3296 which is likely a blend of the (3,1) and (4,2) bands, although Barbier and Williams (J. Geophys. Research, 55: 401. 1950) attribute this to an airglow band.
[6]   This band may be blended with some other feature since it seems abnormally strong.
[7]   This band is in the region of an NII line.
[8]   This band is in the region of O₂⁺ (2,1).
[9]   There is a feature near this wave length but it appears to be broad and diffuse.
[10]   This band is in the region of an NI line.
[11]   There is a feature near this wave length but it appears too broad.

TABLE VII
MEASURED AND CALCULATED INTENSITIES OF N.G. BANDS

v' \ v''	0 M	0 C	1 M	1 C	2 M	2 C	3 M	3 C	4 M	4 C	5 M	5 C	6 M	6 C	7 M	7 C
0	100	100	30	22	6	3.3	2	0.9								
1	10	62	7	37	6	2.6	2	4.6	0.8	1.7						
2			2	79	0.4	10.5					0.2	2.1				
3					1.0						0.6					
4													0.4		0.2	
5															0.2	

evaluation of atmospheric extinction. The intensities of several of the weaker bands cannot be considered reliable.

Bates (1) has discussed in detail the information which may be derived from band intensity data, and we will apply his methods to the intensities given here. The band intensities are computed from the theoretical $p_{v'v''}$ values and the equation

$$[4] \qquad I_{v'v''} = \frac{g_{v'} p_{v'v''} h\nu_{v'v''}^4}{\sum_{v''} p_{v'v''} \nu_{v'v''}^3}$$

where $g_{v'}$ is the population rate of the vibrational level of the upper electronic state. These intensities are given in Table VII for the case $g_{v'} = 1$, i.e. for equal population rates of the excited levels. The theoretical $p_{v'v''}$ values of Turner and Nicholls (21) have been used. By comparing the observed and calculated intensities, it is possible to compute the relative population rates

of the levels of the upper electronic state. The rates for the levels $v' = 0, 1, 2,$ are 1.00, 0.15, 0.020. Bates (1) has determined theoretically the population rates which would result from several different excitation processes. By examining his tables, it appears that if the band system is emitted as the result of simultaneous ionization and excitation of the neutral molecule by electrons the vibrational temperature must be near 1000° K. Although other views have been expressed (19, 20), the band intensities favor the combined ionization and excitation process, the high vibrational temperatures perhaps indicating that protons are involved.

(b) Second Positive Group Bands

Data for the stronger bands of this system, including the bands present and likely present in the auroral spectrum, are given in Table VIII.

TABLE VIII

SECOND POSITIVE GROUP BANDS

v' \ v''	0	1	2	3	4	5	6	7	8	9
0	3371A	3577A	3805A	4059A	4344P[1]					
1	3159A	3339A	3537A	3755A	3998A	4269[2]	4574A	4917P[3]		
2		3136A	3309P[2]	3500P[4]	3710A	3943A	4201P[2]	4490P[2]	4815[5]	
3			3117A	3285A	3469P[6]	3672P[4]	3894P[2]	4142P[2]	4416P[7]	
4					3267P[4]	3446P[5]	3642	3857P[2]	4094P[5]	4356P[8]

[1] This band is in the region of Hγ and is not well resolved.
[2] This band is in the region of a N.G. band.
[3] This band may contribute to the intensity of the NI line at λ4915.
[4] This band is in the region of a VK band.
[5] This band has the wave length of a weak auroral feature.
[6] This band is in the region of the NI line at λ3466.
[7] This band is in the region of an OII line.
[8] There is an auroral feature at the wave length of this band but it appears to be anomalously strong.

The measured intensities of the unobscured bands are given in Table IX. The theoretical intensities which result from equal population rates of the excited levels are calculated from [4] and are given in Table IX. A comparison

TABLE IX

MEASURED AND CALCULATED INTENSITIES OF SECOND POSITIVE GROUP BANDS

v' \ v''	0		1		2		3		4		5		6	
	M	C	M	C	M	C	M	C	M	C	M	C	M	C
0	100	100	59	40	21	14	8	4.5						
1			4	8	20	34	14	15	8	8			3	
2									3	9	3			
3							3	4						

of measured and calculated intensities indicates that the relative population rates of the levels $v' = 0, 1$ are 1, 0.45. These values are much the same as those found from lower dispersion prism spectra (17) which extended further

to the ultraviolet. If we compare only those bands which have comparable wave lengths in order to minimize errors due to atmospheric extinction, somewhat higher relative population rates are found. Hunten (7) has measured the intensities of a number of the bands using a photomultiplier scanning spectrograph, and has obtained still higher population rates. In the earlier paper already referred to the conclusion was reached that the vibrational temperature is $< 500°$ K. However, the relative population rates and hence the temperature are very sensitive to changes in the relative intensities of the bands, and the conclusion seems to be that the data are not sufficiently reliable or extensive to yield accurate vibrational temperatures. Nevertheless, the intensities are of the order expected if the excitation is by collision from the ground level. It should be noted that excitation from the ground level can be achieved by electrons but not by protons and hence a lower vibrational temperature is not unexpected.

(c) First Positive Group Bands

Data for this system including the bands present and likely present in the auroral spectrum are given in Table X.

TABLE X

FIRST POSITIVE GROUP BANDS

v' \ v''	0	1	2	3	4	5	6	7	8
0									
1	8912A								
2	7753A	8722A							
3	6875A	7626A	8542A						
4	6185A¹	6789A	7504A	8369					
5		6127A	6705A	7387A	8204				
6			6070A	6624A	7273A	8047P²			
7				6014A	6545A	7165A	7896P²		
8					5959A	6469A	7059A		
9						5906A	6395A	6968A	
10							5854A	6323A	
11								5804A	6253A

¹ *This band is in the region of 1 P.G. (12,9).*
² *This band is in the region of a Meinel N_2^+ band.*

A considerable number of these bands are partially obscured by other features, including OH bands which appear on the longer exposure spectrograms. The intensities of a number of bands are given in Table XI. Certain of these are partially obscured, but we have corrected for the blending effect of other features. Data on $p_{v'v''}$ values for this system have been given by Bates (1) and Montgomery and Nicholls (11). Using Nicholl's theoretical $p_{v'v''}$ values, intensities are calculated from [4] for equal population rates of the vibrational levels of the upper electronic state. The results are given in Table XI. The relative population rates of the levels $v' = 1, 2, 3, 4, 5, 6, 7, 8$ appear to be of the order of 1.0, 0.58, 0.50, 0.34, 0.30, 0.11, 0.13, 0.030. Because of the uncertainties in the $p_{v'v''}$ values, no great weight can be given to these rates. As Bates (1) has pointed out, excitation of the nitrogen molecule

TABLE XI

MEASURED AND CALCULATED INTENSITIES OF FIRST POSITIVE GROUP BANDS

v'' \ v'	0		1		2		3		4		5		6		7		8		9	
	M	C	M	C	M	C	M	C	M	C	M	C	M	C	M	C	M	C	M	C
0																				
1	100	100																		
2	35	60																		
3			12	43	3	6														
4			0.9	2	29	73														
5					12	67	15	48												
6					1.1	8	9	93												
7							1.3	17	6	102	1.8	15								
8									1.3	38	3	109								
9											1.1		1.8		1.3					
10													1.1							
11															0.9					

from the ground level would populate the upper vibrational levels at a high rate.

(d) Vegard-Kaplan Bands

Data for this system including the bands present and likely present in the auroral spectrum are given in Table XII.

TABLE XII

VEGARD-KAPLAN BANDS

v' \ v''	9	10	11	12	13	14	15	17
0	3352A[1]	3602A	3887P[2]					
1	3198A	3425A	3682A	3979A				
2			3503A	3767A	4072A		4837A	
3					3855P[3]	4171A	4535A	
4								
5								4772A

[1] This band can be clearly seen near the violet edge of the (0,0) 2 P.G. band.
[2] This band is in the region of N.G. (0,0).
[3] This band likely contributes to the (2,2) N.G. band.

(e) Other Band Systems

Vegard and Kvifte (22) attribute a number of features to Goldstein-Kaplan N_2 bands and to NO bands. We conclude from an examination of our spectra that few if any of these bands are present. There are several coincidences, but the agreement is not convincing. Weak features of uncertain origin which have the appearance of bands are listed in Table XIII.

TABLE XIII

WEAK AURORAL BANDS

Wave length (Å)	Possible identification	Notes
3484		Appears to be degraded to red
3614	N.G. (10,9)	Appears to be degraded to red
3632		Broad feature, appears to be degraded to red
3659		Appears to be degraded to red
4378		
4424	VK (2,14)	
4433		
4467	N.G. (6,8)	
4725	2 P.G. (3,9)	
4750		Broad feature, appears to be degraded to red
4805		Broad feature, appears to be degraded to red
4832		Broad feature, appears to be degraded to red
4882	N.G. (6,9)	
4977	2 P.G. (4,11)	
4991		
5087		Appears to be degraded to red
5163		Broad feature
5356		Broad feature
5373	1 P.G. (12,7)	Broad feature
	N.G. (6,10)	
5405	1 P.G. (11,6)	Broad feature
5422	N.G. (5,9)	Broad feature
5476	1 P.G. (9,4)	Broad feature
5488	N.G. (4,8)	Broad feature
5514	1 P.G. (8,3)	Broad feature

ACKNOWLEDGMENTS

REFERENCES

1. BATES, D. R.   Proc. Roy. Soc. (London), A, 196: 217.   1949.
2. BATES, D. R.   Private communication.
3. BATES, D. R. and DAMGAARD, A.   Trans. Roy. Soc. (London), A, 242: 101.   1949.
4. BATES, D. R., FUNDAMINSKY, A., and MASSEY, H. S. W.   Trans. Roy. Soc. (London), A, 243: 93.   1950.
5. DAS GUPTA, N. N. and GHOSH, S. K.   Revs. Modern Phys. 18: 225.   1946.
6. HERZBERG, G.   Ann. Physik, 86: 190.   1928.
7. HUNTEN, D. N.   Private communication.
8. MASSEY, H. S. W. and BURHOP, E. H. S.   Electronic and ionic impact phenomena. Chapter 4.   Oxford University Press.   1952.
9. MASSEY, H. S. W. and BURHOP, E. H. S.   Electronic and ionic impact phenomena. Chapter 8.   Oxford University Press.   1952.
10. MEINEL, A. B.   Astrophys. J.   113: 583.   1951.
11. MONTGOMERY, C. E. and NICHOLLS, R. W.   Phys. Rev. 82: 565.   1951.
12. MOORE, C. E.   Natl. Bur. Standards U.S. Circ. 467.   1949.
13. NICOLET, M.   The emission spectra of the night sky and aurorae.   Gassiot Committee of the Royal Society, 1947.
14. PETRIE, W.   Can. J. Research, A, 25: 293.   1947.

15. PETRIE, W.   Scientific Report AR-1, Geophysics Research Division.   Air Force Cambridge Research Centre, 1950.
16. PETRIE, W., MONAGHAN, P. A., and DOLAN, P. A.   Can. J. Research, A, **27**: **213**.   1949.
17. PETRIE, W. and SMALL, R.   J. Geophys. Research, **57**: 51.   1952.
18. PETRIE, W. and SMALL, R.   Astrophys. J. 116: **433**.   1952.
19. SHKLOVSKI, I. S.   Doklady Akad. Nauk S.S.S.R.   81: 525.   1951.
20. SWINGS, P. and MEINEL, A. B.   *In* The atmospheres of the earth and planets, *edited by* G. P. Kuiper.   2nd ed.   Chapter 6.   University of Chicago Press, Chicago.   1952.
21. TURNER, R. G. and NICHOLLS, R. W.   Phys. Rev. **82**: 290.   1951.
22. VEGARD, L. and KVIFTE, G.   Geofys. Publikasjoner, 18: No. 3.   1951.

THE NEUTRON CAPTURE γ-RAYS FROM POTASSIUM[1]

By G. A. Bartholomew and B. B. Kinsey

ABSTRACT

The capture γ-rays from potassium have been re-examined with greater resolution than was used in previous experiments. The upper end of the spectrum has been carefully studied both with a sample of natural potassium carbonate and with another in which the potassium was enriched in K^{40}. From a comparison of the spectra two γ-rays with energies of 9.39 ± 0.06 and 8.45 ± 0.02 Mev. are assigned to capture by that isotope. The strong γ-ray at 7.757 ± 0.008 Mev. previously ascribed to the ground state transition in K^{40} is now found to represent a transition to a low-lying excited state in that nucleus.

INTRODUCTION

Measurements of the neutron capture γ-rays from potassium obtained with the aid of a pair spectrometer have been described elsewhere (4). The results obtained in that investigation (line width 170 kev.) may be summarized as follows:

(1) a strong γ-ray, B, with an energy of 7.77 ± 0.03 Mev. and an intensity of 11 photons per 100 captures, which was ascribed to the direct transition to the ground state in K^{40};

(2) a weak γ-ray, C, which was ascribed to the ground state transition in K^{42};

(3) a complex and partially resolved spectrum extending from 6 Mev. downwards;

(4) several weak γ-rays with energies above that of B which were accounted for by capture in the rare isotope K^{40}.

It was pointed out that the intensity of the γ-ray B is surprisingly high if this γ-ray is, in fact, emitted in the ground state transition in K^{40} for it must then be of the magnetic quadrupole ($M2$) or electric octupole ($E3$) type according to whether the spin of the compound nucleus formed by capture is 1 or 2 units. Such radiations are expected to be highly forbidden. Also if the weak γ-rays with energies above that of B are actually produced by capture in K^{40} then that nucleus must have a high capture cross section. Since the publication of these results, Pomerance (5) has shown that the capture cross section of K^{40} is 66 barns and contributes about 0.5% to the total potassium cross section.

NEW MEASUREMENTS

The present report contains the results of further measurements of the potassium capture γ-rays made with better resolution (line width 100 kev.). The coincidence spectrum obtained with a sample consisting of about 1 kgm. of anhydrous potassium carbonate is shown in Fig. 1. It will be seen that the main features of the spectrum previously obtained are reproduced. The ener-
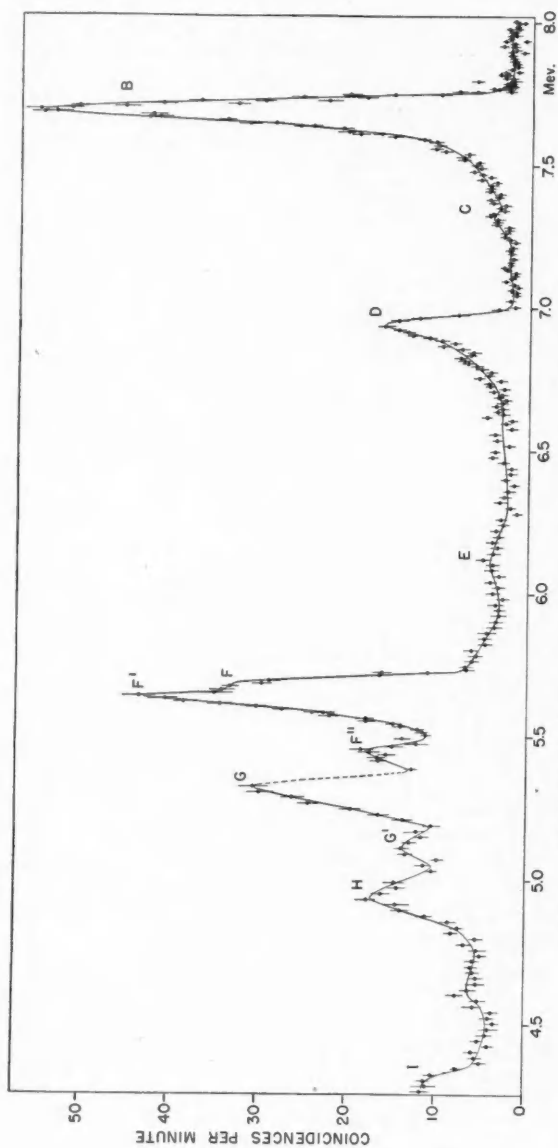
FIG. 1. Coincidence spectrum produced by natural potassium. Line width: 100 kev.

TABLE I

Energies and intensities of the potassium γ-rays

γ-Ray	Energy in Mev.	Intensity in photons per 100 captures in natural potassium	Origin
A''	9.39 ± 0.06	0.02	K^{41}
A'	8.45 ± 0.02	0.1	K^{41}
B	7.757 ± 0.008	3.5	K^{40}
C	7.34 ± 0.02	0.1	K^{42}
D	6.994 ± 0.007	1.3	K^{40}
E	6.31 ± 0.06	0.3	
F	5.740 ± 0.012	6	K^{40}
F'	5.66 ± 0.02	4	K^{40}
F''	5.50 ± 0.02	2.5	K^{40}
G	5.38 ± 0.03	6	K^{40}
G'	5.18 ± 0.02	2	K^{40}
H	5.06 ± 0.02	3	K^{40}
I	4.39 ± 0.03	4	K^{40}

gies and intensities of the strong γ-rays are listed in Table I. The intensities were calculated from the original measurements, in which the peak counting rate of the potassium peak F was compared with that of the 9.0 Mev. γ-ray of nickel emitted from a sample consisting of an intimate mixture of Ni_2O_3 and anhydrous K_2CO_3. In this calculation we used a new and more reliable determination (2) of the variation of the counting efficiency of the spectrometer with energy, and we assumed that when the original nickel comparison was made, the two peaks F and F' were exactly superposed.

An inspection of Fig. 1 will show that the strong coincidence peak F, which originally was not resolved, now appears to be caused by two γ-rays, F and F', the energies and intensities of which may be separately estimated. In addition, another γ-ray F'' appears between F and G. Owing to a breakdown in the apparatus, the part of the spectrum on the upper edge of the peak G was not plotted and unfortunately not repeated, and thus the energy of the γ-ray G cannot be determined with any better accuracy than that obtained in the previous work. No attempt was made to explore the spectrum at energies below that of the γ-ray I.

At the upper end of the spectrum, the γ-ray C which was previously ascribed to the ground state transition in K^{42} is again indicated though its existence
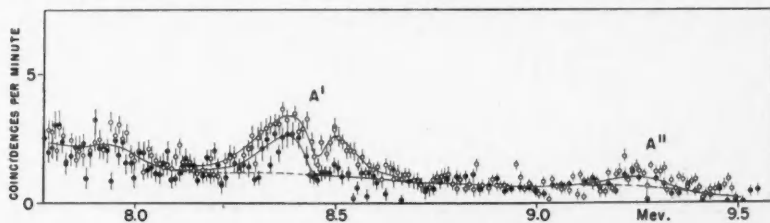

FIG. 2. Higher energy coincidence spectrum produced by potassium. Line width: 100 kev. Full circles, from natural potassium; open circles, from potassium enriched in K^{40}. The peak coincidence counting rate for the γ-ray B is the same for both samples.

is not established with complete certainty. Above 7.7 Mev. (see Fig. 2, full circles) the coincidence spectrum is better defined than in the previous work. The peak (A) previously found at 8.03 Mev. (not shown in Fig. 2) is now known to be spurious. It was a ghost peak derived from the γ-ray B by scattering of electrons from the frames supporting the slits in the spectrometer (2) and this fault has now been greatly reduced. The peak A' is now well defined but the counting rate in the peak A'' is very low and its energy and intensity, therefore, are difficult to measure.

MEASUREMENTS WITH THE SAMPLE ENRICHED IN K^{40}

To verify that the peaks A' and A'' are produced by neutron capture in K^{40}, the coincidence spectrum in this region was examined using a sample of anhydrous potassium carbonate which had been enriched* in K^{40}. The amount of the material used, about 1 kgm., was approximately equal to that used in the natural potassium samples. A mass spectrographic analysis** showed that the K^{40} content had been increased by a factor of 2.2 (to an accuracy of 10%) and a chemical analysis showed that chlorine was present to the extent of 0.12% by weight (as potassium chloride).

The height of the peak B produced by this sample was equal to that produced in similar flux conditions by the natural potassium sample (about 50 coincidences per minute) and the contours of the two peaks could be very exactly superposed. The coincidence spectrum produced by the enriched sample beyond the peak B is shown by the open circles in Fig. 2. It will be seen that the peak A' in the enriched sample is enhanced by a factor of nearly two when allowance is made for the tail of peak B (shown by the broken line). It is therefore clear that A' must be produced by neutron capture in K^{40}. The peak at 8.61 Mev. which appears just above A' may be identified (4) with the ground state γ-ray in Cl^{36}, for its energy is in agreement (within the limits of the experimental errors) with that of the chlorine γ-ray (A) and its intensity is in close agreement with that expected from the known chlorine content of the sample. Unfortunately, we were not able to verify that this γ-ray is due to chlorine by measuring chlorine γ-rays of lower energy, for one of them, at 7.77 Mev., lies under the peak B and is masked by it, and the next, at 7.42 Mev., was not covered by the range of measurements made with the enriched sample. There seems to be no doubt that the low intensity peak A'' must also be caused by neutron capture in K^{40} for, although the enhancement of this peak in the enriched sample is not very clear, there are no strong γ-rays emitted at this energy by any of the possible impurities which the material might contain.

The present measurements with the natural potassium sample were extended to 10.2 Mev., which is close to the neutron binding energy of K^{41}. No γ-rays were detected between the energy of A'' and this value. We should

not expect to detect the ground state γ-ray in K^{41}, for this γ-ray, like that in K^{40}, should be $M2$ and relatively weak. The two γ-rays A' and A'' presumably produce excited states in K^{41} at 1.8 and at 0.85 Mev., although no excited states are known at these energies. The intensities are roughly 14 and 4 photons respectively per 100 captures in K^{40}.

DISCUSSION OF THE γ-RAY B

We have already pointed out that the intensity of the γ-ray B is anomalously high if this γ-ray is indeed that corresponding to the direct $M2$ transition to the ground state of K^{40}. Its energy, 7.757 ± 0.008 Mev., is in agreement (within the stated errors) with the neutron binding energy of K^{40} as determined by Sailor (6), viz. 7.71 ± 0.08 Mev., and within the limits of the errors, 80 kev., there is no evidence in Fig. 1 for the existence of another γ-ray with an energy slightly above that of B which instead could be the ground state transition.

The recent discovery of a low-lying state in K^{40} near 30 kev. accounts for the difficulty, for the energy of B is in close agreement with that of the transition which produces this state directly.* In both K^{40} and K^{42} the odd proton and odd neutron are in $d_{3/2}$ and $f_{7/2}$ states respectively. In the ground state of K^{42}, which has a spin of 2 units (1), it is clear that the total angular momenta of the odd neutron and proton are antiparallel. The spin of K^{40} is 4 units which indicates that for some reason, the antiparallel condition of the spins does not give the most stable configuration. We should expect, therefore, the excited state of K^{40} to be the analogue of the ground state of K^{42}, i.e., that it should have a spin of 2 units and odd parity. The γ-ray (B) emitted in the direct transition to the 30 kev. state should then be of the $E1$ type regardless of the spin of the compound state produced by neutron capture. This interpretation is consistent with the high intensity of γ-ray B for it has been shown elsewhere (3) that $E1$ γ-rays, in this energy range, are strong. It follows that the transition from the 30 kev. state to the ground state should be of $E2$ type, and according to Weisskopf's formula, it should have a lifetime (when account is taken of internal conversion) of about 10^{-6} sec. (7). No isomeric state formed by neutron capture has been found in potassium nor would it have been readily detected for such a lifetime is too short for direct activation measurements.

REFERENCES

1. BELLAMY, E. H. and SMITH, K. F. Phil. Mag. 44: 33. 1952.
2. KINSEY, B. B. and BARTHOLOMEW, G. A. Can. J. Phys. 31: 537. 1953.
3. KINSEY, B. B. and BARTHOLOMEW, G. A. Physica, 18: 1112. 1952.
4. KINSEY, B. B., BARTHOLOMEW, G. A., and WALKER, W. H. Phys. Rev. 85: 1012. 1952.
5. POMERANCE, H. Phys. Rev. 88: 412. 1952.
6. SAILOR, V. L. Phys. Rev. 77: 794. 1950.
7. WEISSKOPF, V. F. Phys. Rev. 83: 1073. 1951.

*W. W. Buechner, private communication.

A QUANTUM-STATISTICAL THEORY OF LIQUID HELIUM[1]

By K. Buckthought

ABSTRACT

A model for liquid He^4 is set up in which the atoms are regarded as an assembly of Bloch waves following Bose-Einstein statistics. The potential field inside the liquid is estimated. Numerical calculation of the thermodynamic functions shows fair agreement with experiment. The λ-temperature and its variation with pressure are calculated, and are in good agreement with observed values. The model is also applied to liquid He^3. The variation of entropy with temperature is calculated.

1. INTRODUCTION

London (16a) and Tisza (18) have attempted to explain the anomalous properties of liquid He^4 by the postulate that an assembly of He^4 atoms obeys Bose-Einstein statistics. Their model for the liquid is an ideal Bose-Einstein gas, and they ignore the strong interatomic forces which exist in the liquid.

Phenomenological models in which the He^4 atoms are regarded as Bloch waves (2) moving through a quasi-crystalline potential field have been proposed by London (16b) and Goldstein (6). These models incorporate no information about the interatomic potential, although the latter is known with fair accuracy from the equation of state of He^4 gas (4, 11, 17).

In the present theory an attempt is made to evaluate the mean potential field encountered by each He atom in the liquid. The wave function and potential field are regarded as functions solely of the coordinates of the single atom, in the sense of the Hartree self-consistent field approximation for atoms and molecules (7). The wave function for the helium atom is then of the Bloch wave type, i.e. a plane wave whose amplitude is modulated by the potential field due to all the other atoms. The assembly of Bloch waves, regarded as independent systems, is to obey Bose-Einstein statistics.

2. SPACE-DISTRIBUTION OF ATOMS IN LIQUID He^4

Owing to the disordering effect of the large zero-point energy, He^4 cannot form a space-ordered crystalline lattice, even at $0°$ K., except under high pressure. However, the potential field encountered by a single atom must have, on the average, some of the periodicity characteristic of a crystalline lattice field. London (16b) has investigated the stability of certain ordered configurations in He^4, and has demonstrated that most such configurations correspond to too high an internal energy to be probable (see also Appendix A).

We expect that most disordered configurations which depart widely from a distribution consistent with the most stable one will also be highly improbable. This most stable configuration is that of a face-centered lattice, each of whose sites is occupied 50% of the time. Such a structure has been proposed by Keesom and Taconis as a result of their X-ray investigations of He^4 (10). The coordination number of such a structure is six, and the interatomic distance, for the observed density of liquid He^4, is therefore 3.2Å.

We therefore propose to replace the actual field inside liquid He[4] by that smoothed-out field which would result from the following model. The atoms are to be represented by Bloch waves of the form

[1] $$\psi_k(\mathbf{r}) = u(\mathbf{r})e^{i\mathbf{k}\cdot\mathbf{r}}$$

where $u(\mathbf{r})$ is a function having a three-dimensional periodicity in the space vector $\mathbf{r}$, and $\mathbf{k}$ is a constant vector playing the role of a set of three quantum numbers, analogous to the wave vector for a plane wave.

We assume that the maxima of $u(\mathbf{r})$ occur at points of a space lattice consistent with the X-ray experiments and the theoretical considerations raised by London.

For self-consistency, we should require that the wave functions used in evaluating the potential be the same as the above type (equation 1). Such a program would require a prohibitive amount of calculation, since the assignment of atoms of the assembly to various wave functions, given by different values of $\mathbf{k}$, depends on the temperature. Thus a separate calculation should be made for each temperature. However, we are interested in a small range of temperatures (0–2.5° K.) for which the thermal energy is about one tenth of the zero-point energy. For the purpose of calculating the potential field, we have replaced the actual set of wave functions, with finite but small k-values, by the wave functions of lowest energy, with $k = 0$. These wave functions have been calculated, using the Wigner-Seitz method (20). The potential field employed for this calculation was the spherically symmetrical one used by Lennard-Jones and Devonshire in their theory of the liquid state (15). The Wigner-Seitz wave function was calculated from the Schrödinger equation by applying the WBK method (3a, 12, 19). The wave function, in terms of distance from a lattice-point, is shown in Fig. 1.
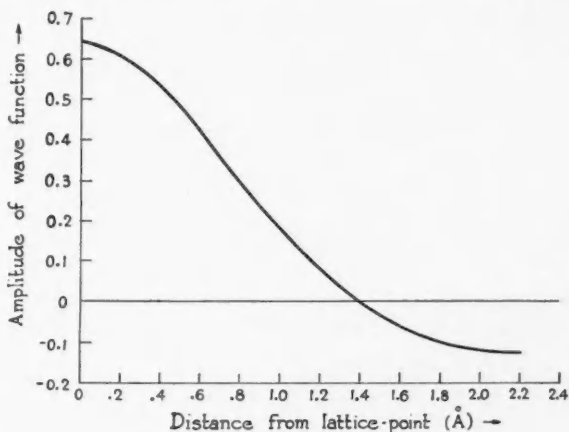

FIG. 1. Wigner-Seitz wave function for liquid He[4].
(Units of probability density: atoms per cubic Ångstrom unit.)

3. THE POTENTIAL FIELD INSIDE LIQUID HE[4]

The potential field was calculated from

$$[2] \qquad V_i(\mathbf{r}_i) = \sum_{j \neq i}^{N} \int \cdots \int v_{ij} |\psi_j^0|^2 \, d\tau_j$$

where $V_i(\mathbf{r}_i)$ is the hypothetical fixed potential field encountered by the ith atom of N atoms in the liquid, $v_{ij}(r_{ij})$ is the interaction energy between the ith and j^{th} atoms, $\psi_j^0(\mathbf{r}_j)$ is the Wigner-Seitz wave function for the jth atom, and the integration is taken over all the space available to the liquid. In practice, because of the crystal symmetry it is necessary to calculate this function only for a small volume surrounding one lattice-point. At each point of this volume, there are contributions from wave functions whose maxima of probability density lie at neighboring lattice-points. Because the pair potential falls off very rapidly with increasing distance, the contributions from only a few (about 10) wave functions are significant at a given point.

The pair-potential takes on large positive values for interatomic distances less than 2.6 Å. Here the mutual wave function of two He atoms must go to zero, imposing an additional correlation effect outside the scope of the Hartree method. This has been taken into account crudely by excluding all contributions to V_i inside a sphere of radius 2.6 Å, centered around the field point $\mathbf{r}_i$. Also we assume that the ith lattice point is vacant.

The pair-potential used was that of Buckingham, Massey, and Hamilton (4). There is some evidence that this function gives the best fit to the data for He[4] gas (11, 17).

4. SOLUTION OF THE SCHRÖDINGER EQUATION

Solutions of the Schrödinger equation in which the potential has a three-dimensional periodicity in space have been discussed by many authors (3b, 5, 21). We shall adopt the procedure and notation of Wilson (21).

We expand the potential and one-atom wave function in a three-dimensional Fourier series based on the reciprocal lattice. Denoting the reciprocal lattice unit vectors by $\mathbf{b}_1$, $\mathbf{b}_2$, $\mathbf{b}_3$, and the general reciprocal lattice vector by $\mathbf{g}_b = g_1 \mathbf{b}_1 + g_2 \mathbf{b}_2 + g_3 \mathbf{b}_3$, where the g_i are integers, we may write the potential field $V(\mathbf{r})$ and wave function $\psi_{\mathbf{k}}(\mathbf{r})$ in the form

$$[3] \qquad V(\mathbf{r}) = \sum_{g_1 g_2 g_3 = -\infty}^{\infty} V_{\mathbf{g}} \exp\left(2\pi i \mathbf{g}_b \cdot \mathbf{r}\right),$$

$$[4] \qquad \psi_{\mathbf{k}}(\mathbf{r}) = \sum_{g_1 g_2 g_3 = -\infty}^{\infty} C_{\mathbf{g}} \exp\left(2\pi i \mathbf{g}_b \cdot \mathbf{r}\right).$$

Substituting these in the Schrödinger equation for one atom, we have an infinite set of linear equations

$$[5] \qquad \left[E - V_{000} - \frac{\hbar^2}{2m} (\mathbf{k} + 2\pi \mathbf{g}_b)^2 \right] C_{\mathbf{g}} = \sum_{\mathbf{h} \neq (000)} C_{\mathbf{g-h}} V_{\mathbf{h}}.$$

These equations are homogeneous in the $C_{\mathbf{g}}$ as unknowns, and have solutions only if the infinite determinant for the coefficients of the $C_{\mathbf{g}}$ vanishes. This determines the eigenvalue E, as a function of $\mathbf{k}$.

For a free atom we would have

$$E = V_{000} + \frac{\hbar^2}{2m} |\mathbf{k}|^2,$$

$$\psi_\mathbf{k} = \text{const.} \times e^{i\mathbf{k}\cdot\mathbf{r}}.$$

Using these as a zero-order approximation in equation 5, we obtain for a first approximation,

[6] $$E = V_{000} + \frac{\hbar^2}{2m} k^2 - \frac{m}{2\pi\hbar^2} \sum_\mathbf{g} \frac{|V_\mathbf{g}|^2}{\pi|\mathbf{g}_b|^2 + \mathbf{g}_b\cdot\mathbf{k}}.$$

This holds if all the $|C_\mathbf{g}|$ are very much less than $|C_{000}|$, i.e. if the wave function does not depart much from that for a plane wave.

For the energy level density, given by $g(E)\,dE$, that is the number of quantum states in the energy range E to $E + dE$, we have

[7] $$g(E)\,dE = \frac{V}{8\pi^3} \int\int\int_E^{E+dE} dk_1\,dk_2\,dk_3.$$

We have evaluated this by expanding the last series of terms of equation 6 in a power series in the k_i, taking advantage of the fact that

$$g_i b_i k_i < \pi|\mathbf{g}_b\cdot\mathbf{k}|.$$

For any term corresponding to a set of integers g_1, g_2, g_3, there is a corresponding term given by $-g_1, -g_2, -g_3$; in the summation over all values of $\mathbf{g}$, terms in odd powers of the k_i consequently disappear. Similarly, summation over all permutations of the $+$ and $-$ signs in $\pm g_1, \pm g_2, \pm g_3$ cancels out all cross terms $k_i k_j$, where $j \neq i$. We get finally

[8]
$$E = V_{000} + \frac{\hbar^2 k^2}{2m} - \frac{4m}{\pi\hbar^2} \sum_{|g_1|,|g_2|,|g_3|} |V_\mathbf{g}|^2 \left\{ \frac{1}{\pi G^2} + \frac{k^2}{3\pi^3 G^4} \right.$$
$$\left. + \frac{k_1^4 + k_2^4 + k_3^4}{9\pi^5 G^6} + \dots \right\}$$

where $G = |g_b|$.

In this rapidly converging series the ratio of successive terms in k_i is of the order of 10^{-1} at most. Thus it will suffice to keep only those terms shown above.

We have evaluated equation 7 approximately, using expression 8 for E, giving

[9] $$g(E) \doteq \frac{2\pi V}{h^3}\left(\frac{2m}{\alpha}\right)^{3/2} \left[(E - E_0)^{\frac{1}{2}} + \frac{512m^3}{3h^6\alpha^2} \sum \frac{|V_\mathbf{g}|^2(E - E_0)^{3/2}}{G^6} \right],$$

where

$$\alpha = 1 - \frac{\hbar^4}{6m^2\pi^4} \sum \frac{|V_\mathbf{g}|^2}{G^4},$$

$$E_0 = V_{000} - \frac{\hbar^2}{m\pi^2} \sum \frac{|V_\mathbf{g}|^2}{G^2}.$$

The last expression is the net energy at $0°$ K. With the data of Appendix B, resulting from the numerical evaluation of the Fourier coefficients for the potential field, we find $E_0 = -10.8$ cal./mol., as compared with the accepted value of -14.2 cal./mol. (9).

5. STATISTICAL MECHANICS OF LIQUID HE[4]

The He[4] atoms are independent systems in this model, each moving in its own potential field. The distribution law for a Bose-Einstein assembly of independent systems is

$$[10] \qquad n(E)\, dE = \frac{g(E) dE}{e^{(E-\mu)/RT} - 1}$$

where μ is the chemical potential (per mol.). E is now counted from the lowest quantum state as energy zero, and we will allow for the zero-point energy by including it as a constant U_0, in the internal energy of the assembly taken as a whole.

To obtain μ as a function of temperature, we write the condition that the total number of atoms in volume V be a constant, i.e.

$$[11] \qquad N = \int_0^{\infty} n(E)\, dE = \int_0^{\infty} \frac{g(E)\, dE}{e^{(E-\mu)/RT} - 1}\,.$$

The total internal energy of the assembly is then

$$[12] \qquad U = U_0 + \int_0^{\infty} \frac{Eg(E) dE}{e^{(E-\mu)/RT} - 1}\,.$$

From these two equations all the thermodynamic functions may be deduced.

London (16a) has shown that below a certain temperature T_λ given by

$$N = \int_0^{\infty} \frac{g(E) dE}{e^{E/RT_\lambda} - 1}$$

a finite fraction of the systems "condense" into the lowest energy state. The number of systems in this state, for temperatures less than T_λ, is

$$N_0 = \frac{1}{e^{-\mu/RT} - 1}\,.$$

The thermodynamic functions below the λ-point are determined by putting $\mu = 0$ in equation 12, as shown by London.

The thermodynamic functions were evaluated using equation 9 for the energy-level density. The entropy and specific heat are shown in Fig. 2, as functions of temperature.

The internal energy was calculated as a function of volume, in the following way. In the analysis of the potential field the contributions from the attractive and repulsive parts of the potential were kept separate. For the purpose of calculating their variation with density, they were assumed to follow a Lennard-Jones potential (14), viz.

$$v_{ij} = \frac{\xi}{r_{ij}^{12}} - \frac{\eta}{r_{ij}^{6}}$$
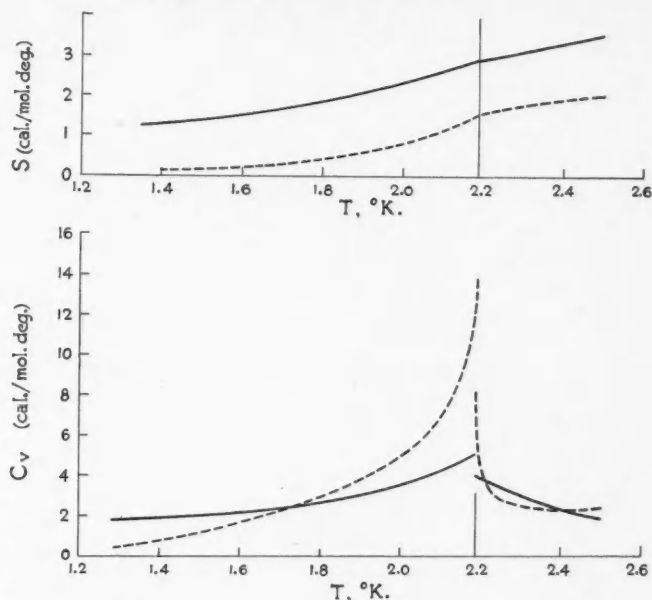
FIG. 2. Entropy and specific heat of liquid He⁴.
——————— Calculated values. ————————— Observed values.

where ξ, η are positive constants, r_{ij} is the interatomic distance. This relation enables us to deduce the variation in the potential field resulting from changes in interatomic distance.

Thus the compressibility K_T and expansion coefficient β could be calculated from the thermodynamic formulae

$$1/K_T = V \, \partial^2 F/\partial V^2, \text{ where } F = U - TS,$$

$$T(dp/dT)_V - p = (dU/dV)_T,$$

$$\beta = K_T(dp/dT)_V.$$

The results of these calculations are shown in Fig. 3.

Similarly, the variation of T_λ with density was calculated, and its variation with pressure deduced from the calculated compressibility (Fig. 4). At zero pressure we find $T_\lambda = 2.23°$ K., in fair agreement with the observed value of $2.186°$ K. (9).

The temperature variation of the compressibility of liquid He⁴ is anomalous, in that there is a discontinuity at the λ-point. It is therefore particularly satisfactory that this discontinuity, together with the rise in compressibility toward the λ-point, is indicated in this theory. The negative expansion coefficient below T_λ and the sign of dT_λ/dp are also accounted for.

Exact agreement with experiment is not to be expected from a theory which takes into account the interatomic interactions in an oversimplified way.
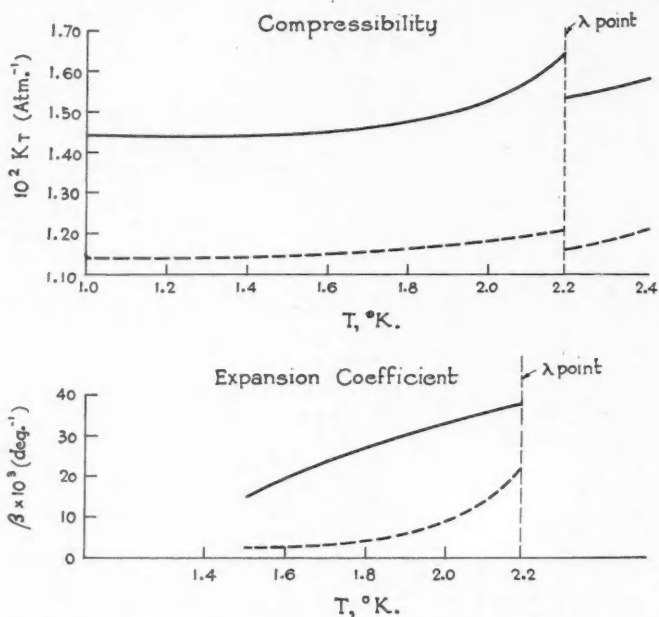
Fig. 3. Compressibility and expansion coefficient of liquid He[4].
——————— Calculated values.   ---------- Observed values.
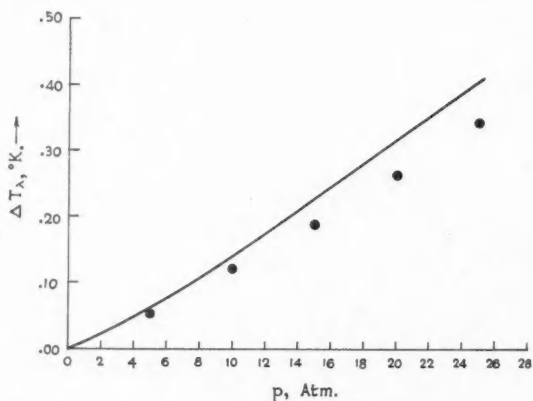

Fig. 4. Variation of λ-temperature with pressure.
——————— Calculated values.   ● Observed values.

6. LIQUID HE³

The same type of model was applied to the problem of liquid He³. In the absence of direct experimental evidence, it was assumed that the space distribution is the same as that in liquid He⁴, except for the larger interatomic distances, corresponding to the larger molar volume of He³. In fact, a calculation of the internal energy for various possible configurations shows that the only stable one is the 50% occupied face-centered lattice used for He⁴ (Appendix A).

The Fermi-Dirac statistics was applied to this case. A system obeying Fermi-Dirac statistics is characterized by a degeneracy temperature (3b)

$$T_0 = \frac{3}{5}\frac{\alpha h^2}{2mR}\left(\frac{3N}{8\pi V}\right)^{2/3}.$$

Here the constant α, characteristic of the present model, has been introduced to take into account that the energy level density of the Bloch wave energy spectrum differs from that of an ideal gas. The value of α was calculated by a method analogous to that used for He⁴, and was found to be 0.94. We find
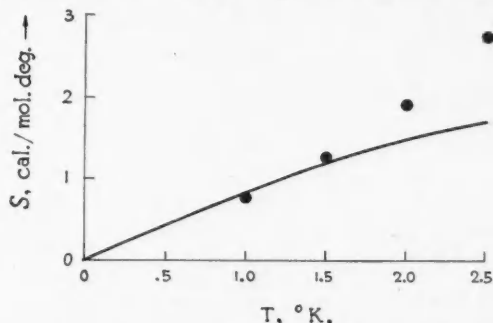

Fig. 5. Variation of entropy of liquid He³ with temperature.
———————— Calculated values. ● Observed values.

$T_0 = 1.8°$ K. This gives a Fermi-Dirac entropy as shown in Fig. 5, which departs from the linear relationship, where the temperature is not small compared to T_0.

The internal energy at 0° K. was calculated to be −1 cal./mol., compared to an experimental value of −4.4 (1).

7. DISCUSSION

The concept of liquid He⁴ as a Bose-Einstein assembly seems to provide a satisfactory basis for the explanation of the thermodynamic properties of the liquid. The striking difference in behavior of the two isotopes of helium is immediately explained, as in the ideal gas model proposed by London. But the model considered here corrects some of the defects of the ideal gas theory. The general behavior of the compressibility and expansion coefficient is explained, and the sign of dT_λ/dp is predicted correctly.

But the specific heat curve has a much sharper maximum at the λ-point than predicted. This points to some ordering process not taken into account—perhaps outside the realm of the Bose-Einstein statistics, and thus probably

present in He^3 as well. For the latter, the exclusion principle presumably prevents a condensation in momentum space.

An additional weakness of the present theory lies in its prediction of a specific heat varying as $T^{3/2}$ near absolute zero. According to the theory of Landau (13) He^4 behaves like a Debye solid near $0°$ K., with a specific heat going to zero as T^3. The experimental evidence favors Landau's theory (8).

Although Landau has had considerable success in predicting the behavior of liquid He^4 near absolute zero, his theory fails to give a satisfactory account of the λ-transition. An important feature of the theory presented here is its ability to deal with the discontinuities at the λ-point.

ACKNOWLEDGMENTS

APPENDIX A

Potential and Kinetic Zero-point Energies for Various Types of Lattice

The potential energy for each structure has been determined by summing up the contributions to the potential energy at a lattice-point, of nearest neighbors and next nearest neighbors. This energy has been multiplied by Avogadro's number divided by two, to get the energy per mole, U.

The zero-point energy was calculated from the formula (16b)

$$Z = h^2/8Mr^2,$$

where M is the mass of the atom, r is the mean "radius of action" of the atom, conceived of as confined to a sphere. r was calculated as follows: (a) if the number of nearest neighbors is 8 or 12, r is to be the nearest neighbor distance less 2.4 Å; (b) if the number of neighbors is 4 or 6, r is to be the mean of the nearest neighbor distance less 2.4 Å. If there are three nearby shells of lattice sites, the radii of all three are averaged.

These criteria were adopted to allow for the lower kinetic energies associated with the more open structures, having lower coordination numbers.

In Table I all energies are in cal./mol. The Keesom-Taconis lattice is that proposed in Reference (10). The last two types listed are essentially the same, except that the "holes" of one are the lattice-sites of the other.

TABLE I

Lattice type	He⁴			He³		
	Z_4	U_4	$Z_4 + U_4$	Z_3	U_3	$Z_3 + U_3$
Cubic close-packed	46	−36	+10	50	−17	+33
Body-centered cubic	59	−37	+22	64	−22	+42
Simple cubic	33	−40	−7	36	−23	+13
Diamond	41	−48	−7	44	−34	+10
50% body-centered	52	−58	−6	56	−38	+18
Keesom-Taconis	46	−56	−10	49	−44	+5
50% face-centered	46	−60	−14	49	−46	+3

APPENDIX B

Analysis of Potential Field Inside Liquid He⁴

We may conveniently represent the lattice used as a basis for the calculation, by a set of simple cubic lattices having each the same lattice constant, but displaced with respect to one another. If the Fourier coefficient for the 50% occupied face-centered lattice is V_g, and that for any one of the simple cubic ones is v_g, we have

$$V_g = v_g \{ 1 + \exp \pi i(g_1 + g_2) + \exp \pi i(g_2 + g_3) + \ldots$$
$$+ 2 \cos \tfrac{1}{2}\pi(g_1 + g_2) + 2 \cos \tfrac{1}{2}\pi(g_2 + g_3) + \ldots$$
$$+ \exp \tfrac{1}{2}\pi i(g_1 - g_2 + 2g_3) + \exp \tfrac{1}{2}\pi i(g_2 - g_3 + 2g_1) + \ldots \}$$

giving

$$V_{000} = 16\, v_{000}, \quad |V_{111}| = 8\,|v_{111}|, \quad |V_{222}| = 16\,|v_{222}|, \ldots ;$$
$$|V_{100}| = |V_{010}| = \ldots = 0.$$

The v_g were determined from numerical integration of

$$v_g = \frac{1}{\tau} \iiint_\tau V(\mathbf{r}) \exp -2\pi i(\mathbf{g}_b \cdot \mathbf{r})\, d\tau$$

over the volume of the liquid τ, giving the following values (cal./mol.)

$$V_{000} = -5.6, \quad V_{111}^2 = 4.9, \quad V_{222}^2 = 26.4, \quad V_{333}^2 = 0.$$

REFERENCES

1. ABRAHAM, B. M., OSBORNE, D. W., and WEINSTOCK, B.   Phys. Rev. 80: 366.   1950.
2. BLOCH, F.   Z. Physik, 52: 555.   1928.
3. BRILLOUIN, L. (a) Compt. rend. 183: 24.   1926.
                  (b) Die Quantenstatistik. Verlag von Julius Springer, Berlin.   1931.
4. BUCKINGHAM, R. A., MASSEY, H. S. W., and HAMILTON, J.   Proc. Roy. Soc. (London), A, 179: 103.   1941.
5. FROHLICH, H.   Elektronentheorie der Metalle.   Verlag von Julius Springer, Berlin.   1936.
6. GOLDSTEIN, L.   J. Chem. Phys. 14: 276.   1946.
7. HARTREE, D. R.   Proc. Cambridge Phil. Soc. 24: 89; 24: 111.   1928.
8. HULL, R. A., WILKINSON, K. R., and WILKS, J.   Proc. Phys. Soc. (London), A, 64: 379.   1951.
9. KEESOM, W. H.   Helium. Elsevier Publishing Co. Inc., Amsterdam.   1942.
10. KEESOM, W. H. and TACONIS, K. W.   Physica, 5: 270.   1938.
11. KISTEMAKER, J. and KEESOM, W. H.   Physica, 12: 227.   1946.
12. KRAMERS, H. A.   Z. Physik, 39: 828.   1926.
13. LANDAU, L.   J. Phys. (U.S.S.R.), 5: 71.   1941.
14. LENNARD-JONES, J. E.   Proc. Roy. Soc. (London), A, 106: 463.   1924.
15. LENNARD-JONES, J. E. and DEVONSHIRE, A. F.   Proc. Roy. Soc. (London), A, 163: 53. 1937; 165: 1.   1938.
16. LONDON, F. (a). Phys. Rev. 54: 948.   1938.
                (b). J. Phys. Chem. 43: 49.   1939.
17. ROSEN, P.   J. Chem. Phys. 18: 1182.   1950.
18. TISZA, L.   Compt. rend. 207: 1035, 1186.   1938.
19. WENTZEL, G.   Z. Physik, 38: 518.   1926.
20. WIGNER, E. and SEITZ, F.   Phys. Rev. 43: 804.   1933; 46: 509.   1934.
21. WILSON, A. H.   Theory of metals. Cambridge University Press, London.   1936.

AN ATOMIC MASS STUDY OF NUCLEAR SHELL STRUCTURE IN THE REGION $28 \leqslant n \leqslant 50$ AND $28 \leqslant Z \leqslant 40$[1]

By Benjamin G. Hogg[2] and Henry E. Duckworth

ABSTRACT

New mass spectrographic masses are reported for some of the isotopes of gallium, germanium, arsenic, and selenium. These results are combined with previously reported atomic mass data in order to study atomic mass trends in the region $28 \leqslant n \leqslant 50$ and $28 \leqslant Z \leqslant 40$. The only pronounced mass effects which occur in this region are those associated with 28 and 50 nucleons. We have found no extra stability which can be associated with the filling of the $f_{5/2}$, $p_{3/2}$, and $p_{1/2}$ subshells. A list of mass values used in this study is included.

I. INTRODUCTION

Some time ago one of us gave a summary (10) of the atomic mass evidence for the existence of certain notably stable nuclear configurations. These stable configurations or "nuclear shells" were attributed to the presence in the nucleus of 28, 50, or 82 protons, or 50, 82, or 126 neutrons, in agreement with the predictions of the single particle nuclear model of Mayer (34, 35) and Haxel, Jensen, and Suess (24). Since that time the mass effect associated with the closure of the 28- and 50-proton shells has been confirmed by Nier's group at the University of Minnesota, who have also demonstrated (8) that there is atomic mass evidence for a 28-neutron shell.

These pronounced mass effects are *all* explained in terms of a spin-orbit coupling which results in large splitting of a nuclear energy level with orbital angular momentum l into two distinct levels $j = l \pm \frac{1}{2}$. Thus, the 28, 50, 82, and 126 shells mark the divisions between the $f_{7/2}-f_{5/2}$, $g_{9/2}-g_{7/2}$, $h_{11/2}-h_{9/2}$, and $i_{13/2}-i_{11/2}$ groups, respectively.

It is now of interest to determine the degree of stability which is associated with the filling of nuclear shells other than those resulting from strong spin-orbit coupling. Probably the best region in which to study this matter is that where $28 < n < 50$ and $28 < Z < 40$, which extends from nickel to zirconium. Here is a region which is almost entirely free of major shell effects and, for this reason, is well suited to the study of effects which are presumably smaller than those which have been observed to date. At the same time, it is a region in which three subshells, namely, $f_{5/2}$, $p_{3/2}$, and $p_{1/2}$, are filled. In this paper we report new atomic mass measurements in this region, and combine these with existing data in order to investigate the nuclear stability variations in which we are interested.

II. EXPERIMENTAL

The new atomic mass measurements upon which this paper is based were made with a Dempster-type double focusing mass spectrograph. Both the instrument (9) and the method (26) have been previously described in some detail.

The mass differences obtained in the present work are given in Table I.

TABLE I

LIST OF NEW ATOMIC MASS DIFFERENCES

Nuclides	Mass difference in m.m.u.	Previous measurements
$Pb^{207} - 3Ga^{69}$	196.6 ± 6	
$Ce^{140} - 2Ge^{70}$	56.8 ± 6	59.5 ± 4 [a]
$Pr^{141} - 3Ti^{47}$	50.9 ± 3	51.3 ± 4 [a]
$Nd^{144} - 3Ti^{48}$	66.7 ± 3	
$Nd^{144} - 2Ge^{72}$	66.3 ± 2	69.8 ± 10 [a]
$2Ge^{72} - 3Ti^{48}$	0.4 ± 4	
$Nd^{150} - 3Ti^{50}$	85.2 ± 5	77.4 ± 17 [b]
$Nd^{150} - 2As^{75}$	77.1 ± 4	
$2As^{75} - 3Ti^{50}$	8.1 ± 6	
$Sm^{152} - 2Ge^{76}$	76.2 ± 2	
$Sm^{152} - 2Se^{76}$	81.4 ± 6	
$Ge^{76} - Se^{76}$	2.6 ± 3	
$Gd^{156} - 3Cr^{52}$	100.4 ± 4	99.4 ± 17 [b]
$Gd^{156} - 2Se^{78}$	87.5 ± 2	
$2Se^{78} - 3Cr^{52}$	12.9 ± 4	

[a] *Reference (12).*   [b] *Reference (20).*

III. STANDARD MASSES

In computing the masses of the nuclides with which we are concerned in this paper we have regarded the masses of certain of the lighter nuclides as substandards, in particular, H^1 and C^{12}. This has necessitated choosing between the masses for these nuclides computed by Li *et al.* (29) on the basis of nuclear reaction data, and those obtained by mass spectroscopic methods by Nier and his collaborators (7) and by Ogata and Matsuda (37). Since we shall be making use of many other masses obtained by Nier and his group, we have chosen to base all of our present calculations on their masses for the substandards. These values are

$$H^1 = 1.008146 \pm 3 \text{ a.m.u.,}$$

$$C^{12} = 12.003842 \pm 4 \text{ a.m.u.}$$

The accuracy of the new mass comparisons described in this paper is such that the use of the reaction-derived values of $H^1 = 1.008142 \pm 3$ a.m.u. and $C^{12} = 12.003804 \pm 17$ a.m.u. would generally make inconsequential changes in the atomic masses computed therefrom. These changes would never be outside the probable errors associated with the masses in question.

IV. COMPUTATION OF ATOMIC MASSES

(a) *Argon, Potassium, Calcium, Scandium, Titanium, Vanadium, Chromium, Manganese, Iron, Nickel, Copper, and Zinc*

The masses of all the stable isotopes of these elements, with the exception of K^{40} and Ca^{46}, have been accurately measured by Collins, Nier, and Johnson (7, 8) and have been used by them to study the stability effects associated with the 28-proton and 28-neutron shells. We had previously measured a number of these masses in our laboratory and find that the agreement is generally good between the new measurements and our older, less accurate ones. The two sets of measurements of the eight nuclides which have been studied in both labora-

tories are shown in Table II. These masses are based in each case on H^1 = 1.008146 $\pm$ 3 a.m.u. and C^{12} = 12.003842 $\pm$ 4 a.m.u.

TABLE II

COMPARISON OF MEASURED MASSES FOR SOME NUCLIDES OF
TITANIUM, CHROMIUM, IRON, AND NICKEL

Nuclide	Collins, Nier, and Johnson[a] (a.m.u.)	Duckworth *et al.* (a.m.u.)	
Ti^{48}	47.96317 $\pm$ 6	47.9630 $\pm$ 3	[b]
Cr^{50}	49.96210 $\pm$ 6	49.9602 $\pm$ 2	[c]
Cr^{52}	51.95707 $\pm$ 9	51.9571 $\pm$ 2	[d]
Fe^{54}	53.95704 $\pm$ 5	53.9567 $\pm$ 2	[d]
Fe^{56}	55.95272 $\pm$ 10	55.95279 $\pm$ 17	[e]
Ni^{58}	57.95345 $\pm$ 10	57.95362 $\pm$ 18	[e]
Ni^{60}	59.94901 $\pm$ 29	63.94931 $\pm$ 14	[f]
Ni^{64}	63.94755 $\pm$ 8	63.94728 $\pm$ 16	[g]

[a]   *Reference (7, 8).*
[b]   *This is a new value resulting from a remeasurement of our old* $O^{16} - Ti^{48}$ *plates.*
[c]   *This is the mass we originally reported and is known to be in error. See Reference (11).*
[d]   *Reference (16).*
[e]   *Reference (14).*
[f]   *Reference (13).*
[g]   *Reference (12).*

In the light of this agreement, we conclude that the Minnesota mass values and ours are equivalent for this part of the mass table, albeit the Minnesota values are more accurate. We are, therefore, adopting in this paper the mass values obtained by Nier and his collaborators for the elements argon to zinc, except for the nuclides Fe^{56}, Ni^{58}, and Ni^{60}. In the case of this trio, weighted means seem to be called for: these are Fe^{56} = 55.95274 $\pm$ 9 a.m.u., Ni^{58} = 57.95349 $\pm$ 9 a.m.u., and Ni^{60} = 59.94925 $\pm$ 13 a.m.u.

(b) *Cobalt*

Cobalt consists of a single stable isotope at mass number 59. Its mass can be deduced from Ni^{60} = 59.94925 $\pm$ 13 a.m.u. (see above), knowing that $Co^{60} - Co^{59}$ = 1.00070 $\pm$ 5 a.m.u. (3, 23, 4) and $Co^{60} - Ni^{60}$ = 0.00302 a.m.u. (42), to be Co^{59} = 58.95136 $\pm$ 14 a.m.u. A second value for its mass can be deduced from Ni^{58} = 57.95349 $\pm$ 9 a.m.u. by using $Ni^{59} - Ni^{58}$ = 0.99930 $\pm$ 1 a.m.u. (23, 28), and McCue's figure (31) of 1.888 $\pm$ 0.003 Mev. for the $Co^{59}(p,n)$ threshold. These data lead to Co^{59} = 58.95164 $\pm$ 9 a.m.u., which is in fair agreement with the Ni^{60}-derived value. The weighted mean for Co^{59} = 58.95157 $\pm$ 10 a.m.u.

(c) *Gallium*

Gallium exists in two stable isotopic forms at mass numbers 69 (60.2%) and 71 (39.8%). We have determined the $Pb^{207} - 3 Ga^{69}$ mass difference as noted in Table I. Using Pb^{207} = 207.0405 $\pm$ 10 a.m.u. (40), we compute Ga^{69} = 68.9480 $\pm$ 4 a.m.u. This value agrees well with the mass of Ga^{69} computed from the Minnesota masses for Zn^{68} and Zn^{70} and appropriate transmutation data, as will now be shown. First, one can combine Zn^{68} = 67.94686 $\pm$ 7 a.m.u. (8) with the 10.10 $\pm$ 0.2 Mev. $Ga^{69}(\gamma, n)$ threshold (39) and the $Ga^{68} - Zn^{68}$ decay

energy, known to be 2.90 Mev. (42), to obtain $Ga^{69} = 68.94810 \pm 22$ a.m.u. Then, also, using $Zn^{70} = 69.94779 \pm 6$ a.m.u. (8), the $Zn^{70}(\gamma,n)$ threshold of 9.2 ± 0.2 Mev. (22), and the mass difference $Zn^{69}-Ga^{69} = 0.00092$ (42), one calculates $Ga^{69} = 68.94777 \pm 22$ a.m.u.

These three different values for the mass of Ga^{69} are in good agreement and lead to a weighted mean of $Ga^{69} = 68.94794 \pm 16$ a.m.u. It is not possible at present to compute a mass for Ga^{71}, the other stable isotope of gallium.

(d) Germanium, Arsenic, and Selenium

These three elements are being discussed together since they are linked by certain key transmutation data in addition to a mass spectrographic mass comparison.

Germanium has five stable isotopes—70(20.55%), 72(27.37%), 73(7.61%), 74(36.74%), and 76(7.67%). Arsenic has but one at mass number 75 while selenium consists of six—74(0.87%), 76(9.02%), 77(7.58%), 78(23.52%), 80(49.82%), and 82(9.19%).

The mass of As^{75} is found from the $2As^{75} - 3Ti^{50}$ mass difference listed in Table I and the mass $Ti^{50} = 49.96077 \pm 4$ a.m.u. (8) to be $As^{75} = 74.94522 \pm 30$ a.m.u. Kinsey and Bartholomew give 7.30 ± 0.04 Mev. for the energy (2) of the most energetic gamma ray following slow neutron capture in As^{75}. This will be assumed to represent the transition to the ground state of As^{76}. Combining these data with 3.12 Mev. (42) for the $As^{76} - Se^{76}$ decay energy, one obtains $Se^{76} = 75.94301 \pm 30$ a.m.u. A second value for this mass will now be computed.

The mass of Se^{78} is found from Table I and $Cr^{52} = 51.95707 \pm 9$ a.m.u. (8) to be $Se^{78} = 77.94210 \pm 22$ a.m.u. From the Chalk River (n,γ) experiments the $Se^{78}(\gamma,n)$ threshold has been found to be 10.483 ± 0.014 Mev. (2), whence $Se^{77} = 76.94438 \pm 22$ a.m.u. Further, Kinsey and Bartholomew give a probable value of 7.416 ± 0.009 Mev. for the $Se^{77}(\gamma,n)$ threshold (2). This leads to $Se^{76} = 75.94337 \pm 22$ a.m.u.

The weighted mean of these two values is $Se^{76} = 75.94324 \pm 18$ a.m.u. Assuming that this represents our best value for Se^{76}, we now adjust the previous values of As^{75}, Se^{77}, and Se^{78} to 74.9454 ± 3 a.m.u., 76.9442 ± 2 a.m.u., and 77.9420 ± 2 a.m.u., respectively.

The threshold for the $As^{75}(\gamma,n)$ reaction is 10.20 ± 0.2 Mev. (38, 39) and the resulting As^{74} decays both by positron and negatron emission. There is a total decay energy of 2.54 Mev. in the positron branch and 1.36 Mev. in the negatron branch (42). These data lead to $Se^{74} = 73.9460 \pm 4$ a.m.u. and $Ge^{74} = 73.9447 \pm 4$ a.m.u.

One may now use these masses for Se^{74} and Se^{78} together with ratios of the isotopic masses of selenium found in the microwave absorption experiments of Geschwind and others (19) to compute $Se^{80} = 79.9421 \pm 6$ and $Se^{82} = 81.9431 \pm 6$ a.m.u.

Turning now to germanium, the mass of Ge^{74} has been computed above, and that of Ge^{72} is found from Table I and $Ti^{48} = 47.96317 \pm 6$ a.m.u. (8) to be 71.94493 ± 20 a.m.u. These masses set the scale for the microwave-derived mass ratios for germanium (18) and lead through them to $Ge^{70} = 69.9464 \pm 7$ a.m.u. and $Ge^{76} = 75.9456 \pm 7$ a.m.u. These computed masses for Ge^{70}

and Ge^{76} will now be compared with ones that we have determined experimentally.

Using $Ti^{47} = 46.96668 \pm 10$ a.m.u. (8), 9.5 ± 0.2 Mev. for the $Pr^{141}(\gamma,n)$ threshold (22, 38), 3.22 Mev. for the total $Pr^{140} - Ce^{140}$ decay energy (42), together with the $Pr^{141} - 3Ti^{47}$ and $Ce^{140} - 2Ge^{70}$ mass differences given in Table I, one obtains $Ge^{70} = 69.9460 \pm 5$ a.m.u. The weighted mean of the two values for Ge^{70} is 69.9461 ± 4 a.m.u.

The mass of Ge^{76} may be obtained from Se^{76} using the mass spectrographic measurement of the $Ge^{76} - Se^{76}$ mass difference listed in Table I. This leads to $Ge^{76} = 75.9458 \pm 4$ a.m.u. which, with the microwave-derived value, gives a weighted mean of $Ge^{76} = 75.9457 \pm 4$ a.m.u.

These results indicate that the $Ge^{76} - Se^{76}$ mass difference is 0.0025 ± 4 a.m.u., or 2.3 ± 0.4 Mev. This leaves 0.8 Mev. available for the decay of As^{76} by K-capture, if the total energy for negatron decay is correctly given by 3.1 Mev. (42). Experimentally, the ratio of positrons to negatrons has been set at less than 0.007% (42).

(e) Bromine

There are two stable isotopes of bromine at mass numbers $79(50.52\%)$ and $81(49.48\%)$. We have not obtained mass spectrographic values for the masses of these nuclides. However, it is possible to compute the mass of Br^{79} from Se^{78} and that of Br^{81} from both Se^{80} and Se^{82}.

In the case of Br^{79}, one uses the $Q = 4.55 \pm 0.2$ Mev. for the $Se^{78}(p,n)$ reaction (5) and 10.7 ± 0.2 Mev. (32, 39) for the $Br^{79}(\gamma,n)$ threshold. In this way one computes $Br^{79} = 78.9435 \pm 4$ a.m.u.

In obtaining Br^{81} from Se^{80}, one makes use of $Q = 2.57 \pm 0.2$ Mev. for the $Se^{80}(p,n)$ reaction (5) and 10.07 ± 0.2 Mev. for the $Br^{81}(\gamma,n)$ threshold (32, 39). Thus, $Br^{81} = 80.9422 \pm 7$ a.m.u. In working from Se^{82}, one knows the $Se^{82}(\gamma,n)$ threshold to be 9.8 ± 0.5 Mev. (1) and the total $Se^{81} - Br^{81}$ decay energy to be 1.5 Mev. (42). In this way, $Br^{81} = 80.9430 \pm 8$ a.m.u. The weighted mean of these two values is 80.9425 ± 5 a.m.u.

There is good agreement between these computed masses for Br^{79} and Br^{81} and those obtained by Hays, Richards, and Goudsmit, who found, using their time-of-flight mass spectrometer (25), that $Br^{79} = 78.944 \pm 1$ a.m.u., and $Br^{81} = 80.943 \pm 1$ a.m.u.

(f) Krypton

There are six stable isotopes of krypton at mass numbers $78(0.354\%)$, $80(2.27\%)$, $82(11.56\%)$, $83(11.5\%)$, $84(56.90\%)$, and $86(17.37\%)$. Collins has obtained masses (6) for all of these isotopes. The masses of Kr^{82}, Kr^{84}, and Kr^{86} had been previously measured in our laboratory (27) and, although there was good agreement between our value and that of Collins for Kr^{84}, there were large discrepancies in the cases of Kr^{82} and Kr^{86}. We have re-examined the plates from which these measurements were made and have remeasured them. The results of the new measurements on these plates are compared in Table III with Collins' values.

The actual doublet measurements upon which these new masses are based are: $2C_3H_6 - Kr^{82}$, $\Delta m = 0.1653 \pm 3$ a.m.u.; $2C_3H_6 - Kr^{84}$, $\Delta m = 0.1826 \pm 3$

TABLE III

COMPARISON OF MASSES FOR Kr^{82}, Kr^{84}, AND Kr^{86}

Nuclide	Collins	New measurements (a.m.u.)
Kr^{82}	81.93961 ± 11	81.9392 ± 4
Kr^{84}	83.93836 ± 9	83.9382 ± 4
Kr^{86}	85.93820 ± 8	85.9384 ± 4

a.m.u.; $\frac{2}{3}Xe^{129} - Kr^{86}$, $\Delta m = 0.0255 \pm 3$ a.m.u. In computing the mass of Kr^{86} we have used $Xe^{129} = 128.94594 \pm 15$ a.m.u., which is a weighted mean of Halsted's 128.9460 ± 2 a.m.u. (21) and our earlier value (27) of 128.94570 ± 26 a.m.u.

These new measurements remove two worrisome discrepancies and justify the assumption that Collins' masses for krypton are compatible with masses got by us in this region.

(g) Rubidium

The only masses available for the two stable isotopes of rubidium, Rb^{85} and Rb^{87}, have been obtained by Hays, Richards, and Goudsmit (25). These do not appear to be consistent with the other masses which have been determined in this region and we are, consequently, not including them in the present set.

(h) Strontium, Yttrium, and Zirconium

Strontium exists in four stable isotopic forms at mass numbers $84(0.56\%)$, $86(9.86\%)$, $87(7.02\%)$, and $88(82.56\%)$. Preliminary measurements of the masses of Sr^{86} and Sr^{88} were made in 1937 by Mattauch (33). Recently, the mass of Sr^{86} has been found, by a study of the $C_3H_7 - Sr^{86}$ and $C_2OH_3 - Sr^{86}$ doublets, to be 85.93552 ± 52 a.m.u., and that of Sr^{88} has been found, by a study of the $CO_2 - Sr^{88}$ doublet, to be 87.93364 ± 35 a.m.u. (15).

The $Sr^{87} - Sr^{86}$ mass difference can be computed using Harvey's Q of 6.29 ± 0.2 Mev. (23) for the $Sr^{86}(d,p)$ reaction, and, also, using 8.40 ± 0.20 Mev. (39) for the $Sr^{87}(\gamma,n)$ threshold, as measured by Sher et $al.$ These two values are 0.99984 ± 21 a.m.u. and 0.99996 ± 21 a.m.u. respectively, giving a weighted mean of 0.99990 ± 15 a.m.u.

The $Sr^{88} - Sr^{87}$ mass difference can be computed from the $Sr^{88}(\gamma,n)$ threshold. This has been measured by Sher et $al.$ to be 11.15 ± 0.20 Mev. (39), corresponding to a mass difference of 0.99700 ± 21 a.m.u. This datum, combined with the information in the previous paragraph, leads to a $Sr^{88} - Sr^{86}$ mass difference of 1.99690 ± 29 a.m.u., which is in poor agreement with the mass spectrographic value of 1.99812 ± 63 a.m.u. This difficulty will be dealt with later after a discussion of the mass of Zr^{90} and the $Zr^{90} - Sr^{88}$ mass difference, which information is useful in assessing the reliability of the masses of Sr^{86} and Sr^{88}.

There are five stable isotopes of zirconium at mass numbers $90(51.46\%)$, $91(11.23\%)$, $92(17.11\%)$, $94(17.40\%)$, and $96(2.80\%)$. The mass of Zr^{90} has been determined mass spectrographically (13), by photographing the $Si^{30} - Zr^{90}$ doublet, to be 89.93286 ± 36 a.m.u. To ascertain the compatibility of this value

with the Sr^{88} mass given above, one can compute the $Zr^{90} - Sr^{88}$ mass difference as follows:

$$Sr^{89} - Sr^{88} = 1.00194 \pm 21 \text{ a.m.u.} \qquad \text{Reference (23)}$$
$$Sr^{89} - Y^{89} = 0.00161 \qquad\qquad\qquad \text{Reference (42)}$$

(a) $\quad Y^{89} - Sr^{88} = 1.00033 \pm 21 \text{ a.m.u.}$

$$Zr^{90} - Zr^{89} = 0.99620 \pm 32 \qquad\qquad \text{Reference (38)}$$
$$Zr^{89} - Y^{89} = 0.00303 \qquad\qquad\qquad \text{Reference (42)}$$

(b) $\quad Zr^{90} - Y^{89} = 0.99923 \pm 32$

$$Zr^{90} - Zr^{89m} = 0.99578 \pm 16 \qquad\qquad \text{References (22, 38)}$$
$$Zr^{89m} - Y^{89} = 0.00364 \qquad\qquad\qquad \text{Reference (42)}$$

(c) $\quad Zr^{90} - Y^{89} = 0.99942 \pm 16$

In this way $Zr^{90} - Sr^{88} = 1.99968 \pm 25$ a.m.u.—(a) plus weighted means of (b) and (c).

This mass difference is to be compared with the mass spectrographic value of 1.9992 ± 5 a.m.u. Since the agreement here is satisfactory, whereas it was not so in the case of the $Sr^{88} - Sr^{86}$ difference, we are assuming that the Sr^{86} mass is in error. We should have liked to remeasure the Sr^{86} doublets in order to justify this assumption, but the plates upon which they are recorded have unfortunately been misplaced. We have, therefore, adjusted the values for Sr^{88} and Zr^{90} in the light of the transmutation value for the $Zr^{90} - Sr^{88}$ mass difference. The results of this adjustment are shown in Table IV. From these adjusted values, using the transmutation results quoted above, one computes $Sr^{86} = 85.9366 \pm 6$ a.m.u., $Sr^{87} = 86.9365 \pm 4$ a.m.u., and $Y^{89} = 88.9336 \pm 4$ a.m.u., the latter being the single stable isotope of yttrium. It is, unfortunately, not possible to compute a mass for the remaining stable isotope of strontium, namely Sr^{84}.

TABLE IV

COMPARISON OF UNADJUSTED AND ADJUSTED MASSES
FOR Sr^{88} AND Zr^{90}

Nuclides	Unadjusted values	Adjusted values
Sr^{88}	87.93364 ± 35	87.9335 ± 4
$Zr^{90} - Sr^{88}$	1.99968 ± 25	1.99958 ± 20
Zr^{90}	89.93286 ± 36	89.9330 ± 4

Harvey has determined (23) the Q's of the $Zr^{90}(d,p)$ and $Zr^{91}(d,p)$ reactions to be 4.93 ± 0.05 Mev. and 6.50 ± 0.10 Mev., respectively. These values lead to the masses $Zr^{91} = 90.9343 \pm 4$ a.m.u. and $Zr^{92} = 91.9339 \pm 4$ a.m.u. The masses of Zr^{94} and Zr^{96} can be found from those of Mo^{94} and Mo^{96} (see next section) using $Zr^{94} - Mo^{94} = 0.00122 \pm 20$ a.m.u. and $Zr^{96} - Mo^{96} = 0.00363 \pm 28$ a.m.u. (17). The resulting values are $Zr^{94} = 93.9365 \pm 5$ a.m.u. and $Zr^{96} = 95.9394 \pm 5$ a.m.u.

(i) Nb^{93}, Mo^{92}, Mo^{94}, Mo^{96}, and Ru^{96}

For the purpose of this paper it is also desirable to compute masses for Nb^{93}, Mo^{92}, Mo^{94}, Mo^{96}, and Ru^{96} in order to determine more accurately the stability associated with stable nuclides possessing 50 and 52 neutrons.

The mass of Nb^{93} can be deduced from that of Zr^{92} using 8.7 ± 0.2 Mev. for the $Nb^{93}(\gamma,n)$ threshold (39) and 1.8 ± 0.2 Mev. for the $Nb^{92} - Zr^{92}$ mass difference (17). The mass so deduced is $Nb^{93} = 92.9355 \pm 4$ a.m.u.

A recent measurement of the $Mo^{92} - Zr^{92}$ mass difference has given 1.25 ± 0.2 Mev. (17), hence, $Mo^{92} = 91.9352 \pm 4$ a.m.u. The mass of Mo^{94} can be calculated from that of Nb^{93} knowing that $Q = 5.03 \pm 0.10$ Mev. for the $Nb^{93}(d,p)$ reaction (23) and that 1.26 Mev. represents the total $Nb^{94} - Mo^{94}$ decay energy (42). This leads to the value $Mo^{94} = 93.9353 \pm 4$ a.m.u. The mass of Mo^{96} has been found mass spectrographically to be $Mo^{96} = 95.9358 \pm 4$ a.m.u. (13).

Finally, the mass of Ru^{96} is found, by combining the recent value $Ru^{96} - Mo^{96} = 2.8 \pm 0.2$ Mev. (17) with the mass of Mo^{96}, to be $Ru^{96} = 95.9388 \pm 4$ a.m.u.

TABLE V

ATOMIC MASSES ADOPTED IN THIS PAPER

A^{40}	$39.97513 \pm$	3	Ni^{60}	59.94925 ± 13		Br^{81}	$80.9425 \pm$	5
K^{41}	$40.97490 \pm$	4	Ni^{61}	60.94907 ± 23		Kr^{78}	77.94519 ± 18	
Ca^{40}	$39.97545 \pm$	9	Ni^{62}	$61.94681 \pm$	9	Kr^{80}	79.94246 ± 11	
Ca^{42}	$41.97216 \pm$	4	Ni^{64}	$63.94755 \pm$	7	Kr^{82}	81.93961 ± 11	
Ca^{43}	$42.97251 \pm$	6	Cu^{63}	$62.94926 \pm$	6	Kr^{83}	$82.9419 \pm$	5
Ca^{44}	$43.96924 \pm$	6	Cu^{65}	$64.94835 \pm$	6	Kr^{84}	$83.93836 \pm$	9
Ca^{48}	47.96778 ± 10		Zn^{64}	$63.99455 \pm$	2	Kr^{86}	$85.93820 \pm$	8
Sc^{45}	$44.97010 \pm$	5	Zn^{66}	$65.94722 \pm$	6	Rb^{85}		
Ti^{46}	$45.96697 \pm$	5	Zn^{67}	$66.94815 \pm$	6	Rb^{87}		
Ti^{47}	46.96668 ± 10		Zn^{68}	$67.94686 \pm$	7	Sr^{84}		
Ti^{48}	$47.96317 \pm$	6	Zn^{70}	$69.94779 \pm$	6	Sr^{86}	$85.9366 \pm$	6
Ti^{49}	$48.96358 \pm$	5	Ga^{69}	$68.9478 \pm$	2	Sr^{87}	$86.9365 \pm$	4
Ti^{50}	$49.96077 \pm$	4	Ga^{71}			Sr^{88}	$87.9335 \pm$	4
V^{50}	49.96330 ± 12		Ge^{70}	$69.9461 \pm$	4	Y^{89}	$88.9336 \pm$	4
V^{51}	$50.96052 \pm$	5	Ge^{72}	$71.9449 \pm$	2	Zr^{90}	$89.9330 \pm$	4
Cr^{50}	$49.96210 \pm$	7	Ge^{73}			Zr^{91}	$90.9343 \pm$	4
Cr^{52}	$51.95707 \pm$	9	Ge^{74}	$73.9447 \pm$	4	Zr^{92}	$91.9339 \pm$	4
Cr^{53}	$52.95772 \pm$	8	Ge^{76}	$75.9457 \pm$	4	Zr^{94}	$93.9365 \pm$	5
Cr^{54}	$53.9563 \pm$	2	As^{75}	$74.9454 \pm$	3	Zr^{96}	$95.9394 \pm$	5
Mn^{55}	54.95581 ± 10		Se^{74}	$73.9460 \pm$	4	Nb^{93}	$92.9355 \pm$	4
Fe^{54}	$53.95704 \pm$	5	Se^{76}	$75.9432 \pm$	2	Mo^{92}	$91.9352 \pm$	4
Fe^{56}	$55.95274 \pm$	9	Se^{77}	$76.9442 \pm$	2	Mo^{94}	$93.9353 \pm$	4
Fe^{57}	56.95359 ± 10		Se^{78}	$77.9420 \pm$	2	Mo^{96}	$95.9358 \pm$	4
Fe^{58}	$57.9520 \pm$	4	Se^{80}	$79.9421 \pm$	6	Ru^{96}	$95.9388 \pm$	4
Co^{59}	58.95157 ± 10		Se^{82}	$81.9431 \pm$	6			
Ni^{58}	$57.95349 \pm$	9	Br^{79}	$78.9435 \pm$	4			

V. DISCUSSION

(a) Mass Values

The atomic mass values adopted in this paper are shown in Table V. Each of these has been discussed in the previous text.

(b) Representation of the Data

Since Table V contains a fairly complete list of the stable isotopic masses in the region $28 \leqslant n \leqslant 50$ and $28 \leqslant Z \leqslant 40$, it should be possible to use this

information to study nuclear shell effects. In attempting to do this, we have
represented the data in several different ways, the most revealing of which
appears to be that shown in Figs. 1 and 2. In these figures we have plotted as
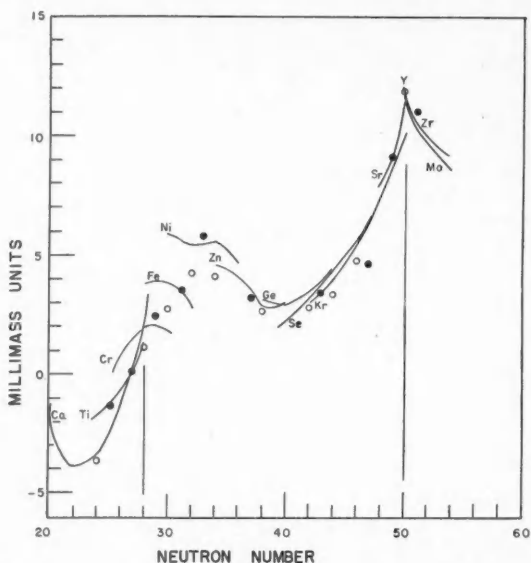

FIG. 1.   A plot of neutron number versus experimental deviation from semiempirical masses.
The solid curves connect all even-A isotopes for the elements shown. The closed circles belong
to even-Z and odd-n nuclides. As can be seen from Table V, the uncertainty in the plotted
points is generally less than 0.5 m.m.u. and, in the case of the Minnesota mass values, is very
much less than this figure.

ordinate the difference between the masses computed from the semiempirical
mass formula by Metropolis and Reitweisner (36) and the observed masses.
These differences are shown in Fig. 1 as a function of the number of neutrons in
the nucleus, and in Fig. 2 as a function of the number of protons. Similar plots
have been employed by Low and Townes (30) and by Wapstra (41).

(c) Analysis of Figs. 1 and 2 for Shell Structure Effects

The large sharp peaks occurring at neutron number 50 and proton number 28
are immediately apparent in Figs. 1 and 2, respectively. These have been previ-
ously ascribed to the spin-orbit splitting of the $g_{9/2}$–$g_{7/2}$ neutron levels and
$f_{7/2}$–$f_{5/2}$ proton levels. The mass effect associated with the 28-neutron magic
number is also apparent in Fig. 1, although partially obscured by the 28-proton
shell, which is a much larger effect.

This strong spin-orbit coupling model of the nucleus (34, 35, 24) seems to be
the most useful guide in the study of nuclear shell effects. On this scheme the
$f_{7/2}$ shell (completed at 28 nucleons) is followed by three subshells before the
$g_{9/2}$ shell (completed at 50 nucleons) begins. These subshells are $f_{5/2}$, $p_{3/2}$, and

$p_{1/2}$ and, if completed in this order, they represent nucleon numbers 34, 38, and 40, respectively. We shall examine Figs. 1 and 2 for mass effects at these numbers.
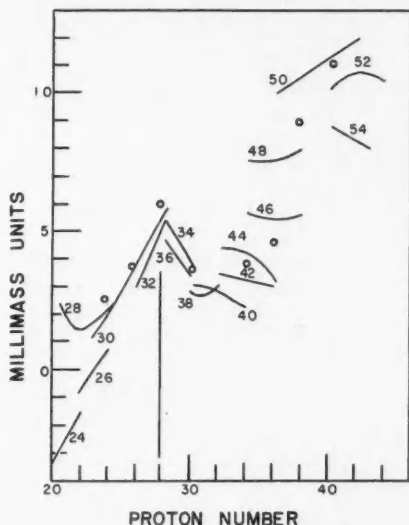

FIG. 2.   A plot of proton number versus experimental deviation from semiempirical masses. The solid curves connect even-A nuclides for the isotonic numbers shown. The circles belong to nuclides having even Z and odd neutron number. The uncertainty in the points is the same as in Fig. 1.

34 Nucleons

A small effect may be trying to assert itself at 34 neutrons in the nickel isotope curve as shown in Fig. 1. However, if instead of the directly determined mass of Ni^{62}, we use the value computed from Cu^{63}, taking the $Cu^{63}(\gamma,n)$ threshold to be 10.85 ± 0.20 Mev. (39), and assuming that the 0.56 Mev. γ-ray follows the 2.89 Mev. positron (42) in the decay of Cu^{62}, the point at 34 neutrons drops and a smooth curve results. The nickel curve then has a shape typical of that region and no shell effect appears.*

We have previously noted (9) that the most stable nuclide of all, in terms of binding energy per nucleon, is Ni^{62}. In the light of Figs. 1 and 2 this stability must be attributed first and foremost to its 28-proton configuration, and, second, to its position near the center of the normal distribution of the nickel isotopes. The stability due to this latter effect must be credited, therefore, to the accident of its birth, and not to its possessing 34 neutrons.*

Fig. 2 gives no indication of a subshell at 34 protons.

*Note added in proof: We have just learned from Prof. Leon Katz (July 29, 1953) that he has found the $Cu^{63}(\gamma,n)$ threshold to be 10.62 Mev., in exact agreement with the new value reported by Dr. Leo Seren at the 1953 Washington Meeting of the American Physical Society. With this datum the Cu^{63}-derived value for the mass of Ni^{62} becomes identical with the directly determined one. Thus, there may be evidence in Fig. 1 for a slight extra stability associated with the 34 neutron configuration.

38 and 40 Nucleons

The zinc curve in Fig. 1 shows a minimum at 38 and a rise toward 40 neutrons. It is unlikely that this is a real effect since, in obtaining the mass of Ga^{69} from Zn^{68} and Zn^{70}, a mass of Zn^{68} which is a little smaller and a mass of Zn^{70} which is a little larger would give values more in keeping with the directly determined value. These calculations have been discussed above in Section IV (c). Such changes would smooth out the zinc curve and remove the only indication for a shell effect in the region of 38 or 40 neutrons.

An examination of Fig. 2 shows that any effect existing at 38 or 40 protons is masked by the strong 50-neutron influence.

40–50 Neutrons

In this region the curves of Fig. 1 rise smoothly and no subshells are found or expected. This suggests that the 10 $g_{9/2}$ levels are filling in regularly.

32 Nucleons

Since the $f_{7/2}$–$f_{5/2}$ levels are widely split, it is quite likely that the $p_{3/2}$ levels fill in before the $f_{5/2}$. If so, a subshell would exist at 32 nucleons. There is possibly in Fig. 2 a vague suggestion of extra stability at 32 protons, but this may disappear when more accurate mass measurements become available.

From Fig. 1, 32 neutrons appears to be a particularly unfavored configuration as far as stability is concerned.

(d) Correctness of the δ-Term in the Semiempirical Mass Formula

In Fig. 1 the even-A isotopes of the even-Z elements are connected by solid lines. The position of the odd-A isotopes of these elements (indicated by closed circles) with respect to these solid lines is indicative of the correctness of the δ-term employed by Metropolis and Reitweisner in their calculations (36) based on the semiempirical mass formula. One sees, when he examines Fig. 1 with this point in mind, that there is no regular error in the δ-term, and that it approximates reality fairly well in this region. The deviations which do exist, although rather larger than the experimental error, do not appear to be unequivocally associated with shell structure.

(e) Summary

The only noticeable mass effects which occur in the region $28 \leqslant n \leqslant 50$ and $28 \leqslant Z \leqslant 40$ are those associated with 28 and 50 nucleons. These are properly attributed to the wide spin-orbit splitting of nuclear levels with high orbital angular momentum. We have found no extra stability which can be associated with the filling of the $f_{5/2}$, $p_{3/2}$, and $p_{1/2}$ subshells.

VI. ACKNOWLEDGMENTS

We have appreciated the privilege of using in Section IV (*d*) certain pre-publication data obtained by Dr. B. B. Kinsey and Dr. G. A. Bartholomew in their studies of neutron-capture γ-rays. Also, we are indebted to Dr. A. O. Nier and Dr. T. L. Collins for informal information received during the course of these experiments.

REFERENCES

1. BALDWIN, G. C. and KOCH, H. W.   Phys. Rev. 67: 1.   1945.
2. BARTHOLOMEW, G. A.   Private communication, April 21, 1953.
3. BARTHOLOMEW, G. A. and KINSEY, B. B.   Phys. Rev. 89: 386.   1953.
4. BATESON, W. O. and POLLARD, E.   Phys. Rev. 79: 241.   1950.
5. BLASER, J. P., BOEHM, F., MARMIER, P., and SCHERRER, P.   Helv. Phys. Acta, 24: 441. 1951.
6. COLLINS, T. L.   Paper 7 *in* Mass spectroscopy in physics research.   Natl. Bur. Standards, Circ. 522.   1953.
7. COLLINS, T. L., NIER, A. O., and JOHNSON, W. H., Jr.   Phys. Rev. 84: 717.   1951.
8. COLLINS, T. L., NIER, A. O., and JOHNSON, W. H., Jr.   Phys. Rev. 86: 408.   1952.
9. DUCKWORTH, H. E.   Rev. Sci. Instruments, 21: 54.   1950.
10. DUCKWORTH, H. E.   Nature, 170: 158.   1952.
11. DUCKWORTH, H. E.   Paper 5 *in* Mass spectroscopy in physics research. Natl. Bur. Standards, Circ. 522.   1953.
12. DUCKWORTH, H. E., KEGLEY, C. L., OLSON, J. M., and STANFORD, G. S.   Phys. Rev. 83: 1114.   1951.
13. DUCKWORTH, H. E., PRESTON, R. S., and WOODCOCK, K. S.   Phys. Rev. 79: 188.   1950.
14. DUCKWORTH, H. E. and PRESTON, R. S.   Phys. Rev. 79: 402.   1950.
15. DUCKWORTH, H. E. and PRESTON, R. S.   Phys. Rev. 82: 468.   1951.
16. DUCKWORTH, H. E., WOODCOCK, K. S., and PRESTON, R. S.   Phys. Rev. 78: 479.   1950.
17. GEIGER, J. S., HOGG, B. G., DUCKWORTH, H. E., and DEWDNEY, J. W.   Phys. Rev. 89: 621.   1953.
18. GESCHWIND, S. and GUNTHER-MOHR, R.   Phys. Rev. 81: 882.   1951.
19. GESCHWIND, S., MINDEN, H., and TOWNES, C. H.   Phys. Rev. 78: 174.   1950.
20. GRAVES, A. C.   Phys. Rev. 55: 863.   1939.
21. HALSTED, R. E.   Phys. Rev. 88: 666.   1952.
22. HANSON, A. O., DUFFIELD, R. B., KNIGHT, J. D., DIVEN, B. C., and PALEVSKY, H.   Phys. Rev. 76: 578.   1949.
23. HARVEY, J. A.   Phys. Rev. 81: 353.   1951.
24. HAXEL, O., JENSEN, J. H. D., and SUESS, H. E.   Phys. Rev. 75: 1766.   1949.
25. HAYS, E. E., RICHARDS, P. I., and GOUDSMIT, S. A.   Phys. Rev. 84: 824.   1951.
26. HOGG, B. G. and DUCKWORTH, H. E.   Can. J. Phys. 30: 637.   1952.
27. KEGLEY, C. L. and DUCKWORTH, H. E.   Nature, 167: 1025.   1951.
28. KINSEY, B. B. and BARTHOLOMEW, G. A.   Phys. Rev. 89: 375.   1953.
29. LI, C. W., WHALING, W., FOWLER, W. A., and LAURITSEN, C. C.   Phys. Rev. 83: 512. 1951.
30. LOW, W. and TOWNES, C. H.   Phys. Rev. 80: 608.   1950.
31. McCUE, J. J. G. and PRESTON, W. M.   Phys. Rev. 84: 384.   1951.
32. McELHINNEY, J., HANSEN, A. O., BECKER, R. A., DUFFIELD, R. B., and DIVEN, B. C.   Phys. Rev. 75: 542.   1949.
33. MATTAUCH, J.   Naturwissenschaften, 25: 170.   1937.
34. MAYER, M. G.   Phys. Rev. 75: 1969.   1949.
35. MAYER, M. G.   Phys. Rev. 78: 16.   1950.
36. METROPOLIS, N. and REITWEISNER, G.   Table of atomic masses.   Unpublished, 1950.
37. OGATA, K. and MATSUDA, H.   Phys. Rev. 89: 27.   1953.
38. OGLE, W. E., BROWN, L. J., and CARSON, A. N.   Phys. Rev. 78: 63.   1950.
39. SHER, R., HALPERN, J., and MANN, A. K.   Phys. Rev. 84: 387.   1951.
40. STANFORD, G. S., DUCKWORTH, H. E., HOGG, B. G., and GEIGER, J. S.   Phys. Rev. 85: 1039.   1952.
41. WAPSTRA, A. H.   Phys. Rev. 84: 838.   1951.
42. WAY, K., FANO, L., SCOTT, M. R., and THEW, K.   Nuclear data.   Natl. Bur. Standards, Circ. 499.   1950, and supplements.

DETERMINATION OF RATES OF CHANGE OF POLARIZABILITY FROM RAMAN AND RAYLEIGH INTENSITIES[1]

By E. J. STANSBURY,[2] M. F. CRAWFORD, AND H. L. WELSH

ABSTRACT

Mean values of the rate of change of polarizability with respect to internuclear distance were determined for several molecules from the ratio of Raman and Rayleigh intensities in the gas. The values obtained are: hydrogen, 1.2×10^{-16} cm.²; deuterium, 1.1; hydrogen chloride, 1.0; hydrogen bromide, 1.2; nitrogen, 1.6; oxygen, 1.4; carbon dioxide (ν_1 vibration), 4.2; methane (ν_1 vibration), 4.1. It is noteworthy that the values for the partially ionic molecules, hydrogen chloride and hydrogen bromide, are nearly the same as for hydrogen and deuterium.

INTRODUCTION

In the polarizability theory of the Raman effect, as developed by Placzek (11), the intensity of the vibrational Raman band of a diatomic molecule depends on invariants of the tensor quantity

$$\alpha_{ij}' = (d\alpha_{ij}/dr)_0$$

where α_{ij} is the polarizability of the molecule and r the internuclear distance, the derivative being taken at the equilibrium position. The mean value, α', of the rate of change of polarizability appears as a molecular constant in other semiempirical theories, as, for example, in the recent treatment of induced infrared absorption, by van Kranendonk and Bird (13). The evaluation of α' for hydrogen has been the subject of a number of theoretical papers. Therefore its experimental determination is of some interest.

A direct determination of α' by the measurement of absolute Raman intensities is impractical; however, the difficulties are obviated to a large extent by using the ratio of the intensities of Raman and Rayleigh scattering in gases. This method was used by Bhagavantam (3, 4, 5, 6), who measured the Raman-Rayleigh intensity ratio for hydrogen, deuterium, nitrogen, oxygen, and carbon dioxide. Since Bhagavantam's value of α' for hydrogen is considerably lower than the values calculated by wave mechanics (Hirschfelder (8), Bell and Long (2)) and the value obtained indirectly from the difference in the refractive indices of hydrogen and deuterium (Bell (1)), it seemed worth while to undertake a new determination of the Raman–Rayleigh intensity ratio for the simpler molecules. In these experiments particular care was used to eliminate the effects of stray light which is the main source of error in the method. The diatomic molecules investigated were hydrogen, deuterium, nitrogen, and oxygen, which have covalent binding, and hydrogen chloride and hydrogen bromide, which have partially ionic binding. In addition, the totally symmetric (ν_1) vibrations of carbon dioxide and methane were studied.

The ratio of Raman and Rayleigh intensities for transverse observation is given by

$$\frac{I_{\text{Raman}}}{I_{\text{Rayleigh}}} = \frac{(\nu - \omega_0)^4}{\nu^4} \frac{(45\alpha'^2 + 13\gamma'^2)}{(45\alpha^2 + 13\gamma^2)} \frac{h}{8\pi^2\mu\omega_e},$$

where ν is the frequency of the exciting radiation, ω_0 the vibrational Raman shift, α and γ^2 are the mean value and anisotropy of the polarizability tensor, α' and γ'^2 the corresponding invariants of the rate of change tensor, μ is the reduced mass of the molecule, and ω_e its frequency of vibration for infinitesimal amplitudes. The mean value of the polarizability can be determined from the refractive index, n, of the gas from the relation

$$n - 1 = 2\pi N\alpha,$$

where N is the number of molecules per cubic centimeter. The ratios, α'^2/γ'^2 and α^2/γ^2, can be calculated from the depolarization factors, ρ_{Raman} and ρ_{Rayleigh}, by means of the formulae,

$$\rho_{\text{Raman}} = \frac{6\gamma'^2}{45\alpha'^2 + 7\gamma'^2} \quad \text{and} \quad \rho_{\text{Rayleigh}} = \frac{6\gamma^2}{45\alpha^2 + 7\gamma^2}.$$

Thus, if n, ρ_{Raman}, and ρ_{Rayleigh}, and $I_{\text{Raman}}/I_{\text{Rayleigh}}$ are measured, $|\alpha'|$ can be determined.

In the formula given above the intensities of the rotational wings of both the Raman and Rayleigh bands are included. If the rotational lines are widely spaced it is advantageous to measure the ratio of the intensities of the Q branches alone. The formula then becomes

$$\frac{I_{\text{Raman}}}{I_{\text{Rayleigh}}} = \frac{(\nu - \omega_0)^4}{\nu^4} \frac{(45\alpha'^2 + 13x\gamma'^2)}{(45\alpha^2 + 13x\gamma^2)} \frac{h}{8\pi^2\mu\omega_e},$$

where x, the fraction of the anisotropic intensity in the Q branch, can be calculated from the probabilities for rotational transitions (Manneback (10), Placzek and Teller (12)).

The Raman intensities corresponding to the totally symmetric vibrations of the linear symmetric molecule XY_2 and the tetrahedral molecule XY_4 can also be expressed in terms of the invariants of a tensor α_{ij}', where the derivatives are taken only with respect to r, the length of the X–Y bond. The constant, μ, in the above formula is $2m$ for XY_2 and $4m$ for XY_4, where m is the mass of the Y atom.

EXPERIMENTAL

The Raman tube for gases, shown schematically in Fig. 1, reduced the stray light to a very low value. It was made from standard wall Pyrex tubing and was blackened on the outside except for the window and the illuminated section. Diaphragms of black glass, bevelled on the edges, were positioned in the front section to prevent light from the lamp from reaching the window directly or by reflection from the walls of the tube. The light trap, made by drawing out the rear end of the tube into a smooth cone, was well removed from the short illuminated section so that no direct light from the lamp could reach it. When
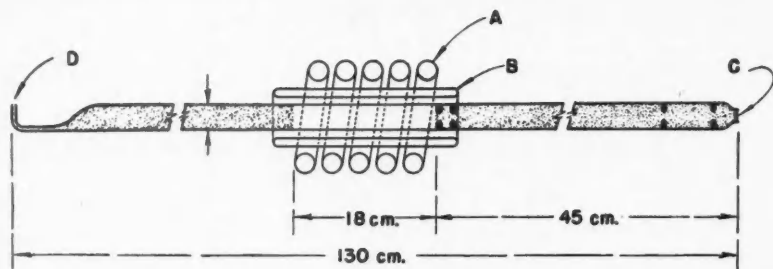
FIG. 1. The Raman tube used in the measurement of the ratio of Raman and Rayleigh intensities in gases. *A*, mercury lamp; *B*, water jacket; *C*, plane window; *D*, gas inlet.

the inside of the light trap was scrupulously clean, the stray light from the evacuated Raman tube was about one-tenth as intense as the Rayleigh scattering from oxygen at a pressure of seven atmospheres. Illumination was provided by a helical mercury arc with internal water cooling in the electrode pools (14). All gases except deuterium were of commercial purity and were introduced into the evacuated Raman tube through a tightly packed cotton wool plug which served to remove dust particles. Deuterium was prepared by the action of calcium metal on heavy water.

A condensing lens was used to image the front and back diaphragms of the Raman tube at the collimator lens and the slit of the spectrograph, respectively. Since high dispersion was not required and short exposure times were desirable, a glass spectrograph with an $F/4$ camera lens and a reciprocal linear dispersion of 225 cm.$^{-1}$ per mm. at $\lambda 4358$ was used.

To measure the Raman–Rayleigh intensity ratio, the Raman scattering, the Rayleigh scattering, and the stray light from the evacuated Raman tube were photographed in separate exposures on the same plate. Stepped slit spectra of a Kipp and Zonen standard lamp were used for the intensity calibration of the plates. In general five spectra were photographed on each plate.

(*a*) The Raman spectrum. The spectral slit width was from 10 to 40 cm.$^{-1}$ and the exposure time for Eastman 103aO spectroscopic plates was from one to eight hours depending on the gas.

(*b*) The Rayleigh spectrum. A group of Wratten filters, whose transmissions were measured with a photoelectric spectrograph, was used to reduce the intensity so that the exposure time was about one hour.

(*c*) The stray light spectrum. The intensity was adjusted by a group of Wratten filters to give the same exposure time as for the Rayleigh spectrum.

(*d*) The intensity calibration for the Raman spectrum. The exposure time was the same as (*a*).

(*e*) The intensity calibration for the Rayleigh spectrum. It was recorded with the same exposure time as (*b*) and (*c*).

The same slit width was used for each of the first three exposures, and the current in the mercury arcs was maintained at 13 ± 0.2 amp. The correct

densities were obtained in exposures (d) and (e) by adjusting the current in the standard lamp. Since the spectral distribution of intensity and its variation with current were known for the standard lamp, these exposures could be used to obtain the intensities of the Raman and Rayleigh lines on the same scale.

Densities were measured with a recording microphotometer. The profiles of the Raman, Rayleigh, and stray light lines were plotted on arbitrary intensity and frequency scales. The areas under the profiles were then corrected by factors determined from the transmissions of the Wratten filters, the intensities of the standard lamp, and the dispersion of the spectrograph, to give the relative intensities of the lines. Finally, the stray light intensity was subtracted from the observed Rayleigh intensity to give I_{Rayleigh}.

The random errors inherent in the photographic measurement of intensities were lessened by averaging the results from several plates for each gas. The Raman–Rayleigh intensity ratios determined from individual plates showed an average deviation from the mean in the range $\pm 3\%$ to $\pm 10\%$. Three values of the ratio for nitrogen obtained with $\lambda 4047$ as exciting line agreed well with five values obtained with $\lambda 4358$, when the frequency dependent factors were removed. The value of α' obtained for deuterium $(1.1 \times 10^{-16}$ cm.$^2)$ was in fair agreement with the value for hydrogen $(1.2 \times 10^{-16}$ cm.$^2)$, the small discrepancy probably being caused by the presence of impurities in the deuterium. The consistency shown by these results indicates that the methods of heterochromatic photometry used introduced no systematic error.

Some error in the measurement of the intensity ratio might be expected to arise from the light scattered by dust particles suspended in the gas. However, the measured Rayleigh intensities for the various gases, corrected for the stray light from the evacuated tube, and reduced to the same conditions of slit width and gas pressure, were found to be closely proportional to α^2. It was therefore concluded that there was no significant contribution to the Rayleigh intensities from light scattered by dust particles.

Since the illumination of the Raman tube was cylindrically symmetrical, the light scattered in the direction of observation was unpolarized and the measured intensity ratios were independent of the transmission characteristics of the spectrograph for polarized light. The conditions for transverse observation were not strictly satisfied, since the angle, θ, between the incident rays and the direction of observation had all values from about $30°$ to $150°$. For the angle θ the Raman–Rayleigh intensity ratio is

$$\frac{I_{\text{Raman}}(\theta)}{I_{\text{Rayleigh}}(\theta)}$$
$$= \frac{(\nu - \omega_e)^4}{\nu^4} \frac{(45\alpha'^2 + 7\gamma'^2)(I_s + I_p \cos^2\theta) + 6\gamma'^2 I_p \sin^2\theta}{(45\alpha^2 + 7\gamma^2)(I_s + I_p \cos^2\theta) + 6\gamma^2 I_p \sin^2\theta} \frac{h}{8\pi^2 \mu \omega_e},$$

where I_s and I_p are the components of the incident intensity with electric vector perpendicular and parallel, respectively, to the plane containing the incident ray and the direction of observation. I_s and I_p can be calculated by applying the Fresnel boundary conditions at the surfaces of the Raman tube and the water jacket, taking into account the inverse square law of intensity.

The observed intensity ratio corresponds to the value of $I_{Raman}(\theta)/I_{Rayleigh}(\theta)$ averaged over the possible values of θ. A calculation made for a slightly idealized Raman source showed that the effect of the oblique rays was not at all large; for the extreme case of completely depolarized Raman scattering and completely polarized Rayleigh scattering the Raman–Rayleigh ratio is depressed by only 15%. The Raman bands and lines (Q branches) used in the determination of α' were fairly highly polarized and the error caused by the oblique rays was not greater than 5% in the most unfavorable case. Since this is smaller than the experimental error, no correction for the effect of the oblique rays was made.

The data used in the reduction of the experimental results are given in Table I. The values of $\rho_{Rayleigh}$ except for hydrogen and deuterium are those quoted

TABLE I

DATA USED IN THE REDUCTION OF THE RESULTS

Gas	ω_e (cm.$^{-1}$)	$\alpha \times 10^{24}$ (cm.^{3})*	$\rho_{Rayleigh}$	ρ_{Raman}	x
H_2	4395	0.84	0.012	0.14	0.32
D_2	3118	0.84	0.012	0.14	0.25
HCl	2990	2.69	0.007	0.4	0.25
HBr	2650	3.71	0.008	0.4	0.25
N_2	2360	1.79	0.036	0.19	0.25
O_2	1580	1.63	0.065	0.26	0.25
CO_2	1340	2.69	0.097	0.20	—
CH_4	2914	2.67	0.000	0.00	—

Calculated from refractive indices for $\lambda 4358$ quoted in the International Critical Tables.

by Bhagavantam (6). For hydrogen and deuterium $\rho_{Rayleigh}$ has not been accurately determined; results of direct measurements, ranging from 0.009 to 0.038, have been given in the literature for hydrogen, and no results are available for deuterium. Although this constant has little effect on the derived values of α', $\rho_{Rayleigh}$ was determined for these gases, as a matter of interest per se, by measuring the relative intensities of the unshifted Rayleigh line and the rotational Raman lines. These experiments gave $\rho_{Rayleigh} = 0.014$ for hydrogen, and 0.010 for deuterium. The mean of these values was used in the determination of α' for both gases. For all the gases except deuterium, hydrogen chloride, and hydrogen bromide, ρ_{Raman} has been measured by Cabannes and Rousset (7).* The value of this constant for deuterium was assumed to be the same as that for hydrogen. The values for hydrogen chloride and hydrogen bromide, which have not been measured previously, were determined from the intensity ratios of the S branch lines and the Q branch of the Raman bands. Since α' was determined mainly from the isotropic scattering, it is not very sensitive to the accuracy of ρ_{Raman}.

RESULTS

The results are summarized in Table II. The wave length of the mercury radiation used to excite the Raman effect is given in the second column; in the

* Cabannes and Rousset measured the depolarization of the Q branch in hydrogen as 0.05 and calculated ρ_{Raman} by assuming that x (the fraction of the anisotropic scattering contained in the Q branch) is equal to 0.25. However, the correct value of x is 0.32.

TABLE II

RATIOS OF RAMAN AND RAYLEIGH INTENSITIES AND DERIVED CONSTANTS

Gas	Exciting line (Å)	$\dfrac{I_{Raman}}{I_{Rayleigh}} \dfrac{\nu^4}{(\nu - \omega_0)^4} \times 10^3$	$\alpha' \times 10^{16} (cm.^2)$	$\overline{(0\mid\alpha\mid1)^2} \times 10^{51}$ (cm.^{6})
H_2	4047	18	1.2	16
D_2	4047/4358	9	1.1	8
HCl	4047/4358	1.1	1.0	15
HBr	4047/4358	1.0	1.2	26
N_2	4047/4358	0.9	1.6	4.0
O_2	4358	1.1	1.4	4.4
$CO_2(\nu_1)$	4358	1.3	4.2	11
$CH_4(\nu_1)$	{ 4358	3.4	4.1	24
	4047/4358			

cases designated 4047/4358 the Rayleigh line at 4358Å was compared with the more conveniently placed Raman line excited by 4047Å and the intensity ratio was corrected by the factor, 1.65, determined from experiments with nitrogen for which both Raman lines could be measured easily. The observed intensity ratios are given in the form, $(I_{Raman}/I_{Rayleigh})\mid(\nu^4/(\nu - \omega_0)^4)$, which is independent of the frequency of the exciting light. For carbon dioxide and methane the total intensities of the bands were measured; for the other gases the intensities refer to the Q branches only. The ratios are higher than those of Bhagavantam (3, 4, 5) by a factor of about two in most cases; however, Bhagavantam (6) states that his results should be considered as giving only the order of magnitude correctly.

In addition to the derived values of α', the values of $\overline{(0\mid\alpha\mid1)^2} = (\alpha'^2 + 13\gamma'^2/45)$ $\times(h/8\pi^2\mu\omega_c)$ are given. The latter quantity, the square of the matrix element of the polarizability for the $1\leftarrow0$ vibrational transition averaged over all orientations of the molecule, is proportional to the total intensity of the Raman band. The values of $\overline{(0\mid\alpha\mid1)^2}$, which include all of the anisotropic intensity, can be considerably in error if ρ_{Raman} is not accurate; this is particularly true of the more highly depolarized bands.

The results given in Table II show that there is some correlation between α' and the multiplicity of the chemical bond; for the four compounds with a single bond the values of α' lie between 1.0 and 1.2×10^{-16} cm.[2] For oxygen with a double bond α' is 1.4×10^{-16} and for nitrogen with a triple bond α' is 1.6×10^{-16}. For polyatomic molecules α' increases with the number of bonds; thus, for carbon dioxide with two double bonds α' is 4.2×10^{-16} and for methane with four single bonds it is 4.1×10^{-16}. The degree of covalence of the bond appears to have little effect on α' since the values for the partially ionic molecules, hydrogen chloride and hydrogen bromide, are as large as that for hydrogen. It has usually been assumed that the Raman scattering from ionic compounds should be very weak.

Although the sign of α' cannot be determined from experiment, there is no doubt that the positive sign should be chosen. Quantum mechanical calculations show that α' is positive for hydrogen, and the isotope effect discussed by Bell (1) gives positive values for hydrogen, hydrogen chloride, hydrogen bromide,

and methane. The fact that the polarizability of the helium atom, the limiting case of the hydrogen molecule as $r \to 0$, is less than the polarizability of the hydrogen molecule indicates that α' is positive for hydrogen. Also, the polarizabilities of neon, argon, and krypton are less than the polarizabilities of methane, hydrogen chloride, and hydrogen bromide, respectively. It is therefore fairly certain that in general the polarizability increases with internuclear distance.

For four molecules studied in this investigation the value of α' has been calculated by Bell (1), using an ingenious method based on the difference in the refractive indices of isotopic compounds. If α and α_i are the polarizabilities obtained from the refractive indices of the isotopic molecules, α' is equal to $(\alpha - \alpha_i)/(\bar{x} - \bar{x}_i)$, where $\bar{x} = (r - r_e)$, the average departure from the equilibrium position in the $v = 0$ state, is calculated quantum mechanically from the cubic approximation to the Morse potential curve. Bell's results are compared with those obtained in the present investigation in Table III. The agreement is

TABLE III

Gas	Value of $\alpha' \times 10^{16}$ (cm.^{2})	
	From Raman–Rayleigh intensity ratios	From refractive indices of isotopic compounds (1)
H_2	1.2	1.68
HCl	1.0	1.23
HBr	1.2	1.07
CH_4	4.1	7.71

probably within the uncertainties in Bell's values which are sensitively dependent on the accuracy of the potential function used.

The value of α' for hydrogen is of particular interest since wave mechanical calculations of this constant have been made. The results of these calculations are compared in Table IV with the experimental results. The theoretical values

TABLE IV

VALUES OF α' FOR HYDROGEN

Method	$\alpha' \times 10^{16}$ (cm.^{2})
Raman and Rayleigh intensities	
Bhagavantam (4)	0.85
This investigation	1.2
Refractive indices of hydrogen and deuterium	
Bell (1)	1.68
Wave mechanical calculation	
Hirschfelder (8)	0.89–1.00
Bell and Long (2)	1.49
Ishiguro, Arai, Mizushima, and Kotani (9)	1.411

of α' have a considerable spread about the present experimental result. The most recent paper is by Ishiguro, Arai, Mizushima, Kotani (9) who have taken into account the mechanical and electrical anharmonicities of the molecule.

A comparison with the experimental results is best made through the Raman–Rayleigh intensity ratio; their theoretical value of $\nu^4 I_{Raman}/(\nu - \omega_0)^4 I_{Rayleigh}$ is 33.6×10^{-3}; the experimental value is 18×10^{-3}. It is unlikely that the experimental result is in error by as much as 90%.

REFERENCES

1. BELL, R. P. Trans. Faraday Soc. 38: 422. 1942.
2. BELL, R. P. and LONG, D. A. Proc. Roy. Soc. (London), A, 203: 364. 1950.
3. BHAGAVANTAM, S. Indian J. Phys. 6: 319, 557. 1931.
4. BHAGAVANTAM, S. Indian J. Phys. 7: 107, 549. 1932.
5. BHAGAVANTAM, S. Proc. Indian Acad. Sci. A, 2: 477. 1935.
6. BHAGAVANTAM, S. Scattering of light and the Raman effect. Andhra University, Waltair, India. 1940.
7. CABANNES, J. and ROUSSET, A. Compt. rend. 206: 85. 1938.
8. HIRSCHFELDER, J. O. J. Chem. Phys. 3: 555. 1935.
9. ISHIGURO, E., ARAI, T., MIZUSHIMA, M., and KOTANI, M. Proc. Phys. Soc. (London), A, 65: 178. 1952.
10. MANNEBACK, C. Z. Physik, 62: 224; 65: 574. 1930.
11. PLACZEK, G. Marx, Handbuch der Radiologie, VI (2). Akademische Verlagsgesellschaft m. b. H., Leipzig. 1934.
12. PLACZEK, G. and TELLER, E. Z. Physik, 81: 209. 1933.
13. VAN KRANENDONK, J. and BIRD, R. B. Physica, 17: 953. 1951.
14. WELSH, H. L., CRAWFORD, M. F., THOMAS, R. T., and LOVE, G. R. Can. J. Phys. 30: 577. 1952.

INTERPRETATION OF THE FLUCTUATING ECHO
FROM RANDOMLY DISTRIBUTED SCATTERERS. PART I[1]

By J. S. Marshall and Walter Hitschfeld

ABSTRACT

The radar echo from randomly distributed scatterers fluctuates in intensity about a mean equal to the sum of the intensities contributed by each particle. If k independent intensity values are averaged, the r.m.s. deviation of the fluctuation is reduced by a factor $\sqrt{k}$. Counting the fraction of signals falling above one or more thresholds is a practically simpler, though somewhat less rapid, alternative to averaging. As a further alternative, one can superimpose many independent sweeps of amplitude or signal level on an A-scope, and so observe the most probable value.

In range interval l, a single sweep contains $2l/h$ independent data, where h is the pulse length. The intensity averaged under the continuous trace is slightly more accurate than the average of the independent data.

Pulses sent through the same scatterers yield identical returns until the scatterers have had time to reshuffle themselves. Successive pulses give independent echoes, however, if their frequencies differ by about $1/\tau$, τ being the pulse duration. Echoes from the same pulse received at separate antennas are similarly independent.

Several (k) independent echo values are helpful in measuring steady echoes against a noise background. For fluctuating echoes, k must be large, regardless of the relative strengths of echo and background. Large values of k in addition materially enhance the detectability of fluctuating echoes weak compared to the noise.

1. INTRODUCTION

The radar echo from a random array of scatterers is "incoherent" and so the *average* intensity is well known to be the sum of the intensities from the individual scatterers. The random fluctuations of the signal about its average value provide an important limitation to the accuracy of the information obtainable.

The purpose of this paper is to investigate these fluctuations theoretically (and by analogue computation) with a view to establishing the extent of this limitation, and the improvements that may be effected by averaging or by modifying the method of pulsing and scanning.

The present approach is an elementary one. Mathematical proofs of some of the points raised are provided by Wallace (5).

2. PROBABILITY DISTRIBUTIONS

Let a signal $y = A \sin\omega t$ be generated at range $r = 0$, starting at time $t = 0$, and ending at time $\tau = h/c$, where c is the velocity of light. The quantities τ and h are the duration of the emitted pulse in time and its length in space; $\omega = 2\pi\nu$, where ν is the radio frequency. The resulting pulse of electromagnetic radiation is beamed by an antenna into a region containing scatterers. Some of the energy is scattered back towards the transmitting site, where it may be received by the transmitting antenna.

At any time $t > h/c$, the receiver will be receiving signals from all scatterers in the beam between distances $\frac{1}{2}ct$ and $\frac{1}{2}(ct - h)$. These signals will be distributed

randomly as to phase. Thus the region from which signals are being received at a particular instant is a section of the beam, of length along the beam $h/2$, and of cross-sectional area which we will denote by B. Every point in this region has a particular phase; i.e. the position of the scattering particle determines the phase of the signal received from it. The volume $Bh/2$ of the region is uniformly distributed over all possible phases. This region will be referred to as the "contributing region" for the time of reception t, or for the corresponding recorded range $r = \frac{1}{2}tc$ (see Fig. 1).
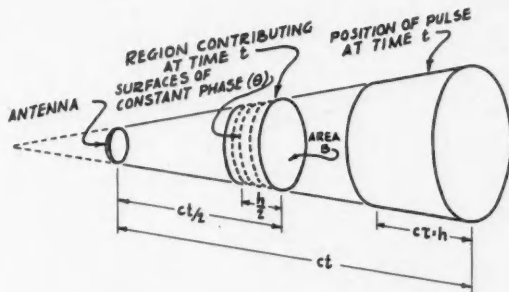
FIG. 1.   Positions of pulse and contributing region at time t.

Consider that fraction of the active volume giving signals of phase between θ and $\theta + \Delta\theta$. It consists of a series of cross-sectional slices of the beam, having a total volume of $\dfrac{\Delta\theta}{2\pi}\dfrac{Bh}{2}$, which we will denote by V_θ. Let us treat it as a region all-in-phase.

In the case of randomly distributed particles, the number in volume V at a given instant is $V\bar{n} + G(V\bar{n})$, where $\bar{n}$ is the average number in unit volume and $G(V\bar{n})$ is a Gaussian deviate whose mean square value is $V\bar{n}$. The probability distribution of G is then

[1]
$$P(G) = \frac{1}{(2\sigma^2\pi)^{1/2}}\, e^{-G^2/2\sigma^2}, \quad \sigma^2 = V\bar{n},$$

$P(G)\, dG$ being the probability that G falls into the range of values G to $G + dG$.

Since the particles in this volume are scatterers all in the same phase and each giving amplitude a, the total amplitude is $V\bar{n}a + G(V\bar{n}a^2)$. If various sizes of scatterers are involved, this becomes

$$V\bar{n}_1a_1 + V\bar{n}_2a_2\ldots + G(V\bar{n}_1a_1^2 + V\bar{n}_2a_2^2 + \ldots).$$

In either case, let A_θ denote the amplitude of the signal from the region under consideration; then

$$A_\theta = V_\theta\textstyle\sum a + G(V_\theta\textstyle\sum a^2),$$

where the summations are over unit volume, G as before is a Gaussian deviate whose mean square value is $\sigma^2 = V_\theta\sum a^2$, and $V_\theta = \dfrac{\Delta\theta}{2\pi}\dfrac{Bh}{2}$.

For use in summation over the various phases rectangular coordinates may be taken. The X-component of A_θ is

$$X_\theta = [V_\theta \sum a + G(V_\theta \sum a^2) \cos \theta].$$

The X-component of the sum of all amplitude elements, and so of the resultant phasor, is

$$X = \sum_\theta V_\theta(\sum a) \cos \theta + G[\sum_\theta V_\theta(\sum a^2) \cos^2 \theta] = 0 + G(\tfrac{1}{4}Bh\sum a^2),$$

obtained on the assumption that $\sum a$ is independent of θ, i.e. that the mean density of the scatterers is the same throughout the contributing region.

It follows at once that X and Y similarly are Gaussian deviates of mean square values

[2] $$\overline{X^2} = \tfrac{1}{4}Bh \sum a^2 \text{ and } \overline{Y^2} = \tfrac{1}{4}Bh \sum a^2.$$

Since $A^2 = X^2 + Y^2$, therefore

[3] $$\overline{A^2} = \overline{X^2} + \overline{Y^2} = \tfrac{1}{2}Bh \sum a^2.$$

Now A^2 and a^2 are proportional to the total and individual intensities, respectively, and so equation 3 states that the average intensity is the sum of the intensities from the individual scatterers.

The foregoing addition of the random phasors being received at a given instant is Rayleigh's (4) problem of the "random walk". While the answer is well known, it has been developed here using a form of grouping most convenient to later arguments in the present work.

The probability distributions of X and Y are Gaussian:

[4] $$P(X) = \frac{1}{\sqrt{2\sigma^2\pi}} e^{-X^2/2\sigma^2},$$

and similarly for Y, where the mean square deviation σ^2 of X and Y is given by

[5] $$\sigma^2 = \tfrac{1}{4}Bh \sum a^2.$$

The summation is over unit volume; multiplication by $\tfrac{1}{2}Bh$ makes it a summation over the contributing region, i.e. the region heard from at any one instant.

Using equation 3, $2\sigma^2$ may be replaced by $\overline{A^2}$, which henceforth will always be done, since $\overline{A^2}$, the mean square value of the received amplitude and hence a number proportional to the intensity, is a most important and easily visualized quantity. In subsequent work it will be convenient to disregard the factor of proportionality between $\overline{A^2}$ and the mean intensity; so that $\overline{A^2}$ will be the symbol both for mean-square amplitude and mean intensity.

The probability of the vector ending in an element of area $dX\,dY$ at position X, Y in the phasor plane is

[6] $$P(X)\,P(Y)\,dX\,dY = \frac{1}{\pi\overline{A^2}} e^{-(X^2+Y^2)/\overline{A^2}}\,dX\,dY.$$

This is a dome of which all cross sections are Gaussian (Fig. 2). The region about the origin is the area on which the phasor is most likely to terminate, but zero
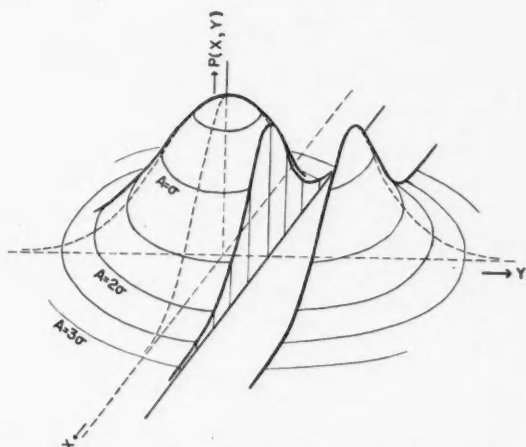
FIG. 2. Perspective sketch of the Gaussian dome $P(X, Y)$ (equation 6), with A, X, and Y measured in units of σ, the r.m.s. value of X and Y.

is not the most likely value for the *amplitude*, which is the distance from the origin regardless of phase.

Probability Distributions of Amplitude, Intensity, and Intensity Level

By rewriting equation 6 in plane-polar coordinates, and integrating over all values of θ, the probability distribution for the amplitude A

[7] $$P(A)\, dA = (2A/\overline{A^2})\, e^{-A^2/\overline{A^2}}\, dA$$

is obtained.

It is the quantity $\overline{A^2}$, the intensity of the received signal, that has been related in equation 3 to the scattering cross section of the particles $\sum a^2$ (and so, for Rayleigh scattering, to $\sum D^6$, where D is particle diameter). Thus the probability distribution of A^2, the instantaneous value of the intensity, is of special importance.

Using $P(A^2)\, dA^2 = P(A)\, dA$, one finds

[8] $$P(A^2)\, dA^2 = (1/\overline{A^2})\, e^{-A^2/\overline{A^2}}\, dA^2.$$

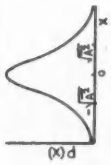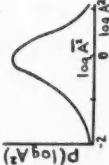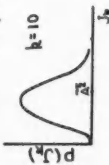This distribution is a simple exponential; its maximum value is at the origin.

The range of values of intensity is often very great. For this reason, displays, measurements, and analyses in terms of intensity level (in db. $= 10 \log_{10} A^2/A_0^2$) are often preferred. In such an event, the distribution in the logarithm

[9] $$P(\log A^2)\, d\log A^2 = \frac{1}{M\overline{A^2}} \exp\left\{ \frac{\log A^2}{M} - \frac{1}{\overline{A^2}} e^{(\log A^2)/M} \right\} d\log A^2,$$

where $1/M = \ln 10 = 2.30258$, is required.

Some properties of the above distribution functions are listed in Table I. Sketches of equations 4, 8, 7, and 9 appear on the left of the table.

TABLE I

Signal function j		Probability function $P(j)$	Most probable value j_b	Mean value $\bar{j}$	Standard deviation $\sqrt{(j-\bar{j})^2} = \sigma_j$
X (or Y)		$\dfrac{e^{-X^2/A^2}}{\sqrt{\pi A^2}}$	0	0	$\sqrt{A^2/2} = 0.707\sqrt{A^2}$
A^2		$\dfrac{e^{-A^2/\overline{A^2}}}{\overline{A^2}}$	0	$\overline{A^2}$	$\overline{A^2}$
A		$\dfrac{2A\,e^{-A^2/\overline{A^2}}}{\overline{A^2}}$	$\sqrt{\overline{A^2}/2} = 0.707\sqrt{\overline{A^2}}$	$\tfrac{1}{2}\sqrt{\pi \overline{A^2}} = 0.886\sqrt{\overline{A^2}}$	$\tfrac{1}{2}\sqrt{(4-\pi)\overline{A^2}} = 0.463\sqrt{\overline{A^2}}$
$\log A^2$		$\dfrac{\exp\left\{\dfrac{\log A^2}{M} - \dfrac{\exp(\log A^2/M)}{\overline{A^2}}\right\}}{M\,\overline{A^2}}$ $(M = \log_{10} e)$	$\log \overline{A^2}$	$\log (\overline{A^2}\,e^{-\gamma})$ $= \log(0.561\,\overline{A^2})$	$\pi(\log e)/\sqrt{6} = 0.557$
J_k		$P(J_k) = \dfrac{k^k J_k^{k-1}\exp(-k J_k/\overline{A^2})}{(\overline{A^2})^k (k-1)!}$	$\overline{A^2}\left(1-\dfrac{1}{k}\right)$	$\overline{A^2}$	$\dfrac{\overline{A^2}}{\sqrt{k}}$
$\overline{A^2}$		$Q_k(\overline{A^2}) = \dfrac{(k J_k)^{k-1}\exp(-k J_k/\overline{A^2})}{(\overline{A^2})^k (k-2)!}$	J_k	$\dfrac{k}{k-2}J_k$	$\dfrac{k}{(k-2)\sqrt{k-3}}J_k$

3. PROBABILITY DISTRIBUTIONS FOR SEVERAL INDEPENDENT DATA

The widths of the above distribution functions suggest that little significance can be attached to single echo measurements. Several data are required for the reduction of the fluctuations. Only when the fluctuations are small can $\overline{A^2}$, the mean value of the signal intensity, be determined from the measurements with any degree of confidence.

Averaging A^2

It is required to determine $P(J_k)$, the distribution of J_k, the average of k independent intensity values. Thus

[10]
$$J_k = \frac{1}{k} \sum_1^k A^2.$$

The required distribution is the product

[11]
$$P(A_1^2)\, P(A_2^2) \ldots P(A_k^2)\, dA_1^2\, dA_2^2 \ldots dA_k^2$$

summed over all values of the A^2's which satisfy condition [10]. Thus

[12]
$$P(J_k)\, dJ_k = \frac{e^{-kJ_k/\overline{A^2}}}{(\overline{A^2})^k} \int \int \ldots \int dA_1^2\, dA_2^2 \ldots dA_k^2,$$

$(k - 1 \text{ integration signs}).$

where the integration is carried out subject to $\sum A_i^2 = kJ_k$.

The problem can be solved in an elementary way[1] by the method of induction. The integrations can be carried out for $k = 2$ and $k = 3$ by changing [12] into polar coordinates, and from $P(J_2)$ and $P(J_3)$ results for other low values of k can be obtained. An inspection of a few such expressions allows the form for any value of k to be inferred to be

[13]
$$P(J_k)\, dJ_k = \frac{k^k}{(\overline{A^2})^k (k - 1)!} J_k^{k-1} e^{-kJ_k/\overline{A^2}}\, dJ_k.$$

This general result is the correct one, because (i) it reduces to the proper forms for $k = 2$ and 3 respectively, and (ii) it can easily be shown that an increase of k by 1 leads to the corresponding expression for J_{k+1}.

Graphs of the distribution $P(J_k)$ for $k = 1, 2, 10,$ and 100 are shown in Fig. 3. It will be noted that the distributions become increasingly more peaked (at $\overline{A^2}(1 - 1/k)$) and narrower (standard deviation = $\overline{A^2}/\sqrt{k}$) as k increases. This is brought out more usefully by the curves of Fig. 5. Here, using Pearson's Tables of the Incomplete Γ-Function, the limits below which 2.5, 10, 25, 75, 90, and 97.5% of the averages of k independent measurements of A^2 may be expected to fall have been plotted. The vertical separations of corresponding members of this family are the 95%, 80%, and 50% confidence limits. It will be seen, for instance, that 10% of the averages of 50 independent measurements fall below $0.80\overline{A^2}$, while 90% come below $1.175\overline{A^2}$. It follows then that the 80%

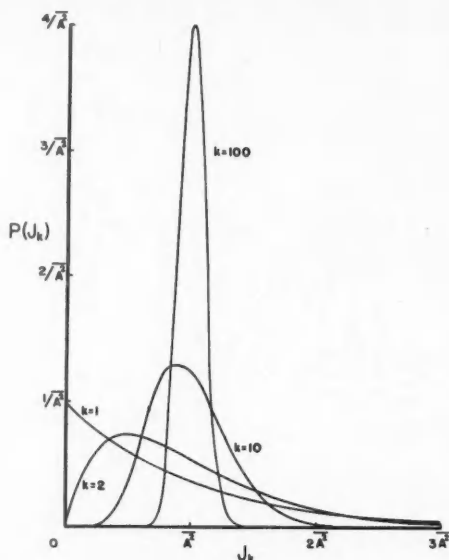[1] *For a more general method of formulating the problem, see Wallace (5).*

FIG. 3.   The probability distribution of J_k, the average of k independent values of signal intensity, when the true mean intensity is $\overline{A^2}$ (see equation 13).

confidence limits are approximately $\overline{A^2} \pm 0.2\overline{A^2}$. When the confidence limits are plotted against $k^{-(1/2)}$, they appear as almost straight lines converging towards a point at $k^{-(1/2)} = 0$.

The above solution may be formulated usefully in an inverse manner (as suggested by Wallace (5)) by inquiring into the precision to which $\overline{A^2}$ may be determined when an observed value of J_k is available. The relative probability that the true average has a value $\overline{A^2}$, given a value of J_k, is simply (from equation 13) $(\overline{A^2})^{-k}e^{-kJ_k/\overline{A^2}}$; the distribution in $\overline{A^2}$ follows by normalization:

$$[14a] \qquad Q_k(\overline{A^2})\, d\overline{A^2} = \frac{e^{-kJ_k/\overline{A^2}}\,(\overline{A^2})^k}{\displaystyle\int_0^\infty e^{-kJ_k/\overline{A^2}}d\overline{A^2}/(\overline{A^2})^k}\, d\overline{A^2}.$$

The normalizing integral in the denominator is finite only if $k > 2$; that is to say, from a single intensity measurement no information about A^2 may be obtained; or, to put it more precisely, for a given measurement of J_k there is always an overwhelming probability that it came from a very large $\overline{A^2}$. The fact that we do not really admit this overwhelming probability is based on considerations quite extraneous to the measurement made, e.g. a general knowledge of the nature of the disturbance from which the echo comes.

If $k > 2$, equation [14a] becomes

$$[14b] \qquad Q_k(\overline{A^2})\, d\overline{A^2} = \frac{(kJ_k)^{k-1}}{(k-2)!} \frac{1}{(A^2)^k}\, e^{-kJ_k/\overline{A^2}}\, d\overline{A^2}.$$

This distribution is plotted for $k = 2, 3, 10$, and 100 in Fig. 4 which should be compared with Fig. 3. The new curves are in general broader, though as k increases, the two distributions become more and more alike. A notable difference is that the most probable value of $\overline{A^2}$ equals J_k for all values of k. Also, the
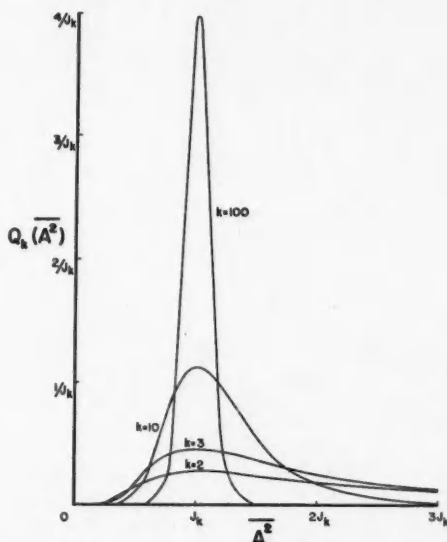

Fig. 4. The probability distribution of $\overline{A^2}$, the mean signal intensity, in terms of J_k, an average of k independent values of signal intensity (equation 14b).
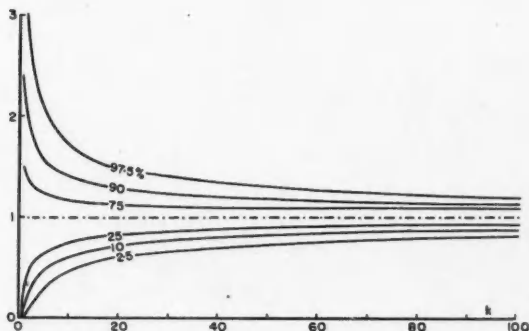

Fig. 5. Width of the distribution $P(J_k)$, expressed in units of $\overline{A^2}$ (along the ordinate axis). The 90% curve, for instance, indicates that 90% of the averages of 50 independent values of signal intensity (A^2) may be expected to fall below $1.175\overline{A^2}$.
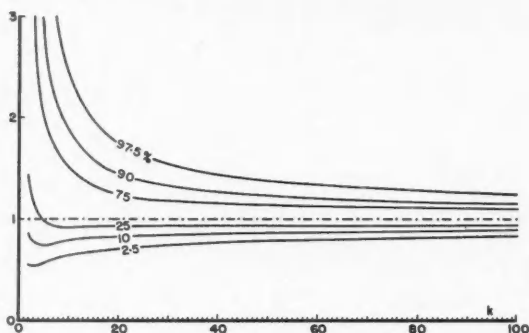
FIG. 6. Width of the distribution $Q_k(\overline{A^2})$, expressed in units of J_k (along the ordinate axis). The 90% curve indicates, for instance, that there is a 90% chance that $\overline{A^2}$ (the mean of very many measurements) falls below $1.225\,J_{50}$, J_{50} being an average of 50 independent intensity values.

nth moment of the $Q_k(\overline{A^2})$ distribution exists only for $k \geqslant (n+2)$. Limits of confidence for $Q_k(\overline{A^2})$, similar to those for $P(J_k)$, are shown in Fig. 6. Some properties of both distributions are listed in Table I.

Averaging A and log A²

The probability distributions of averages of k independent values of signal amplitude A and intensity level $\log A^2$ cannot be found by the above methods. A numerical method was therefore adopted. One thousand random numbers for X and another thousand for Y (all taken from Wold (6)) were combined to form sets of one thousand independent values of A and of $\log A^2$, obeying, respectively, the distributions $P(A)$ and $P(\log A^2)$. Confidence limits, describing the convergence of the averages of k independent values of A and of $\log A^2$, were then drawn, as functions of k, in a manner similar to Figs. 4 and 6. These limits, when expressed in comparable terms, were found to be very close to those for $P(J_k)$; for large values of k, they can in fact be shown to be identical.

Probability of a Signal Being Above a Given Threshold

While averaging is the most obvious and theoretically the most satisfactory way of dealing with several independent data, the practical problems involved are considerable. Extensive and costly equipment of at best doubtful performance is required in the storing and averaging, if a reasonably large number of data are required. An alternative method— the classification of the signals and the determination of the fraction falling above a given threshold—can be realized by much simpler and more reliable equipment, as only on–off type of response is required in the circuits. The theory of this method of analyzing the data will now be presented, and the resulting reduction of the fluctuations will be compared with that obtained by straight averaging.

The probability that A^2 has a value equal to or greater than C^2 (a given threshold) is (using equation [9])

[15] $$\int_{C^2}^{\infty} \frac{e^{-A^2/\overline{A^2}}}{\overline{A^2}}\, dA^2 = e^{-C^2/\overline{A^2}}.$$

(The probability for $A \geqslant C$ and for $\log A^2 \geqslant \log C^2$ is, of course, the same.)

If k independent values of A^2 are examined, let p be the number of them falling above the threshold C^2. This number p has an a priori probability $\bar{p} = ke^{-C^2/\overline{A^2}}$ and follows the binomial distribution:

$$[16] \qquad P_k(p) = \frac{k!}{(p)! \, (k-p)!} \left(\frac{\bar{p}}{k}\right)^p \left(1 - \frac{\bar{p}}{k}\right)^{k-p}$$

$$[17] \quad \begin{cases} \text{of mean value } \bar{p} \\ \text{and mean square deviation } \bar{p}(1 - \bar{p}/k). \end{cases}$$

Let the calculated value of $\overline{A^2}$, obtained from the observed value of p/k, be denoted by $\widetilde{A^2}$. Examine now the fluctuations in $\widetilde{A^2}$ about the a priori mean intensity $\overline{A^2}$. Equation [15] leads to

$$[18] \qquad \overline{A^2} = \frac{C^2}{\ln (k/\bar{p})} \quad \text{and} \quad \widetilde{A^2} = \frac{C^2}{\ln (k/p)},$$

where, for brevity, one may put $x = p/k$ and $y = \widetilde{A^2}/C^2$.

Using the binomial distribution [16], one can compute the limits x_F in x, within which given fractions F of measurements of x may be expected to fall. From equation [18] one can then obtain the corresponding limits y_F in y, which may conveniently be expressed as multiples of $\bar{y} = \overline{A^2}/C^2$. The results can thus be displayed (Fig. 7) as plots of $y_F/\bar{y}$, as functions of $\bar{p}/k$ or C^2/A^2. The necessary computations were carried out for all integral values of p when $k = 10$. In the cases $k = 50$ and $k = 100$, on account of the unwieldy form of the binomial law, a Gaussian approximation for $P(p)$ was used.

From Fig. 7, the smoothing is seen to depend on the proper choice of C^2, which in turn varies somewhat with k and with the degree of confidence required: when k is large (50 or 100), C^2 should be between $1.2 \overline{A^2}$ and $1.6 \overline{A^2}$, corresponding to $\bar{p}/k$ between 0.2 and 0.3. For smaller values of k, lower thresholds are indicated. At $k = 10$, C^2 should be about equal to $\overline{A^2}$, giving $\bar{p}/k$ of about 0.35. The confidence limits of Fig. 7 are fairly flat in the vicinity of the optimum points; at $k = 50$ or 100, for instance, the variation in precision over an 8 db. range in C^2 containing the optimum value is barely 20%. It is worth observing that this particular optimum range of C^2 arises as a compromise from the contradictory indications of equations [18] (sketched in Fig. 8) and [17]. Equation [18] permits the evaluation of $\overline{A^2}/C^2$ from $\bar{p}/k$ with the greatest precision where the slope of the curve has its flat minimum (at $C^2 = 2\overline{A^2}$ or $\bar{p} = 0.135k$). The precision is extremely poor, on the other hand, near $\bar{p} = 0$ and particularly near $\bar{p} = k$, which are precisely the regions where, according to equation 17, minimum scatter in $\bar{p}$ may be expected.

In Fig. 9, the best smoothing obtainable by the present technique is compared with the reduction of the fluctuations when k intensity measurements are averaged in the usual way. It may be seen that at $k = 10$ the 95% confidence limits are 70% wider with the present technique than when the data are averaged in the ordinary way. At $k = 100$, the widening of these limits is less than about 30%, which is probably a loss in precision smaller than would be incurred on account of experimental error if ordinary averaging were attempted.
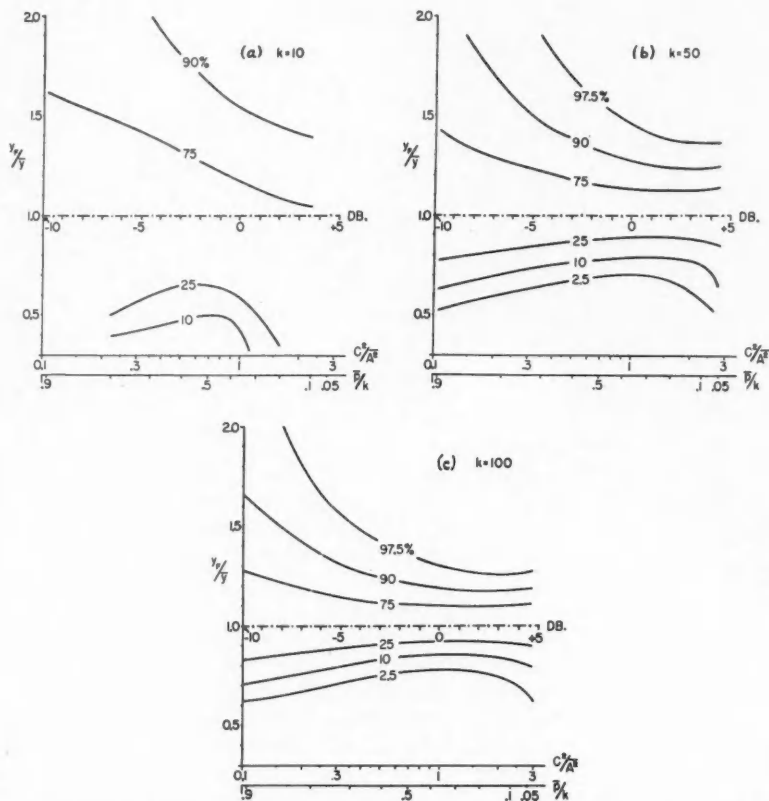
FIG. 7. Confidence limits for $k = 10$, $k = 50$, and $k = 100$. It may be seen, for instance, that when $k = 100$, one can place $\overline{A^2}$ with 80% confidence within the limits $0.85\overline{A^2}$ and $1.17\overline{A^2}$ when $C^2 = 1.5\overline{A^2}$, i.e. when $\overline{p}/k$ is about 0.22.

An attempt to check the validity of the theory here presented by numerical means was made. Values of p/k for $k = 100$ were calculated from the set of 1000 independent values of A assembled for use in the previous subsection. These values were plotted in Fig. 10 against the theoretical limits of Fig. 7c. If allowance is made for the smallness of the sample studied, the numbers may be seen to support the theory.
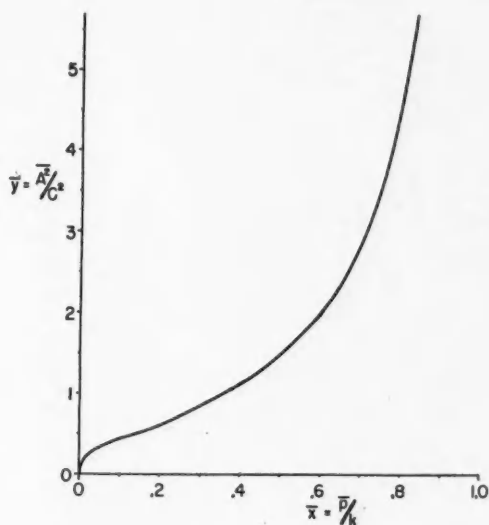
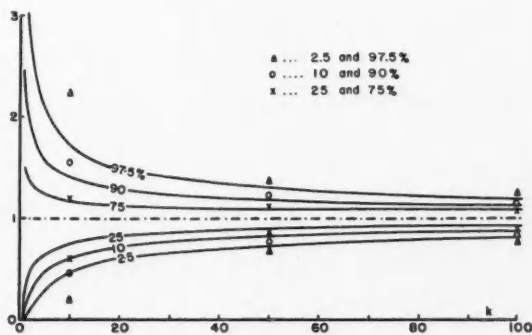FIG. 8.   Plot of equations [18], $y = \dfrac{1}{-\ln x}$ or $\bar{y} = \dfrac{1}{-\ln \bar{x}}$.

FIG. 9.   Comparison of confidence limits in classifying and counting technique (heavy points) and in averaging (curves, copied from Fig. 5). Note, for instance, that when $k = 50$, the theoretical 80% confidence band in averaging is $0.35\overline{A^2}$, and in classifying and counting $0.45\overline{A^2}$.
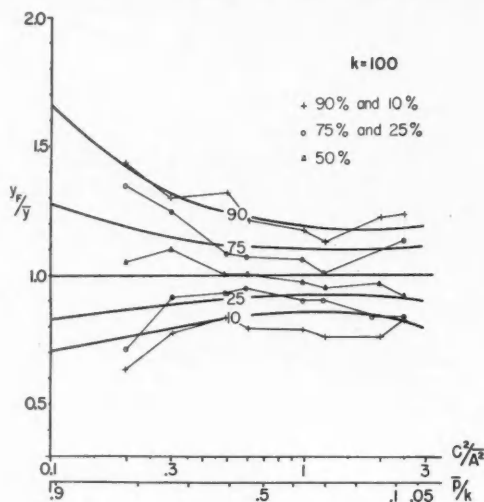
FIG. 10.   Numerical check of the confidence limits of Fig. 7c.

4. DEPENDENT AND INDEPENDENT DATA

So far this paper has been concerned with independent data. It is now desirable to discuss just exactly what data are independent, how their number may be increased, and whether any information can be derived from nonindependent ones.

Achieving Independence in Time

Consider first the scatterers in a particular "contributing region" (cf. Fig. 1). The specific value of the phasor **A** depends on the distribution of the particles relative to the phase pattern of the beam. If another pulse is sent out after some motion of the scatterers has taken place, a change in **A** in both magnitude and phase is to be expected, unless the motions involve exact half wave lengths only (i.e. zero phase change), or are small compared to the half wave length. On the other hand, this new value of **A** will never, in principle, be completely independent of the first, because however much time elapses, the configuration of the particles at any time will always depend to some extent on the initial distribution. Independence is, however, approached gradually. If the scatterers are raindrops, experiment indicates that practically complete independence is achieved at 10 cm. wave length after time intervals of the order of 0.01 to 0.02 sec. (announced by Aaron Fleisher at the Radar Weather Conference, University of Illinois, October 1–3, 1951). This means that in one second, between 50 and 100 independent data may be obtained from one particular contributing region. Looking vertically at cloud or rain by means of a 1.25 cm. radar, on the other hand, Bartnoff, Paulsen, and Atlas (1) measured times-to-independence of the order of 0.00375 sec.

The variation of the returned intensity in time intervals shorter than those mentioned is related to radio frequency and beam width, and to the frequency and amplitude of the relative motion of the scattering particles. This aspect has been studied by Hilst, Fleisher, and others, and is reported in a series of Technical Reports by the Weather Radar Research group of the Massachusetts Institute of Technology.

Achieving Independence in Range

As the pulse travels out from the radar, the signal returned fluctuates as new scatterers continually come into the contributing region while others leave it. These fluctuations may be studied conveniently by considering the contributing region to be divided into n elements of length $\frac{1}{2}h \times 1/n$, each containing an integral number of wave lengths. The signal phasor contributed from each element has rectangular components which are Gaussian deviates of mean square value $(Bh/4n)\sum a^2$.

As the contributing region proceeds along the beam with speed half that of light, new units are included continually, and old ones dropped out. Sample behavior of **A** as the contributing region progresses outward has been computed from tables of randomly sequenced deviates (Wold (6)) by building up the components X and Y as the algebraic sums of 100 (for n) deviates. The addition
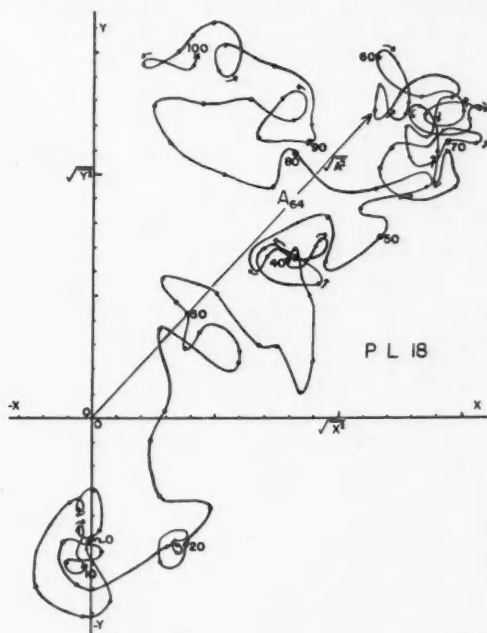

FIG. 11.   Typical hodograph (of half-pulse length PL 18), with contributing region divided into 100 slices. A_{64} is a typical instantaneous amplitude vector.

of one deviate to X and one to Y, and the removal of the 100th-preceding deviates, gives new values for X and Y, and so for A, representing the condition existing when the contributing region has moved by $(1/100)$th its own length. After 100 such changes, one has a whole new set of deviates, an independent value for A.

An actual case, developed on a 100-element basis, is shown in Fig. 11. Each phasor element (the straight line joining successive points on the hodograph) is independent of all others except the hundredth-preceding and the hundredth-succeeding, with each of which it shares one of its two vector terms. Thus while the first and last points on the hodograph for length $h/2$ are the only two independent points (i.e. phasors starting from the origin) on the hodograph, every single element (line joining adjacent points) is independent of every one of the other 99 elements appearing in this hodograph. When a continuous hodograph for several successive lengths $h/2$ is prepared, the elements become half-independent, each one being related to the hundredth-preceding and succeeding elements.

It is rather surprising to find that the probability distribution of each of the phasor elements is the same as that for the vector sum of 100 of them. When we add them vectorially, the intensity (corresponding to A^2) increases proportionately, on an average, to their number, but (if, as for the moment, background noise is neglected) the accuracy of the information conveyed remains constant. If the individual terms could be squared and their squares added, the accuracy would increase from that for $k = 1$ to that for $k = 100$.

The variation of amplitude and phase with range has been plotted (Fig. 12) for 30 half-pulse lengths. The plot of A is effectively the picture resulting on an A-scope type display, if the band-width of the amplifiers is approximately $100c/h$ and all circuit elements respond linearly. The variation of A^2 with range is shown in Fig. 13. The prc⋅ ⋅ility distribution in this case reaches a maximum at $A^2 = 0$ (equation 8) ⋅ı so of course the trace spends most of its time close to the axis $A^2 = 0$.

A characteristic of the graphs of Fig. 12 worth special mention is that the fluctuations in θ become small when A is large. The explanation is that the fluctuations in the increment ΔA from one amplitude to the next are relatively small, as is illustrated by the general appearance of the hodograph of Fig. 11. When A is large, the effect of the vector increment on the phase angle is therefore small, and vice versa. It may be noted in passing that if the average value of A over a length, say $h/2$, were corrected according to the amount of fluctuation in θ, a much improved measure of $\bar{A}$ would be obtained.

An assessment was made of the value of the information conveyed by incompletely independent signals, such as make up the curves of Figs. 12 and 13. Mean values of A^2 (or A) obtained by averaging under the full curves were compared with the means of the instantaneous values separated in range by $h/2$, i.e. adjacent independent data. On the whole, the results indicate a slightly more rapid convergence to the true average when the dependent values are included along with the independent ones. This same conclusion is further borne out by observations of the standard deviation. The theoretical value of σ (for infinite samples), for independent values of A^2, is $\overline{A^2}$; for averages of 100 inde-
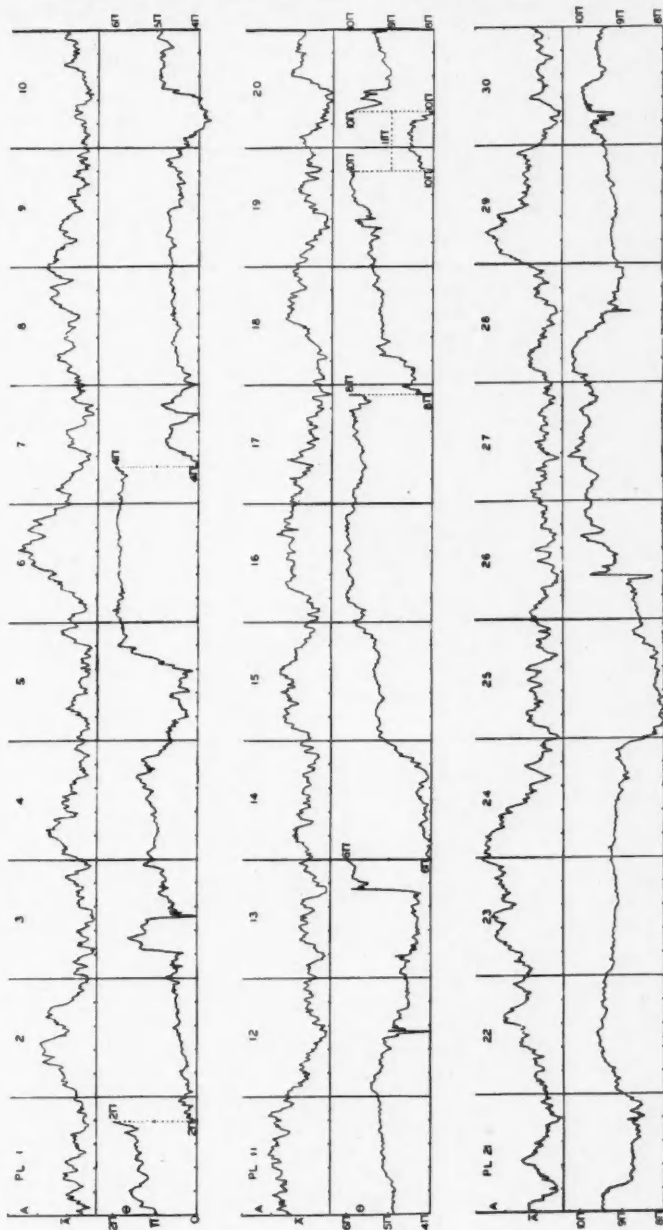
Fig. 12.   Traces of computed signal amplitude A and phase θ for 30 half-pulse lengths, for each of which 100 points are shown. The A-trace is a hypothetical sample of an A-scope sweep, provided the amplifier band width is $100/\tau$ and all circuit elements involved respond linearly.
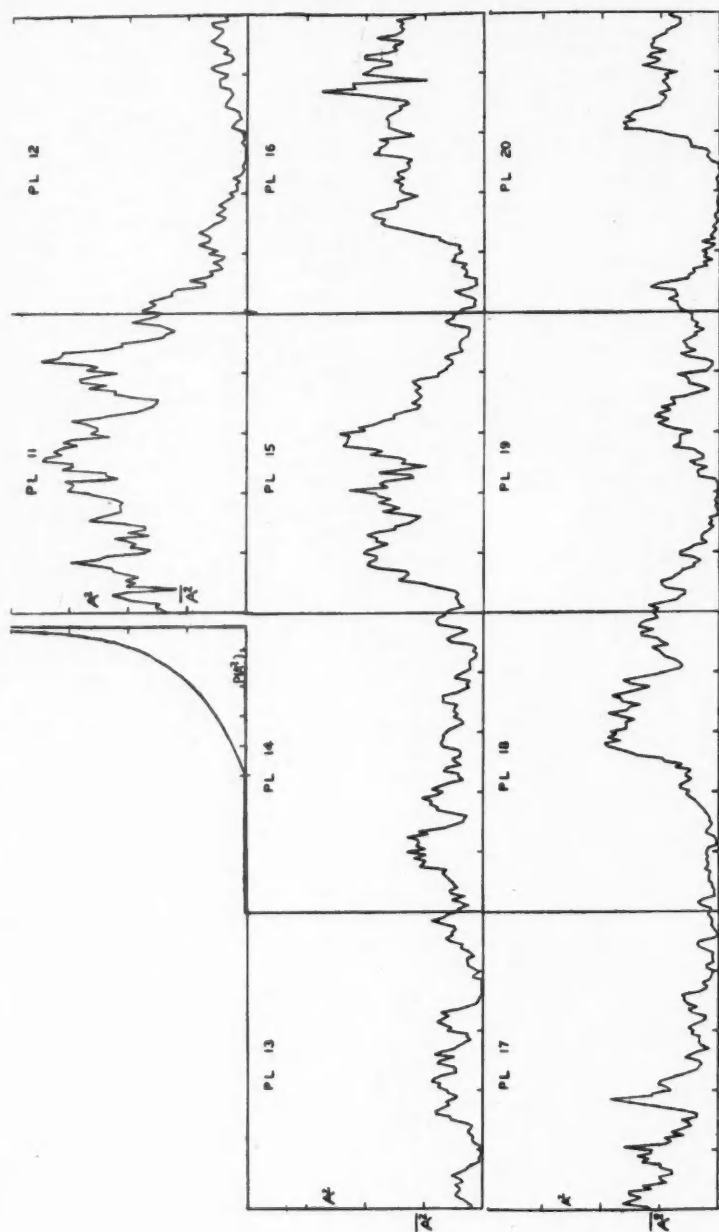
FIG. 13.   Traces of A^2 (the signal intensity) for 10 of the half-pulse lengths of Fig. 12; also the probability distribution of (the independent values of) A^2, shown just ahead of PL 11.

pendent values of A^2 it is $\overline{A^2}/\sqrt{100} = 0.10\overline{A^2}$. For the 30 half-pulse lengths under study the deviations turned out to be $1.008\ \overline{A^2}$ (for the independent values of A^2) and $0.85\ A^2$ (for the 30 averages of 100 values of A^2). This indicates again that an average of 100 such semidependent values is a somewhat better clue to true mean $(\overline{A^2})$ than any independent value alone, but is, of course, not nearly so good as an average of 100 independent values. A more quantitative discussion of this problem is given by Wallace (5), who considers a continuous smooth transition from one independent point to the next (corresponding to our 100 intermediate steps). The gain in accuracy of information again appears to be disappointingly small. The number of independent data available from a length along the beam $k \times \frac{1}{2}h$ is k and the improvement obtainable by averaging a larger number of data is never great.

It has been seen from the hodograph that the signal *variations* in a range interval $h/2$ contain the equivalent in information of many independent data. It has appeared, however, that averaging under the A^2 (or the A) plot is not an efficient way of bringing it out. It is the successive vector variations in $\mathbf{A}$, which we will call $\Delta\mathbf{A}\ [= A(t + \Delta t) - \mathbf{A}(t)]$, that contain the additional information. It may be worth considering briefly the practical problems of obtaining this quantity. Quite a direct method, simple in principle, though probably difficult to realize, might consist in splitting the signal received by the antenna into two parts, to be propagated by two wave guides in parallel. One of the guides is slightly longer than the other, so that one half of the signal will be delayed by some time interval Δt, equivalent to a range interval $\frac{1}{2}c\Delta t$, relative to the other. If the delayed term is subtracted from the other, the resultant is, for a perfectly rectangular pulse, just this $\Delta\mathbf{A}$. The signal is, of course, of low intensity, for the method if used at all would be for $\Delta t \ll \tau$. Further, amplifiers would be required of band-width $1/\Delta t$.

It is probably easier to obtain the component of $\Delta\mathbf{A}$ in the direction of $\mathbf{A}(t)$. This component is inferior to $\Delta\mathbf{A}$ only in having (because it is just a component) an intensity level 3 db. lower. It would be obtained by differentiating the "video" or output signal, and full-wave rectifying the derivative to obtain its absolute magnitude. Again, amplifiers would be required of band-width $1/\Delta t$, but where the $\Delta\mathbf{A}$ device was most practicable for $\Delta t \ll \tau$, the dA/dt device should be practicable for any Δt for which the corresponding band-width $1/\Delta t$ is available. This derivative no longer makes sense, however, when circuits preceding the video become saturated.

Now for any interval Δt between independent data, a band-width of $1/\Delta t$ is sufficient to provide all the independent data. An increase in band-width beyond this value adds extra detail which adds little useful information, hardly increasing the value of k. It does, however, add background noise of intensity proportional to the band-width. The graphs of A and A^2 in Figs. 12 and 13 consist of points plotted at intervals of $\tau/100$, corresponding to signals passed through amplifiers of band-width $100/\tau$. If we observe or average A^2 (or A) directly, all detail beyond one point per time interval τ is of little use. Similarly, in the case of a receiver, any band-width beyond $1/\tau$ is of little use. If, however, we observe $\Delta\mathbf{A}$ or its component, or the square of either of these, then added

band-width up to $1/\Delta t$ can be utilized to increase k, our measure of useful
information, efficiently. The increment Δt is here the time interval over which
ΔA is measured.

In general, suppose that signals from precipitation are required with resolu-
tion in range to a range interval l. The accuracy of the information can be
increased by making the half-pulse length $h/2$ short compared with l, and aver-
aging along the range over a travelling interval l. Alternatively, the pulse length
can be left unchanged, but the *increments* in the signal magnitude rather than
the total signal are averaged. In either case, the signal component used is
weakened by this shortening, and the receiver band-width required is increased.
One advantage of the short time-constant at the output, not shared by a
shortened pulse length, is that the former could presumably be made variable
with range. Thus the sensitivity of the equipment could be made independent
of range, and the excess power at short range disposed of to provide increased
precision at short range.

Achieving Independence by Changing the Frequency

The above discussion of the fluctuations in time in the return from a given
contributing region demonstrates that considerable time must be allowed to
elapse before an independent datum can be obtained. The discussion of the
fluctuation encountered as the pulse is moving out from the radar shows that an
appreciable loss in power and a gain in background noise level must be coun-
tenanced if the number of independent signals along a given bearing is to be
increased. The number of independent signals from a given contributing region
can however be multiplied by shifting the frequency of successive pulses, without
any sacrifice in the signal/noise ratio, and regardless of the time interval between
the pulses.

In Section 2 it was noted that any particular range of phase θ to $\theta+\Delta\theta$
could be identified with a series of cross-sectional slices of the beam, the volume
of which was denoted by V_θ. In the case of a one microsecond pulse of 3 cm.
radiation, for example, the series contains 10,000 slices. The deviation from
average of the magnitude of the phasor element representing that range of phase
will be proportional to the deviation from average of the scatterers in that series
of slices. If the wave length of the radiation is changed slightly, so that the
number of wave lengths in the pulse length is changed by one, then the volume
V_θ is no longer identifiable with a single phase, but instead is distributed over all
possible phases (Fig. 14). The specific contribution that is made to the resultant
signal is thus eliminated, even though its chance of contributing, on the average,
remains unchanged. This applies to each element of volume V_θ, and to the corre-
sponding phasor element A_θ. It appears, therefore, that a change of *one* in the
number of wave lengths in the pulse length should give an independent value of
A.

If the spreading-out of V_θ over 2π (or any integer $\times 2\pi$) makes the new signal
value *completely* independent of the old, it would seem reasonable that a
spreading-out of V_θ over any angle should create *some* degree of independence.
Wallace (5) gives a complete mathematical analysis of this problem, confirming

SLICES ORIGINALLY AT ZERO PHASE

SLICES FINALLY AT ZERO PHASE

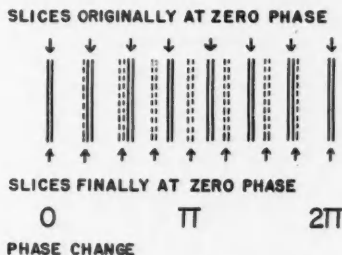0   π   2π

PHASE CHANGE

FIG. 14.   Showing how the phase corresponding to each slice contributing to A (for $\theta = 0°$) is increased as the number of wave lengths in the pulse length (and so the number of slices) is increased by one. For the purpose of the sketch, only eight original slices have been taken to make up the volume V_θ.

the above conclusions. He shows in addition that effectively independent returns can be obtained by frequency shifting, not only for rectangular, but even for somewhat distorted pulses.

For the purpose of illustrating this effect further, it is sufficient to quote one of Wallace's results (also obtained by Goldstein (3)*) valid for a rectangular pulse. The correlation coefficient between the signal intensity $A_0{}^2$ received from a set of scatterers at frequency ν_0 and the intensity A^2 obtained from the same scatterers at frequency $\nu_0 + \Delta\nu$ is given by:

[19]
$$\rho = \left(\frac{\sin \pi\tau\Delta\nu}{\pi\tau\Delta\nu}\right)^2,$$

where the correlation coefficient is defined by

[20]
$$\rho = \frac{\overline{A_0{}^2 A^2} - (\overline{A^2})^2}{\overline{A^4} - (\overline{A^2})^2}.$$

Equation [19] is sketched in Fig. 3 of Wallace (5). The correlation between A^2 and $A_0{}^2$ falls off rapidly as the frequency shift approaches $1/\tau$, the reciprocal pulse duration. When $\Delta\nu$ is greater than about $3/4\tau$, A^2 may be regarded as virtually independent of $A_0{}^2$.

Achieving Independent Data by Change of Aspect

Two (or more) independent signals may be obtained simultaneously from the scatterers of a given contributing region, if the scattered energy is received at two (or more) separate antennas. One of the antennas may also do the transmitting, so that the method to be discussed involves one ordinary radar set and at least one additional receiver. Independence comes about in this procedure through the fact that randomly distributed particles present randomly different aspects to properly spaced receiving antennas. In Fig. 15, AB represents a thin slice of the contributing region from which signals are returned to the radar, all at the same phase. Signals arriving from the point A at the separate receiver will be changed in phase (delayed) by $2\pi(r - r')/\lambda$, while those from B will be

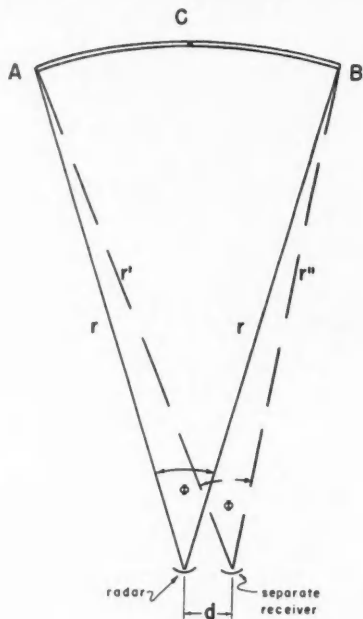*There is a minor misprint in Goldstein's equation (134).*

FIG. 15. Two separate antennas receive practically independent signals from the same scatterers in the slice AB.

changed in phase (advanced) by $2\pi(r - r'')/\lambda$. The phase changes at intermediate points will be between these limits. At a point C, practically halfway, the phase change will be zero. By suitably choosing d, the distance between the antennas, it is possible to make the phase changes at A and B equal, respectively, to $-\pi$ and $+\pi$, or integral multiples thereof. In such an event, the phases of the signals received at the two antennas from each scatterer will differ by effective amounts between $-\pi$ and $+\pi$, the exact value of the difference depending on the *random* position of the particle. The difference itself will therefore be random, and the two signals will be independent. Using the fact that λ and d are very small relative to the range r, and on the assumption of a uniform and sharply defined beam, it is easy to show that for complete independence

$$[21] \qquad\qquad d = n\lambda/\phi, \ n = 1, 2 \ldots$$

where ϕ is the beam width. In fact, the boundaries of the beam are not sharp, and a more precise theory would be required.

The above argument follows so closely that given under the heading of frequency shifting, that it is reasonable to infer a formula similar to [19]:

$$[22] \qquad\qquad \rho = \left(\frac{\sin \ \pi \phi d/\lambda}{\pi \phi d/\lambda} \right)^2$$

for the correlation coefficient between the two signals. When the beam width is defined as the angular distance between half-power points, ϕ is of the order of

λ/D, where D is the diameter of the antenna. The appropriately refined form of equation [21] would then indicate that the smallest value of d for independence is of the order of D, or that the two antennas should be contiguous. It would follow that while only certain discrete values of d lead to *complete* independence, in practice any separation at all would lead to a useful amount of it.

An argument very similar to the above would show that if the radar itself (i.e. transmitter as well as receiver) were moved sideways, independent signals would be obtained from the same scatterers at intervals equal to about one-half of those calculated by equation [21].

If the beam is not filled with scatterers (as has been assumed above) very much the same theory holds, except that ϕ needs to be redefined as the angle subtended by the target at the radar. Two separate receivers and a measured value of the correlation coefficient may then be used to determine the size of the target. This technique has already been applied in radioastronomy (2).

When the existence of background noise is taken into account, the apparent advantage of the above method of obtaining independent signals is reduced, in analogy to what was found above in connection with the suggestion of using a shorter pulse length. Clearly, several small antennas, each with its own receiver, contribute more independent data than one single large one, but the signal intensity carried by each would be small, with an attendant reduction in signal/noise ratio.

5. RADAR DISPLAYS

The averaging of several independent signals, which has been shown to be an essential step in a quantitative evaluation of the return from precipitation, can be greatly facilitated by a careful consideration of the display used. In displacement presentations, or A-scopes, the amplitude A, or some function of A, is displayed as a vertical displacement against a horizontal range-sweep. In area-displays, the signal function is presented as a brightness modulation of the range-sweep, while successive range-sweeps are spread over the area of the display as the direction of the beam is rotated to scan an "area" in space.

Displacement Modulation: Single Sweep

A single sweep of an A-scope resembles Fig. 12, or would if the frequency-response band-width were about $100/\tau$. The best band-width, however, is the reciprocal of the time between independent data. In Fig. 16, therefore, plots resembling usual A-scope traces more closely are obtained by drawing straight lines through a set of 25 independent points. Such curves have been drawn for A^2, A, and $\log A^2$.

Alongside the A-scope traces in Fig. 16 have been drawn the probability distributions of the signal functions as summarized in Table I, and so of the height of the trace. In every case the height of the trace varies widely, and so the average height or "height of grass" is not the sort of thing that can be determined reasonably by a glance at an A-scope presentation. A quantity one can determine well, however, from a single sweep, if it is photographed, is the fraction of time (over several or many pulse lengths) that the signal spends above any specified threshold value. This fraction has been related to the correct value of $\overline{A^2}$ in Section 3. The fraction can usually be determined most accurately when
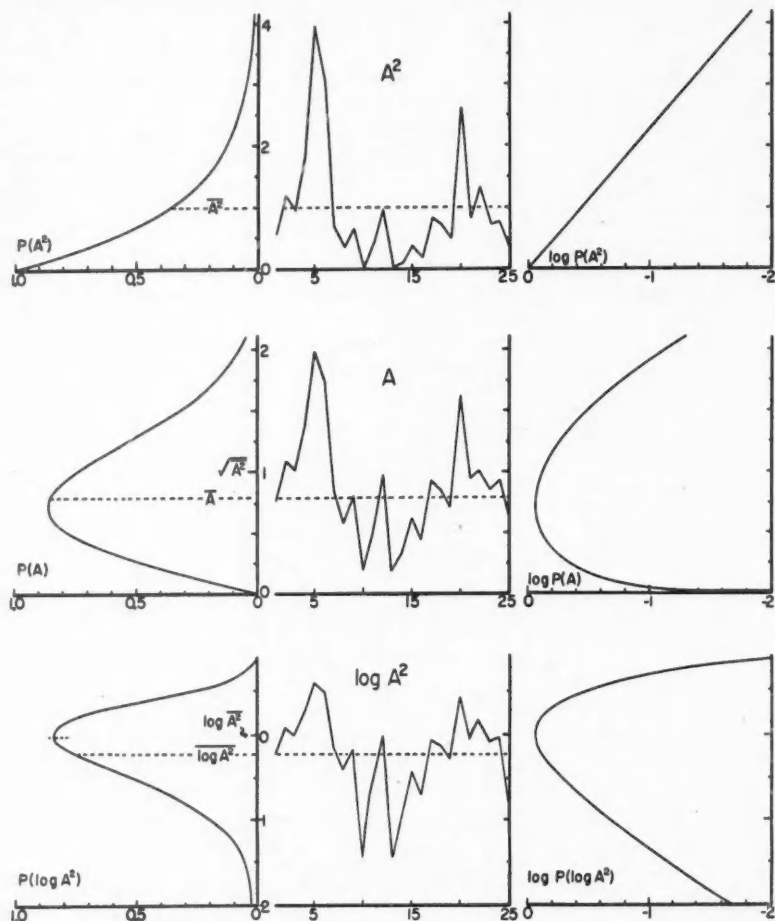
FIG. 16. Top row (left to right): probability distribution of signal intensity (A^2), typical traces of independent A^2-values, and distribution of luminance on "A^2-scope" resulting from superposition of many independent A^2-traces. Center row, same for signal amplitude, A; bottom row for signal intensity level, $\log A^2$.

its value is of the order of 20%. Any display may be used: A or A^2 or $\log A^2$; the height of the optimum threshold will vary most gradually on a logarithmic display. Thus with the wide range of values of $\overline{A^2}$ encountered in precipitation studies, a logarithmic function should be the most useful one to display.

Displacement Modulation: Many Sweeps

The case of several sweeps is more difficult to analyze. When *very many* sweeps are superimposed a new approach suggests itself, however. The superposition

may be by long-persistence phosphor, or preferably, by time-exposure photography, where the contribution of each sweep is given equal weight. Such A-scope photographs are frequently used and reported; their correct interpretation calls for careful consideration.

With many sweeps superimposed, the detail of the individual lines is lost; instead we obtain a continuous gradation of luminance over the display. The degree of contrast in the gradation depends on the characteristics of the persistent phosphor or of the photographic emulsion involved. "Saturation" is possible here, just as it is in electrical circuits, and in most cases it is something to avoid. The probability distributions of the signal function are also distributions of luminance with height, assuming linear response in the phosphorescent or photographic material. Since the processes involved are not usually linear, but approximately logarithmic, the logarithm of the probability is more pertinent to the description of the appearance of the display or its photograph. Plots of the logarithms of the probabilities of the signal functions are also shown in Fig. 16.

The least helpful display, for many sweeps, is that of A^2. Here the log luminance decreases linearly with height. The desired quantity $\overline{A^2}$ could be determined from the slope of the line, but this would involve photometry and a knowledge of the degree of contrast in the photographic or phosphorescent process. The height at which the signal disappears would require a knowledge of the same factors, and of threshold sensitivity as well. The A-display is more useful, in that the height of maximum luminance and so of most-probable A can be determined. A relation between the most probable $A (= A_p)$ and $\overline{A^2}$ has been given in Table I. Photometry is not needed for this determination: the over-all brightness would be reduced until only a narrow region around the maximum was perceptible. Unfortunately, the maximum in the curve of log luminance against height is rather a broad one. The most useful display of the three would be that of log A^2. The maximum here is of the same width regardless of its height on the screen. Further, as mentioned in connection with single sweeps, the motion of the maximum up and down the screen with variations in $\overline{A^2}$ is appropriately more gradual. It is fortuitous and convenient that the most probable value of log A^2 is equal to log $\overline{A^2}$. The rapid decrease in luminance above the height of maximum luminance makes it appear that maximum signal height could be read with considerable accuracy. Consideration of the scales involved reveals that this is not the case. When A^2 drops to zero, its logarithm drops to minus infinity. The finite lower limit of any logarithmic amplifiers distorts the distribution of luminance with height, and for weak signals it must be interpreted with care.

If several independent A's or A^2's or log A^2's are averaged before presentation on a displacement presentation, the resulting distribution in height will be much narrower than those shown in Fig. 14, and a firm, narrow trace across the tube can be obtained. The only drawback is the need for a memory device of some sort before the A-scope.

Intensity Modulation

Figs. 12 and 16 show the variations in displacement with range on an "A-scope", or of intensity (luminance) with range along a single sweep on a two-

dimensional display. Now suppose that the antenna is rotated slowly, so that there are many sweeps on the two-dimensional display for every beam width. Then the variation with angle for a given range r will be similar to the variation with range for a given direction, except that the former changes discontinuously from sweep to sweep. Neglecting motion of the scatterers among themselves, each successive signal at the same range but at a slightly changed direction incorporates some new volume to the contributing region, discards some old, in the same way as an increment in range with a fixed direction (Fig. 17).
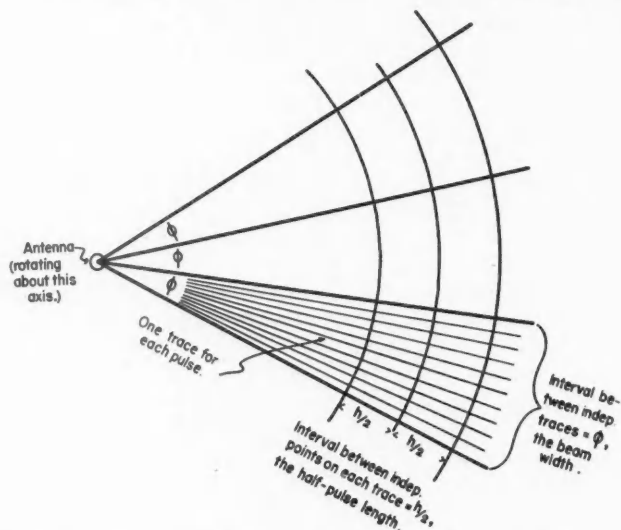

Fig. 17.   Moving along the beam through range interval $h/2$, the half-pulse length, or scanning through ϕ, the beam width, leads to an independent signal value.

To picture the random variations in intensity over the surface of a two-dimensional display, one must visualize the two-dimensional equivalent of Fig. 12. In practice, amplifier band-widths of approximately $1/\tau$ smooth out the variations with range until effectively only the essential independent points are left. On the other hand, the variations of signal with direction of the beam, at fixed range, tend to include many intervening dependent (and so nonessential) points.

Let us consider an example:

Pulse length 1 μsec. ($\frac{1}{2}h = 0.1$ mile),

Beam width $\phi = 1/2°$ ($=1/2$ mile at 56 miles),

PRF $= 1000$ sec.$^{-1}$ $\}= 10$ pulses per beam width,

Rate of sweep $= 50°$ sec.$^{-1}$ $\int = 20$ pulses per mile at 56 miles.

When the degree of independence achieved by relative motion of the scatterers as the beam rotates through its own width (0.01 sec.) is neglected, there will be nine dependent and relatively useless data at range r between successive indepen-

dent data. A sample of the random area pattern of A obtained is given in Fig. 18, for a region 15 half-pulse lengths by two beam widths, or 1.5×1 miles, at range 56 miles for the particular case given above. Streaking across the beam is

6	6	21	7	15	12	3	16	4	12	16	11	15	15	10
7	3	18	9	14	12	10	27	4	16	19	15	14	17	9
10	7	11	3	15	6	16	28	4	12	19	20	14	20	8
11	10	14	10	11	8	11	29	8	7	21	16	5	27	8
10	4	15	11	13	13	14	27	8	5	23	19	2	27	6
6	7	8	12	8	13	14	15	1	12	24	17	10	31	11
8	3	7	11	9	9	14	17	7	13	23	22	10	21	10
7	4	5	4	11	7	2	16	8	5	17	16	12	23	7
6	4	10	4	4	1	10	14	9	4	21	12	7	27	7
5	15	5	10	8	5	10	17	9	11	21	9	11	27	7
8	10	6	9	5	8	14	10	6	6	17	9	10	35	6
13	5	4	10	6	8	11	7	14	10	12	5	13	33	11
15	8	7	16	6	8	6	3	20	14	11	9	8	31	13
23	16	6	8	5	13	4	4	16	12	11	19	2	26	6
22	20	4	12	10	15	5	13	10	14	8	16	0	25	9
18	27	5	10	13	15	9	6	12	13	3	16	5	15	5
13	30	6	11	19	22	10	10	10	10	2	16	14	14	3
19	26	15	12	18	23	4	8	6	19	8	16	14	9	8
12	28	9	8	13	16	9	11	7	17	8	20	12	12	11
5	20	10	10	14	18	9	10	6	13	10	17	15	5	12

(Right margin: BEAM WIDTH; bottom margin marker: $h/2$)

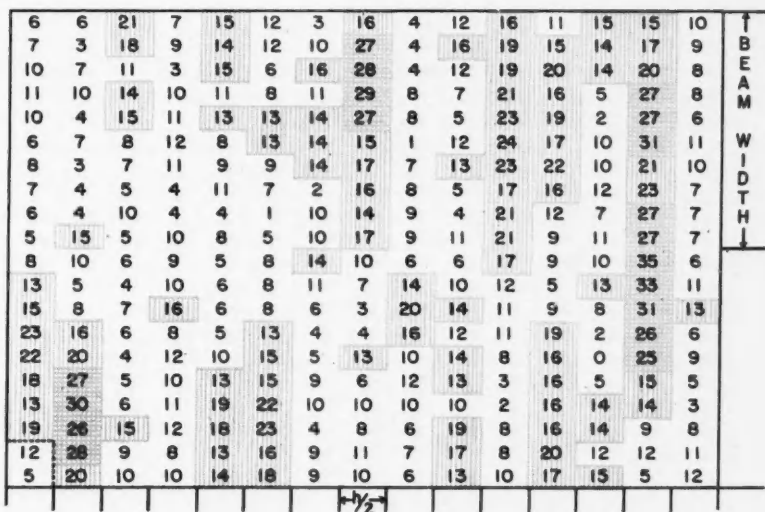FIG. 18. Typical appearance of a section (15 half-pulse lengths $\times$ 2 beam widths) of a brightness-modulated display. (Area shown measures 1.5×1 miles for the example discussed in the text). The numbers represent amplitude values received from element of area resolved ($h/2 \times \phi$). Vertical shading indicates amplitudes exceeding average ($\overline{A} = 12.5$); cross shading, amplitudes exceeding $1.5\overline{A} = 18.75$.

apparent, particularly when high threshold values of the signal are applied. Similar effects would, of course, be obtained in the case of the A^2 and the log A^2 pattern.

If the frequency were varied by one or more megacycles between successive pulses, with a saw-toothed pattern over a cycle of 10 pulses, each successive value in a column would be independent of its neighbors, just as holds now for figures in a row. There would then be 200 independent data per square mile, instead of effectively 20 as there are now. Samples are given (for A) in Fig. 19.

The element of area to which a picture can be resolved is [beam-width $\times \frac{1}{2}h$] but this is scarcely significant when the randomness of the individual recorded data is as great as that displayed in Fig. 19. Without increasing the size of this element, it would be useful to average the data within the element. If the desired elemental area of resolution is greater than beam-width $\times \frac{1}{2}h$, the averaging might usefully be carried to this larger element, which can have any desired shape provided that neither of its dimensions is less than that of the basic element. The creation of the larger element could be achieved fairly simply by deforming the focus of the cathode ray tube or alternatively by defocusing the
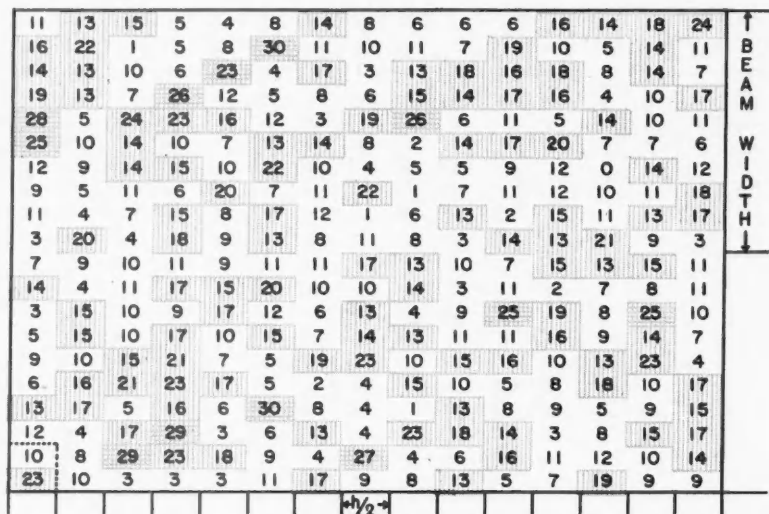
11	13	15	5	4	8	14	8	6	6	6	16	14	18	24
16	22	1	5	8	30	11	10	11	7	19	10	5	14	11
14	13	10	6	23	4	17	3	13	18	16	18	8	14	7
19	13	7	26	12	5	8	6	15	14	17	16	4	10	17
28	5	24	23	16	12	3	19	26	6	11	5	14	10	11
25	10	14	10	7	13	14	8	2	14	17	20	7	7	6
12	9	14	15	10	22	10	4	5	5	9	12	0	14	12
9	5	11	6	20	7	11	22	1	7	11	12	10	11	18
11	4	7	15	8	17	12	1	6	13	2	15	11	13	17
3	20	4	18	9	13	8	11	8	3	14	13	21	9	3
7	9	10	11	9	11	11	17	13	10	7	15	13	15	11
14	4	11	17	15	20	10	10	14	3	11	2	7	8	11
3	15	10	9	17	12	6	13	4	9	25	19	8	25	10
5	15	10	17	10	15	7	14	13	11	11	16	9	14	7
9	10	15	21	7	5	19	23	10	15	16	10	13	23	4
6	16	21	23	17	5	2	4	15	10	5	8	18	10	17
13	17	5	16	6	30	8	4	1	13	8	9	5	9	15
12	4	17	29	3	6	13	4	23	18	14	3	8	15	17
10	8	29	23	18	9	4	27	4	6	16	11	12	10	14
23	10	3	3	3	11	17	9	8	13	5	7	19	9	9

(Right margin: ↑ BEAM WIDTH ↓)   (Bottom: |←½→|)

FIG. 19. Same as Fig. 18, except that amplitudes in adjoining rows (as well as in the columns) are independent. Note how the vertical streaking in the background, so predominant in Fig. 18, is largely absent.

recording camera. The basic element changes its linear dimensions with range, of course. Whether the modified element did so would be largely a matter of choice.

If the k-value for the average within the desired element of resolution is too low, i.e. leaves too much uncertainty as to the correct signal mean strength, one can superimpose successive scans.* Relative motion of the scatterers is almost certain to provide effective independence of data for successive scans. Some sort of memory device would be required, of course, and the simplest would seem to be a photographic record.

As has been pointed out previously (Section 2) signal intensities or A^2's are directly additive, but $\overline{A^2}$, $\overline{A}$, and $\overline{\log A}$ or $\overline{\log A^2}$ have fixed relationships among them, so that any one of A^2, A, or their logarithms or some other function of A^2 can be averaged, so long as the correct factor is introduced. It must be borne in mind, of course, that

$$\overline{A^2} \neq (\overline{A})^2 \neq \log^{-1}(\overline{\log A^2}).$$

Use of A, still more so of $\log A^2$, reduces the range of signal strength over which the amplifiers and cathode ray tube are required to behave proportionately.

There is another way, of limited applicability, of reducing the proportional response requirement. That is to generate a black-and-white picture, i.e. one of extreme contrast, rather than one of continuous gradation. All signals above a

*A "sweep" is the line traced on the display tube as the pulse moves out from the radar. As the antenna rotates once about a vertical axis, or completes one up and down motion in a vertical plane, the picture caused by all sweeps is called a "scan".

certain threshold are recorded "white", all below that threshold "black". Then the camera or other memory device simply records the amount of white signal in a given area in one or any specified number of scans, this being the fraction of signal above a given threshold. This fraction has been related to A^2 in Section 3, and its corresponding application to A-scope observations was discussed above. The range of signal strength over which this technique works well is only about 10 db. Amplifiers might possibly be designed, however, in which the signal recorded comes from the first saturated stage of the amplifier, or from the one preceding. (Such amplifiers have actually been designed for continuous signals.) The fractional technique applied to this type of amplifier should provide equipment giving reasonable precision over a wider range of signal intensities.

6. EFFECTS OF BACKGROUND NOISE

Fluctuating Signals in the Presence of Background Noise

The echo arriving back at a radar from a random array of scatterers has been discussed at length. Its average strength is related to the properties of the distributed target; but all that is known about its instantaneous value is a probability distribution. When the echo enters the circuits, it combines with a random background signal originating in the circuits; this background will have a probability distribution of much the same sort, depending on the circuit parameters. On the assumption that the two statistics are, in fact, identical, echo plus background has the same distribution as an echo from a stronger target.

The signal arriving back from a single point target has a specific strength, a probability distribution of zero width. When it enters the circuits, and combines with the background signal, however, the combination no longer has a specific value, but a probability distribution whose width or standard deviation is a function of the relative strength of signal and background. The instantaneous output signal (the signal leaving the receiver) then can never be predetermined specifically, unless the target is a single point (or some equivalent nonrandom array) *and* infinitely stronger than the random background.

Whatever the probability distribution of the output signal, that for an average of k such independent signals will have a standard deviation proportional to $k^{-(1/2)}$. If the random component of the output signal is due to circuit fluctuations, those fluctuations can be trusted to achieve independence in the interval between consecutive radar pulses. When the major part of it is due to the random array of the target elements, say raindrops, the time to independence may be great compared with the interval between radar pulses.

The interplay of the ratio of echo intensity to background noise intensity, m^2, and of k, the number of independent signals available, is displayed in Fig. 20 for both fluctuating and steady echoes. Here lines of constant standard deviation σ, taken as a fraction of the mean echo intensity, are drawn. Solid lines apply when the incoming echo fluctuates about a mean intensity $\overline{A}^2$ before being mixed with the background noise in the receiver. The broken lines apply when the incoming echo has a fixed intensity S^2; here, the fluctuations, of which σ is the standard deviation, are due entirely to the noise background.

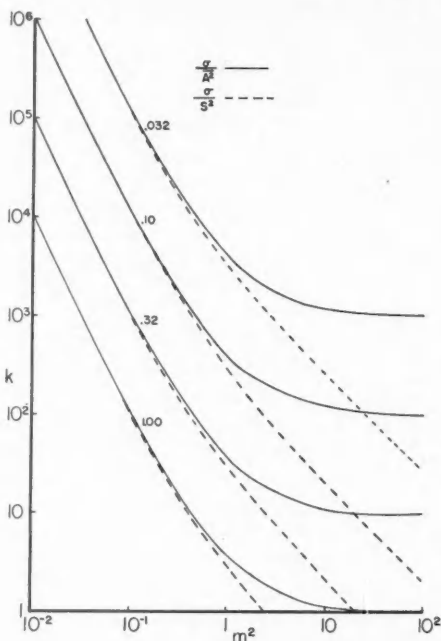In both cases, increasing k consistently decreases the standard deviation

FIG. 20. Lines of constant standard deviation (expressed as fractions of mean echo intensity); k is the number of independent data available, m^2 is the intensity ratio (echo/background). Solid lines for fluctuating, broken lines for steady, echoes.

$(\sigma \propto k^{-(1/2)})$. In the case of a steady signal (broken lines), increasing the echo/background ratio m^2 consistently decreases the standard deviation, although at a gradually diminishing rate. In the case of a fluctuating input signal (solid lines), increasing m^2 decreases σ only until m^2 reaches a value of about ten. Higher values of m^2 do not appear to be any more useful; σ cannot, in fact, be reduced below $\overline{A^2}/\sqrt{k}$. This brings out again the main thesis of the present paper: signals from rain and similar random arrays have a measure of uncertainty associated with them which can be overcome by averaging independent data, but cannot be improved (beyond $m^2 \doteq 10$) by increasing the strength of the signals. Every such signal carries an uncertainty equivalent to $m^2 = 1$ before it ever enters the circuits.

The solid lines of Fig. 20 are based on the theory of Sections 2 and 3 and on the results shown in Table I. Thus

$$[23] \qquad \frac{\sigma}{\overline{A^2}} = \frac{\sigma_1}{\sqrt{k}} \frac{1}{\overline{A^2}} = \frac{\overline{A^2} + \overline{B^2}}{\sqrt{k} \ \overline{A^2}} = \frac{m^2 + 1}{m^2 \ \sqrt{k}},$$

where $m^2 = \overline{A^2}/\overline{B^2}$ is the "echo/noise ratio", $\overline{B^2}$ being the mean intensity of the background noise; σ_1 is the standard deviation of the fluctuating output signal

when one independent datum is available (i.e. for $k = 1$). This quantity is equal (Table I) to the mean intensity of echo plus background.

For the broken lines, the theory given by Goldstein (3) has been used. Goldstein (his equation (175)) shows that

$$\sigma_1/(S^2 + \overline{B^2}) = \sqrt{1 + 2m^2}/(1 + m^2)$$

where σ_1 is the standard deviation of the steady echo mixed with the background when $k = 1$, while S^2 is the intensity of the steady signal. Using $m^2 = S^2/\overline{B^2}$ and $\sigma = \sigma_1/\sqrt{k}$, the equation

[24] $$\sigma/S^2 = \sqrt{1 + 2m^2}/m^2\sqrt{k}$$

for the broken lines is obtained.

Detectability of Weak Echoes

Increasing k has just been shown to aid materially in the precise measurement of a fluctuating echo in the presence of a background noise; in addition, large values of k make possible the *detection* of fluctuating echoes which are weak compared to the background noise.

In Section 3, the probability distributions $P(J_k)$ of the average of k independent signal measurements (equation [13]) and $Q_k(\overline{A^2})$ of the true mean intensity in terms of J_k (equation [14b]) were derived. Table I lists the corresponding standard deviations:

[25]   for $P(J_k)$: $\overline{A^2}/\sqrt{k}$

[26]   for $Q_k(\overline{A^2})$: $J_k k/[(k - 2)\sqrt{k - 3}]$.

The distributions themselves are sketched in Figs. 3 and 4. Their appearance suggests—and this can be proved rigorously—that both functions tend towards a Gaussian probability distribution with standard deviations [25] or [26] as k increases.

Since the noise background too follows these distributions, it is evident that provided a sufficient number of observations of it are made, an exact value of the noise level may be assumed to be known. Let this value be a.

Consider now that k independent signal measurements, each signal consisting of background noise plus possibly an echo, have been made. For simplicity, let k be large enough (say greater than about 50) for the Gaussian approximations to be usable. If the resulting average of the k intensities, J_k, happens to coincide with the noise intensity a, the probability distribution of the true signal average $\overline{A^2}$ will be a Gaussian centered at a and having the standard deviation of equation [26]. It then follows from symmetry that there is a half-chance that the true value of the echo + noise should be above a, i.e. that there is an echo. There is also a half-chance, of course, that the signal is due only to noise.

Assume now that a fluctuating echo is being received, for which the true mean (echo + noise) power is c $(>a)$. The probability distribution of the received signal for any value of k is then equation [13] or its Gaussian approximation, and the probability R of this echo plus noise giving rise to a signal greater than a may be worked out. This R may be interpreted as the chance of getting a return greater than a, and hence the chance of getting a return which permits the ob-

server to assert with greater than 50% confidence that he is looking at a real target. The 50% curves of Fig. 21 show this probability R as a function of $c - 1 = m^2$, the echo/background ratio, for three values of k.
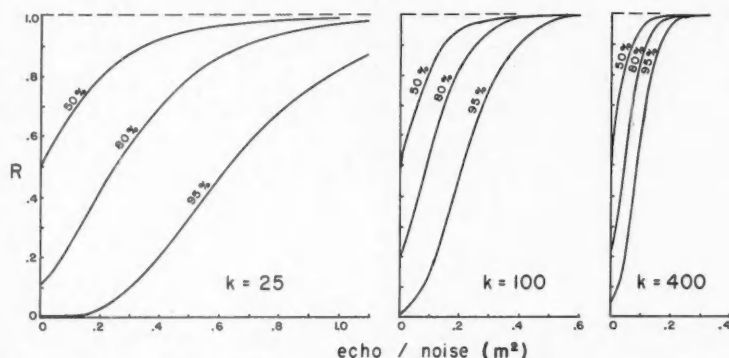

FIG. 21.   The probability R that for a given mean echo, the average of $k = 25$, 100, or 400 echo + noise intensities will inspire in the observer a confidence greater than 50, 80, or 95% that an echo exists.

For a higher than 50% confidence, it is necessary to analyze the distribution $Q_k(\overline{A^2})$ further. It is found, for instance, that, for $k = 100$, signals (echoes + noise) falling at $b = 1.209a$ inspire an 80% confidence that an echo exists. The probability R is then simply the chance that a signal of mean power c gives rise to an average power greater than $1.209a$ in $k = 100$ cases. In this way, the 80% and 95% confidence curves of Fig. 21 may be calculated. These curves are plotted against m^2; the point 1.0 on the abscissa thus indicates an echo of the same power as the noise. This is the echo strength which for low values of k is often regarded as "minimum detectable". It has been noted before that in the case of random targets several independent data must always be examined together. For this reason it would appear that for fluctuating signals from random targets the threshold of detectability is in all cases well below noise level.

The results shown in Fig. 21 apply when k independent signals are *averaged*. In Section 3 the alternative and practically more attractive method of analyzing k data, by counting the fraction p/k of them which exceed a given threshold, was described. The criterion of detectability of echoes utilized in this way may be constructed in an analogous manner. The resulting curves for R versus m^2 are very similar to those shown in Fig. 21 for averaging, except that they are displaced towards the right by a factor about 1.3, when $k = 100$; this means that in counting, the echo has to be about 1 db. stronger than in averaging, in order to be detectable with the same precision.

SUMMARY

Randomly distributed scatterers give rise to echoes widely fluctuating in intensity about a mean which is generally the only quantity of physical interest.

Straight averaging of the data (whether of intensity, amplitude, or intensity

level is immaterial) is the most obvious way of obtaining the mean. The width of the fluctuations reduces by $\sqrt{k}$, where k is the number of independent data involved. But in practice averaging is both difficult and costly. A more readily realized alternative (involving only on–off type of response in the equipment) consists of classifying the signals and counting the fraction falling above a given threshold. This procedure yields the desired mean slightly less rapidly than ordinary averaging, provided the threshold is picked judiciously (to within ±4 db.), or else provided that a sequence of thresholds, spaced not further apart than 8 db., is available.

Another simple alternative to averaging consists of superimposing many independent traces on an A-scope type display. The *details* of the individual traces are lost, and a continuous gradation of luminance results. The location of the brightest portion of the screen corresponds to the peak of the distribution curve of the signal function displayed. The mean value of the signal intensity may then be deduced easily. This technique fails when the receiver is square-law, as the distribution law of signal intensity has its maximum at zero intensity. Linear or logarithmic receivers would seem almost equally suitable for the purpose.

The above techniques involve independent data. From any emitted pulse, these are received at the rate of one per pulse duration. Shortening the pulse duration, or alternatively, receiving echoes from each pulse by separate antennas, increases the amount of independent information available, though only at a cost in signal power.

The number of independent data may be increased substantially (by a factor between 5 and 20) and at no loss of power, by transmitting consecutive pulses at slightly different radio frequencies. A difference in frequency of only about $1/\tau$, where τ is the unvarying pulse duration, ensures complete independence of consecutive pulses. The frequency need only be varied until the natural reshuffling among the particles produces the independence needed.

In general, receivers with logarithmic response characteristics are most suitable with random targets, such as are involved in weather radar. Their ability to respond over the wide range of power encountered in such echoes reduces appreciably the incidence of saturation. Further, because they are made up of several successively saturating stages, logarithmic amplifiers permit readily the establishment of the several thresholds which are desirable in the classifying and counting method of signal analysis.

The precision of measuring the intensity of echoes from *steady* targets observed against a fluctuating noise background improves by an increase in either k, the number of independent data available, or the echo/noise ratio m^2. For *fluctuating* echoes, the echo/noise ratio is not quite so important; its increase beyond about 10 adds practically nothing to the precision of measurement, while an indefinite improvement in precision may be secured by a sufficient increase in k. Large values of this quantity similarly permit the *detection* of fluctuating echoes amounting in strength to only a small fraction of the background noise.

REFERENCES

1. BARTNOFF, S., ATLAS, D., and PAULSEN, H. Proceedings of the Third Radar Weather Conference, McGill University, Montreal, Quebec. Sept. 15–17.   1952.
2. BROWN, R. H., JENNISON, R. C., and DAS GUPTA, M. K.   Nature, 170: 1061.   1952.
3. GOLDSTEIN, H.   Sections 6.13–6.21. *In* Propagation of short radio waves, Vol. 13 of Radiation Laboratory Series. *Edited by* D. E. Kerr. McGraw-Hill Book Company, Inc., New York.   1952.
4. RAYLEIGH, LORD.   The theory of sound. Vol. I. Dover Publications, New York.   1945. pp. 35–42.
5. WALLACE, P. R.   Can. J. Phys. 31: 995.   1953.
6. WOLD, H.   Random normal deviates, Tract No. XXV. *In* Tracts for Computers. Cambridge University Press, London.   1948.

INTERPRETATION OF THE FLUCTUATING ECHO FROM RANDOMLY DISTRIBUTED SCATTERERS. II[1]

BY P. R. WALLACE[2]

ABSTRACT

The determination of the probability distribution for the magnitude of a radar echo from randomly distributed scatterers is a standard problem of the "random walk" type. We are concerned with the information to be gained about the scatterers from observation of the echoes, and the methods whereby this information may be extended. The method of averaging independent signals is investigated, and compared with the method of continuous averaging, which is found to be somewhat better. By appropriate variation of frequency of the radiation, it is found possible to obtain effectively independent determinations from a given region, and hence to derive more precise information about it. Finally, the continuous variation of signal with time is studied, and a simple picture of the development of the signal proposed. The Markoff method is used throughout.

1. INTRODUCTION

If a radar signal is directed toward atmospheric precipitation and the echo from that precipitation studied, limited information about the scatterers may be obtained. Neither the size of the scattering droplets nor their density may be determined directly; but if a drop-size distribution is assumed, information about each may be inferred. Since the echo to be expected from a given distribution of scatterers is subject to wide statistical fluctuation, no precise information may be obtained from an individual echo.

We note that at any particular time t after emission of the signal, the echo being received is a superposition of waves back-scattered from all particles in the range of distance between $\frac{1}{2}c(t - \tau)$ and $\frac{1}{2}ct$ from the station, and within the angular range of the outgoing beam, τ being the duration of the emitted pulse. Thus, with the passage of time, we scan a region of space whose near and distant frontiers are both receding from us at a rate equal to half the velocity of light. Echoes received at intervals of time τ come from completely different regions and the signals received are therefore independent. If it were known that the density and size distribution of scatterers were constant over a number of these independent regions of length $\frac{1}{2}c\tau$, we might make use of the several independent measurements of signal to gain more precise information; however, this presumably assumes part of what one would like to know.

We have undertaken, in Sections 3 and 4, a calculation of the probability distribution of the precipitation parameters which can be inferred from a sequence of independent measurements, and also from a continuous recording of the echo from the same region. The latter is found to be somewhat, though not spectacularly, superior. Some further insight into this problem may be acquired by studying the development of the signal as the frontiers of the scattering region recede.*

The analysis will also be applicable to the variation of signal as the region changes owing to lateral sweeps.

It has been found possible to make a rather simple picture on the basis of which the autocorrelation of signals separated by a given time interval may be studied.

Finally, a proposal by Marshall (1) permits the determination of independent signals from a given region of view. This is accomplished by changing the frequency of the radiation used. This effectively reshuffles the phases at which the radiation is scattered from the various droplets—and does it in a random way, provided the phase change is appropriately chosen. We have developed in Section 6 the quantitative theory of this method.

It should be remarked that we are neglecting throughout the random spatial reshuffling of the scatterers. This will be justifiable if measurements are made within a time appreciably smaller than that required for random radial displacements of the order of one wave length to take place. Ultimately, of course, this effect will itself so redistribute the phases as to create an independent signal.

2. ECHO FROM RANDOM SCATTERERS BY THE MARKOFF METHOD

Suppose that a pulse is emitted at wave length λ cm. and constant amplitude, and is h cm. long, so that it contains

[2.1]
$$n_0 = h/\lambda$$

wave lengths.

Now consider a scatterer at linear distance r from the station. Its contribution to the echo will commence at a time $2r/c$ from the beginning of the emission of the pulse; this signal will be

[2.2]
$$z = ae^{i\omega(t-2r/c)} \text{ for } 2r/c < t < (2r/c) + \tau,$$
$$= 0 \qquad \text{for } t < 2r/c \text{ or } t > (2r/c) + \tau.$$

The amplitude a will depend on the size of the scatterer and also on its distance from the receiver—the latter owing to solid angle effects. If this complication is neglected—a justifiable approximation if relative distances from the source do not vary too much—and if the size distribution is assumed everywhere the same, the signal is given by

[2.3]
$$Z = e^{i\omega t} \bar{a} \sum_n e^{-2iKr_n}$$

where $\bar{a}$ is the average scattering amplitude, and $K = \omega/c$. The summation is over all particles lying in the range of distance

[2.4]
$$\tfrac{1}{2}ct - \tfrac{1}{2}h < r_n < \tfrac{1}{2}ct.$$

To find the probability of a given value of $Z = X + iY$ we must weight the probability of this value when the number of scatterers contributing is N, with the probability that these are in fact N scatterers. If the linear density of scatterers is σ, this latter probability is given by the Poisson distribution

[2.5]
$$p_N = \frac{\bar{N}^N}{N!} e^{-\bar{N}}$$

where $\bar{N} = \tfrac{1}{2}\sigma h$ is the average value of N.

To calculate the probability distribution of the signal from N random scatterers, as in all later problems, it is most convenient to use the Markoff method.

We shall recall briefly the conventional treatment of the problem by this method. We consider an N-dimensional space with coordinates $r_n (n = 1, 2, \ldots, N)$. Each point in this space for which all coordinates are between 0 and $h/2$ will represent a possible disposition of the N particles, all having equal a priori probability. Thus the probability that the real and imaginary parts of Z lie in the ranges $(X, X + dX)$, $(Y, Y + dY)$ respectively will be the proportion of the volume $(\frac{1}{2}h)^N$ lying between the surfaces

$$\cos 2K r_n = X, X + dX$$

and also

$$\sin 2K r_n = Y, Y + dY.$$

If a function δ which is unity in this region, zero outside, is defined, it is clear that the required probability is

[2.6] $$P_N(X, Y) \, dX dY = \int_0^{\frac{1}{2}h} dr_1 \ldots \int_0^{\frac{1}{2}h} dr_N \left(\frac{2}{h}\right)^N \delta.$$

Now let us introduce the two-dimensional Fourier transform $\phi_N(\xi, \eta)$ of $P_N(X, Y)$. Taking transforms of both sides of [2.6] we find that

$$\phi_N = [J_0(\rho)]^N$$

where $\rho^2 = \xi^2 + \eta^2$, one J_0 coming from the integration over each coordinate r_n. Here J_0 designates the conventional Bessel function of order zero. Therefore the probability of a signal in $(X + dX, Y + dY)$ is given by

$$P(X, Y) = \sum_N p_N P_N(X, Y)$$

[2.7] $$= \frac{1}{(2\pi)^2} \int_{-\infty}^{\infty} \int_{-\infty}^{\infty} \exp\left[-\bar{N}(1 - J_0(\rho))\right] e^{-i(\xi X + \eta Y)} \, d\xi \, d\eta.$$

In the limit of large N it is sufficient to replace $1 - J_0(\rho)$ by its approximate value $\frac{1}{4}\rho^2$ for small ρ; the integral is then easily evaluated to give

[2.8] $$P(A) \, dA = \frac{2A}{\overline{A^2}} e^{-A^2/\overline{A^2}} \, dA$$

where $\overline{A^2} = \bar{N}\bar{a}^2$; or alternatively

[2.9] $$P_0(I) \, dI = \frac{1}{\bar{I}} e^{-I/\bar{I}}$$

where $I = A^2$. This is the familiar "random walk" solution (2). We note that what we have obtained is a distribution in intensity A^2.

Before going on to specific applications, we might mention two advantages of the Markoff method in problems of this type.

1. It yields first the Fourier transform of the distribution required. Thus, even if the inversion cannot be carried out, we may obtain the moments of the distribution by differentiation; e.g. if $q(\xi)$ is the transform of the distribution $p(x)$,

$$\bar{x} = -i q'(0),$$

[2.10] $$(\Delta x)^2 = [q'(0)]^2 - q''(0), \text{ etc.}$$

2. In problems concerned with chains of processes, we can make use of the fact

that the probability distribution of the result of the chain is the convolution of the probability distributions of the individual steps. Therefore, using a familiar theorem of Fourier analysis, the transform of the complete probability is the product of the transforms of the component probabilities.

3. DISTRIBUTION OF THE AVERAGE OF INDEPENDENT SIGNALS

Suppose that, either by lateral sweeps or by measurements at pulse-length intervals, we obtain k different independent intensity measurements $I_1, \ldots, I_k$. Let us designate their average as J_k. Now by the convolution theorem of the previous section, the transform of the probability distribution for the sum of the determinations is the product of the transforms of the probabilities of the individual determinations; since the latter are identical,

[3.1] $$\pi(\xi) = [q_0(\xi)]^k$$

where $q_0(\xi)$ = transform of $P_0(I)$,

$\pi(\xi)$ = transform of the distribution of $kJ_k = Y_k$.

Since direct calculation gives

[3.2] $$q_0(\xi) = \frac{i/\bar{I}}{\xi + i/\bar{I}},$$

we get, on evaluating the inverse transform of $[q_0(\xi)]^k$ by contour integration, for the distribution of the sum Y_k

[3.3] $$\frac{1}{(\bar{I})^k} \frac{Y_k^{k-1}}{(k-1)!} e^{-Y_k/\bar{I}}.$$

Consequently for the distribution of J_k

[3.4] $$P_k(J_k) = \frac{k^k J_k^{k-1}}{(\bar{I})^k (k-1)!} e^{-kJ_k/\bar{I}}.$$

This result does not quite answer the practical question, namely: to what accuracy can we determine the mean intensity $\bar{I}$, which depends on the mean scattering amplitude from a single particle and the particle density, when our information consists of k independent intensity measurements? However, the distribution of $\bar{I}$ for a given J_k can be deduced from [3.4]. The *relative* probabilities are

[3.5] $$\frac{1}{(\bar{I})^k} e^{-kJ_k/\bar{I}}$$

and the absolute probability may be obtained by normalization. The normalization integral is only convergent for k at least 2. This arises from the fact that, for a single intensity measurement, there is always an overwhelming probability that it came from an indefinitely large $\bar{I}$! The fact that we do not really admit this overwhelming probability is based on considerations quite extraneous to the measurement made, that is to say, our conviction on physical grounds of the finite character of the disturbance from which the echo comes.

For $k \geqslant 2$ we find the distribution

[3.6] $$Q_k(\bar{I}) = \frac{(kJ_k)^{k-1}}{(k-2)!} \frac{1}{\bar{I}^k} e^{-kJ_k/\bar{I}}.$$

From these we calculate immediately

$$(\bar{I})_{\text{AV}} = \frac{k}{k-2} J_k,$$

[3.7]

$$(\Delta\bar{I})^2 = \frac{k^2}{(k-2)^2(k-3)} J_k^2.$$

In general, the nth moment is finite only for $k \geqslant n + 2$. In particular, at least four independent measurements are needed to give information about $\bar{I}$ with finite probable error, and even then $\Delta\bar{I} = 2J_4$, a very wide spread. For $k = 10$, $\Delta\bar{I} = 0.47J_{10}$, a result which is considerably greater than the r.m.s. deviation in J_{10} for fixed $\bar{I}$, namely $\Delta J_{10} = 0.31\bar{I}$. In the limit of large k, the fractional r.m.s. errors tend to become equal.

The distributions $P_k(J_k)$ and $Q_k(I)$ are shown in the accompanying paper of Marshall and Hitschfeld (1), Figs. 3 and 4.

4. DISTRIBUTION OF CONTINUOUSLY AVERAGED SIGNALS

Suppose now we consider the average signal over m pulse lengths, and see whether it offers the possibility of greater accuracy in the determination of $\bar{I}$. It is clear that it must be at least as good as the averaging of independents, since all data contained in them are used in the continuous averaging process.

Suppose we take the time at which the averaging is begun as $t = 0$. The particles then contributing to the signal lie, according to [2.4], in the coordinate range

  (i) $-h/2 < r_n < 0$ (Region R_1).

Particles in this region contribute to the average for time $< \tau$.

In the region

  (ii) $0 < r_n < (m-1)h/2$ (Region R_2)

are particles which do not contribute to the signal either at the beginning or the end, but each contributes for a total time τ.

In the region

  (iii) $(m-1)h/2 < r_n < mh/2$ (Region R_3)

lie particles which contribute to the signal at the end of the interval of averaging, but contribute altogether for time $< \tau$.

We are now interested in the intensity $I = ZZ^*$ (see equation [2.3]). The time average of I is immediately calculable and is

[4.1] $I_t = \sum_{r_n} E_1(r_n) + 2 \sum_{r_n \neq r_{n'}} \cos 2K(r_n - r_{n'}) E_2(r_n, r_{n'})$

where

$$E_1(r_n) = \frac{1}{m}(1 + 2r_n/h) \text{ in } R_1,$$

[4.2]

$$= \frac{1}{m} \text{ in } R_2,$$

$$= \frac{1}{m}\left[1 - \frac{2(r_n - \frac{1}{2}(m-1)h)}{c}\right] \text{ in } R_3$$

and

$$E_2(r_n, r_{n'}) = \frac{1}{m}\left(1 + 2\,\frac{\min\,(r_n, r_{n'})}{c}\right)\,(r_n, r_{n'} \text{ in } R_1),$$

[4.3]
$$= \frac{1}{m}\left(1 - \frac{2r_n - r_{n'}}{c}\right) \text{ (at least one of } r_n, r_{n'} \text{ in } R_2 \text{ and}$$

$$|r_n - r_{n'}| < \tfrac{1}{2}h),$$

$$= \frac{1}{m}\left[1 - 2\,\frac{\max\,(r_n, r_{n'}) - \tfrac{1}{2}(m-1)h}{c}\right]\,(r_n, r_{n'} \text{ in } R_3).$$

It is evident that it would be difficult to obtain the distribution of I_t; however, it is quite feasible to get its mean-square deviation

$$\Delta I_t = [\overline{I_t^2} - (\overline{I_t})^2]^{\frac{1}{2}}.$$

In the calculation of $\overline{I_t^2}$, the cross-product of the first and second terms in [4.1] drops out, as do cross-products between the terms of the second series. Also, in the squared terms arising from the second series, $\cos^2 2K(r_n - r_{n'})$ may be replaced by $\tfrac{1}{2}[1 + \cos 4K(r_n - r_{n'})]$; the contribution from the oscillating term is then $1/n_0$ of that from the constant (n_0 being the number of waves in the pulse), and may therefore be neglected.

Direct computation of the integrals then yields the result:

[4.4]
$$(\Delta I_t)^2 = \bar{I}^2(4m - 1)/6m^2$$

where $\bar{I}$ is the mean intensity.

Now the region over which the average has been calculated contains $(m + 1)$ independent regions. The r.m.s. deviation of the average of the $(m + 1)$ independent signals is

[4.5]
$$\Delta J_{m+1} = \bar{I}/\sqrt{m + 1}.$$

The ratio of the mean square deviations, which we shall call the "factor of improvement" f, is

[4.6]
$$f = \frac{(\Delta I_t)^2}{(\Delta J_{m+1})^2} = \frac{(4m - 1)(m + 1)}{6m^2}.$$

We list a few values in Table I: We note in particular that there is no improvement unless the average is taken over more than one pulse duration. At best, the reduction of the r.m.s. deviation due to averaging does not exceed 22.5%.

TABLE I

m	1	2	3	4	5	10	20	50	∞
f	1	0.88	0.81	0.78	0.76	0.72	0.69	0.68	2/3

Put differently, we can give the number of independent signals which give the same r.m.s. deviation as the continuous average over the duration of m pulses. This is given in Table II.

TABLE II

m	1	2	3	4	$m \geqslant 4$
N_e	2	3.4	4.9	6.4	$\frac{3}{2}m + \frac{3}{8}$

It should be noted that if we are again interested in obtaining the distribution of true mean intensity $\bar{I}$ from a known signal, a further analysis is necessary. Roughly, we may estimate the result in this way: we assume that the continuous average is equivalent to the average of $(m + 1)/f$ independent signals, as indicated in Table II. If the average is over 10 or more intervals, to a good approximation

[4.7] $$(\Delta \bar{I})^2 \approx \frac{2}{3} \frac{(m + 1)^2}{(m - \frac{1}{3})^2 (m - 1)} I_t^2 \approx \frac{2}{3m} I_t^2$$

(see [3.7]); so that we get the same factor of improvement as in the converse problem. This is to be expected, in view of the similarity of the distributions for averages over reasonably large numbers of pulse lengths.

5. CONTINUOUS VARIATION OF THE SIGNAL INTENSITY*

We now turn to a somewhat different problem: that of the variation of the signal as the region scanned is varied. We ignore the motion of the individual scatterers, but consider the evolution of the signal as the region from which the signal is received recedes continuously into the distance. Alternatively, the analysis applies equally well to the case in which the direction of the outgoing beam is altered, and the signal varies owing to a lateral sweeping. Finally, although the continuous variation is studied, the results may be used to relate signals received from any two regions which partially overlap.

Let us look for the probability that the complex vector representing the echo be $\mathbf{A}_0$ at an initial time, and $\mathbf{A}$ at a time t later. The signal at the initial time will come from a region of length $\frac{1}{2}h$, which we shall designate $0 < r < \frac{1}{2}h$; at the later time it will come from the interval $ct/2 < r < ct/2 + h/2$. Let us assume that there are N_1 particles in $(0, ct/2)$, contributing to the first signal only; N_2 in $(ct/2, h/2)$ contributing to both; and N_3 in $(h/2, h/2 + ct/2)$ contributing to the latter one only. The first signal will then have components X_0, Y_0 given by

$$X_0 = \sum_{N_1} \cos 2Kr_n + \sum_{N_2} \cos 2Kr_p,$$

$$Y_0 = \sum_{N_1} \sin 2Kr_n + \sum_{N_2} \sin 2Kr_p.$$

The second is given by

$$X = \sum_{N_2} \cos 2K(r_p - \tfrac{1}{2}ct) + \sum_{N_3} \cos 2K(r_q - \tfrac{1}{2}ct),$$

$$Y = \sum_{N_2} \sin 2K(r_p - \tfrac{1}{2}ct) + \sum_{N_3} \sin 2K(r_q - \tfrac{1}{2}ct).$$

*Results similar to some of those in this section have been given by Siegert (3) (1943) and (4) (1946) in connection with the variation of signal solely due to the motion of the scatterers. We include a discussion of this problem in order to point out a simple result (formula [5.3]) and its interpretation (Fig. 1), which make possible a graphic picture of the development with time of the sort of signal with which this paper is concerned.

Now the probability of a signal intensity represented by a vector in dX_0, dY_0 initially and in dX, dY at time t is given by

$$\left(\frac{2}{ct}\right)^{N_1}\left(\frac{2}{h-ct}\right)^{N_2}\left(\frac{2}{ct}\right)^{N_3}\int_0^{\frac{1}{2}ct}\prod_{n=1}^{N_1}dx_n\int_{\frac{1}{2}ct}^{\frac{1}{2}h}\prod_{p=1}^{N_2}dx_p\int_{\frac{1}{2}h}^{\frac{1}{2}h+\frac{1}{2}ct}\prod_{q=1}^{N_3}dx_q\cdot\delta\delta_0$$

where the symbol $\prod$ signifies a product, and

$\delta_0 = 1$ if X_0, Y_0 lies in the required range dX_0, dY_0

$\quad = 0$ otherwise, and

$\delta \; = 1$ if X, Y lies in the required range dX, dY,

$\quad = 0$ otherwise.

Representing the δ's in the usual way by Fourier transformations, we can determine the probability distribution for given N_1, N_2, N_3. Weighting with the usual Poisson distributions for these quantities, we find that the probability that the original signal is in $(X_0, X_0 + dX_0;\ Y_0,\ Y_0 + dY_0)$ and the second one in $(X, X + dX;\ Y,\ Y + dY)$ is

$$dX_0\,dY_0\,dX\,dY\left(\frac{1}{2\pi}\right)^4\int e^{-i(X_0\xi_0+Y_0\eta_0)}d\xi_0\,d\eta_0\int e^{-i(X\xi+Y\eta)}d\xi\,d\eta$$

[5.1] $\qquad \times \exp\left\{-\sigma\left[\tfrac{1}{2}ct(1-F_1)+\tfrac{1}{2}(h-ct)(1-F_2)+\tfrac{1}{2}ct(1-F_3)\right]\right\}$

where

$$F_1 = \frac{2}{ct}\int_0^{\frac{1}{2}ct}\exp\left\{i(\xi_0\cos 2Kr + \eta_0\sin 2Kr)\right\}dr,$$

[5.2] $\quad F_2 = \dfrac{2}{h-ct}\displaystyle\int_{\frac{1}{2}ct}^{\frac{1}{2}h}\exp\left\{i[\xi_0\cos 2Kr + \eta_0\sin 2Kr + \xi\cos 2K(r-\tfrac{1}{2}ct)\right.$

$$\left. + \eta\sin 2K(r-\tfrac{1}{2}ct)]\right\}dr,$$

$$F_3 = \frac{2}{ct}\int_{\frac{1}{2}h}^{\frac{1}{2}h+\frac{1}{2}ct}\exp\left\{i[\xi\cos 2K(r-\tfrac{1}{2}ct)+\eta\sin 2K(r-\tfrac{1}{2}ct)]\right\}dr.$$

Making use of the fact that $\sigma ct/2$ is very large to expand the F's to quadratic terms as in [2.7], [5.1] comes out in terms of Gaussian error integrals. Evaluating, we find that the probability in question is

$P(X_0, Y_0; X, Y)\,dX_0\,dY_0\,dX\,dY$

[5.3]
$$= dX_0\,dY_0\,dX\,dY\left(\frac{1}{\pi\bar I}e^{-A_0{}^2/\bar I}\right)\left(\frac{1}{\pi\bar I(1-\Delta^2)}e^{-|\mathbf{A}-\Delta\mathbf{A}_0{}'|^2/\bar I(1-\Delta^2)}\right)$$

where $A_0{}^2 = X_0{}^2 + Y_0{}^2$,

$\Delta = 1 - t/\tau$ where τ is the pulse duration,

$\mathbf{A}_0{}'$ is the vector obtained by rotating the vector $\mathbf{A}_0$ with components (X_0, Y_0) through the angle $-\omega t$, ω being the circular frequency of the radiation, and $\mathbf{A}$ is the vector with components (X, Y).

The first bracket in [5.3] represents the probability distribution of the original signal; the second, which may be designated $P(\mathbf{A}_0 \to \mathbf{A})$, is the probability distribution after time t, when the initial signal is given by $\mathbf{A}_0$.

If we ignore variations with the frequency of the emitted radiation—consider,

that is, the signal only at intervals of one or several r-f. periods—the distribution at time t is a Gaussian (normal error function) centered on the point $\Delta \mathbf{A}_0$ (a point moving uniformly in toward zero from the initial value $\mathbf{A}_0$) and having a standard deviation $\bar{I}(1 - \Delta^2)$, which increases from zero at $t = 0$ to $\bar{I}$, the value for an independent signal, at $t = \tau$. This is illustrated in Fig. 1.
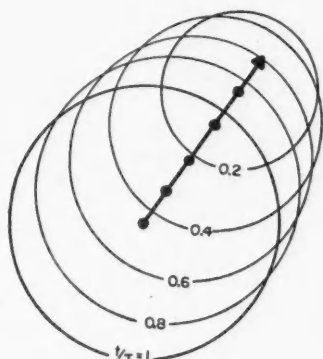

FIG. 1. Straight line represents initial signal amplitude and phase. At later instances, as t approaches τ, the phasors are subject to two-dimensional Gaussian probability distributions. The surfaces representing these distributions are centered, at the times indicated, at the emphasized points, and have standard deviations equal to the radii of the circles. When $t = \tau$, the distribution is that of an independent phasor.

The result [5.3] makes possible the calculation of the frequency distribution of the echo, as calculated in Siegert's papers. Knowledge of the frequency distribution, however, conveys no useful information about the precipitation which returns the echo. The preceding treatment of the development of the signal is the basis for autocorrelation studies, and in addition, provides a simple and graphic picture which aids in the understanding of the correlation of successive signals.

6. THE METHOD OF FREQUENCY VARIATION

Let us consider now the following problem: suppose that a signal of intensity I_0 is received from a given region when the circular frequency is ω_0; what then will be the probability distribution for the intensity I which will be received from the same region when the frequency is ω? We shall assume, as usual, that there is not sufficient time between these measurements to allow the scattering particles to undergo any appreciable movement. If, however, there should be an appreciable random or turbulent motion, it would clearly have the effect of making the successive measurements more independent of each other.

Let (X_0, Y_0) be the real and imaginary parts of the complex vector

[6.1]
$$Z_0 = \sum_{r_n} e^{2iK_0 r_n} \left(K_0 = \frac{\omega_0}{c} \right)$$

where the sum is over the N particles in a half-pulse-length range of length $\frac{1}{2}h$. Suppose also that (X, Y) are the corresponding parts of the vector

$$[6.2] \qquad Z = \sum_{r_n} e^{2iKr_n} \left(K = \frac{\omega}{c}\right)$$

corresponding to an altered frequency ω. The probability that (X_0, Y_0) lies in a given range (dX_0, dY_0) and (X, Y) lies in (dX, dY) is

$$[6.3] \qquad \left(\frac{2}{h}\right)^N \int_0^{\frac{1}{2}h} \delta_0 \delta \, dx_1 \ldots dx_N$$

where δ_0, δ are one when (X_0, Y_0) and (X, Y) respectively are in the ranges in question, zero otherwise.

Representing δ_0, δ as Fourier integrals, transforming to polar coordinates:

$$(X_0, Y_0) \rightarrow (A_0, \theta_0),$$
$$(X, Y) \rightarrow (A, \theta),$$

and for the transformed variables:

$$(\xi_0, \eta_0) \rightarrow (\rho_0, \chi_0),$$
$$(\xi, \eta) \rightarrow (\rho, \chi),$$

we obtain, on integration over θ_0 and θ,

$$[6.4] \qquad \frac{1}{(2\pi)^2} A_0 dA_0 A dA \int \rho_0 \, d\rho_0 \, d\chi_0 \int \rho d\rho d\chi \, . \, J_0(\rho_0 A_0) \, J_0(\rho A) \, b^N(\rho_0, \rho)$$

where

$$[6.5] \qquad b(\rho_0, \rho) = \frac{2}{h} \int_0^{\frac{1}{2}h} \exp\{i[\rho_0 \cos(2K_0 r - \chi_0) + \rho \cos(2Kr - \chi)]\} \, dr.$$

Weighting with the Poisson distribution for the number N of contributing particles, and summing, $b^N(\rho_0, \rho)$ becomes in this integral

$$e^{-N_0(1-b(\rho_0, \rho))}$$

where $N_0 = $ mean of $N = \sigma h/2$.

The next step is to expand b to quadratic terms in ρ_0, ρ. If this is done, and the integrations over χ, χ_0 are performed, we obtain the distribution

$$[6.6] \quad A_0 dA_0 \, . \, A dA \int J_0(A_0 \rho_0) \rho_0 d\rho_0 \int J_0(A\rho) \rho d\rho \, . \, \exp\{-\frac{1}{4}N_0(\rho^2 + \rho_0^2)\}$$
$$\times J_0(\frac{1}{2}i N_0 g_0 \rho \rho_0)$$

where J_0 is the Bessel function, and

$$[6.7] \qquad g_0 = \frac{\sin \frac{1}{2}h\Delta K}{\frac{1}{2}h\Delta K} .$$

Finally, the ρ_0, ρ integrals may be evaluated. Putting $I_0 = A_0^2$, $I = A^2$, we find that the probability of intensity I_0 at frequency ω_0 and I at frequency ω is

$$[6.8] \qquad \frac{1}{N_0} e^{-I_0/N_0} dI_0 \left[dI \, \frac{1}{N_0(1-g_0^2)} \exp\left\{-\frac{I_0 g_0^2}{N_0(1-g_0^2)} - \frac{I}{N_0(1-g_0^2)}\right\} \right.$$
$$\left. \times J_0\left(\frac{2i \, g_0 \sqrt{II_0}}{N_0(1-g_0^2)}\right) \right].$$

The factor in the square bracket, $P(I)\, dI$, is the probability that the intensity at frequency ω is in I, $I + dI$, that at frequency ω_0 being I_0. In Fig. 2, $P(I)$ is plotted for several values of $h\Delta K/2\pi$. In Fig. 3, $g_0{}^2$ is plotted as a function of ΔK and $\Delta\nu$ (solid line).
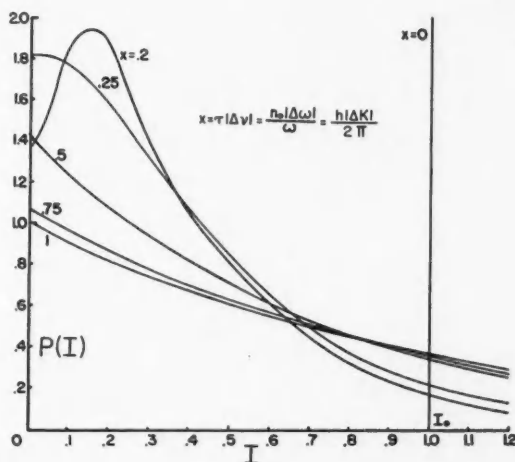
FIG. 2. Probability distributions of the signal intensity I at transmitter frequencies $\nu_0 + \Delta\nu$, given that the intensity is I_0 at frequency ν_0. Each curve is drawn for a fixed value of $x = \tau \mid \Delta\nu \mid$, τ being the pulse duration, h the pulse length, $\omega = 2\pi\nu$, $K = \omega/c$. n_0 is the initial number of wave lengths per pulse length. The curve for $x = 1$ is the exponential distribution of equation [2.9], indicating that I has become completely independent of I_0.

The second signal is now completely independent of the first provided $g_0 = 0$, i.e.

$$\Delta K = \frac{2}{h}\, n\pi \qquad (n = \text{integer})$$

or

[6.9]
$$\frac{\mid \Delta\omega \mid}{\omega} = \frac{n}{n_0},$$

n_0 being again the number of waves in the outgoing signal. Thus, by virtue of a succession of small variations of frequency, independent signals can be obtained, and their average used to obtain an estimate of the mean scattering intensity for a given half-pulse length. This frequency variation should, of course, remain sufficiently small that the scattering cross sections of the particles are not appreciably affected by it.

It may be noted that, for $\Delta\omega/\omega \geqslant 1/n_0$, $g_0{}^2$ is *never* larger than 0.05, so that there is a substantial degree of independence of consecutive measurements at any such frequency shift. Thus, provided one can afford to make the frequency shifts sufficiently large, no very precise control of frequency is necessary.

If we take account of the fact that the emitted wave will not be precisely a
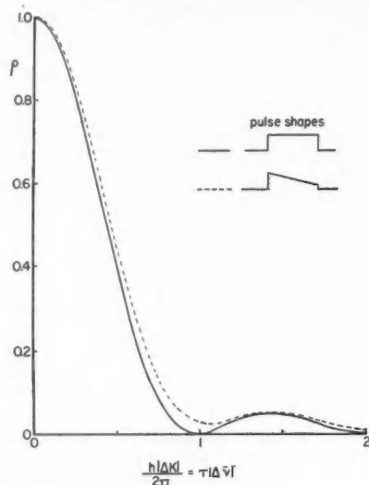
FIG. 3. Variation of ρ, the correlation coefficient between signal intensities I (at frequency $\nu_0 + \Delta\nu$) and I_0 (at frequency ν_0), with $\Delta\nu$. Solid line, for an ideal rectangular pulse; broken line, for a trapezoidal pulse.

It can be proved that ρ, defined as $\bar{I} \times \bar{I}_0 - (\bar{I})^2 / \bar{I}^2 - (\bar{I})^2$, equals the factor $g_0{}^2$ of equation [6.7] and γ^2 of equation [6.17].

square wave, the result will be somewhat altered. Suppose that at any time t the outgoing wave amplitude is modulated by a factor $f(t/\tau)$. We may define the factor so that its mean value is unity, so that

$$\int_0^1 f(u)\, du = 1.$$

t we shall assume to be measured from the initial moment of propagation. We shall write $F(u) = f(1 - u)$, so that

[6.10] $$\int_0^1 F(u)\, du = 1$$

also. The results of the preceding calculation are now altered in that $b(\rho_0, \rho)$ (equation [6.5]) becomes

[6.11] $$b'(\rho_0, \rho) = \frac{2}{h} \int_0^{\frac{1}{2}h} \exp\left\{ iF\left(\frac{2r}{h}\right)\left[\rho_0 \cos (2K_0 r - \chi_0) \right.\right.$$
$$\left.\left. + \rho \cos (2Kr - \chi) \right]\right\} dr.$$

If, as will in general be the case, $F^2(2r/h) = \psi(2r/h)$ varies only slightly over a wave length of radiation,

[6.12] $$1 - b'(\rho_0, \rho) \approx \tfrac{1}{4}[\alpha(\rho_0{}^2 + \rho^2) + 2\rho\rho_0 G]$$

where

[6.13] $$\alpha = \int_0^1 \psi(u)\, du = 1 + \int (\Delta F)^2\, du,$$

ΔF being $(F - 1)$, the deviation of the form factor F from its mean value. Also

[6.14] $$G = C(h\Delta K) \cos \Delta\chi + S(h\Delta K) \sin \Delta\chi$$

where C is the Fourier cosine transform of $\psi(u)$ for argument $h\Delta K$, and S is the corresponding sine transform.

Putting

[6.15] $$\sqrt{C^2 + S^2} = H(h\Delta K),$$

we see that $\alpha = H(0)$. We may now calculate the distribution exactly as before; the probability that I_0 lies in dI_0 and I in dI is

[6.16]
$$\tilde{\omega}(I, I_0) \, dI \, dI_0 = \frac{1}{\bar{I}^2(1 - \gamma^2)} \exp\left\{ -\frac{I_0}{\bar{I}(1 - \gamma^2)} - \frac{I}{\bar{I}(1 - \gamma^2)} \right\}$$
$$\times J_0\left(\frac{2i\,\gamma\sqrt{II_0}}{\bar{I}(1 - \gamma^2)} \right) dI \, dI_0$$

where $\bar{I}$ is the mean intensity, and

[6.17] $$\gamma = \frac{H(h\Delta K)}{H(0)},$$

H being the magnitude of the Fourier exponential transform of the modulation function ψ.

We can consider as the simplest case of interest, that in which the intensity falls off linearly over the duration of the pulse:

[6.18] $$\psi(u) = 1 + \beta(u - \tfrac{1}{2}), \quad (0 < u < 1).$$

Introducing $\mu(<\pi/2)$ such that

$$\tan \mu = (1 - \tfrac{1}{2}\beta)y/\beta$$

and

$$\Phi = \sqrt{(1 - \tfrac{1}{2}\beta)^2 + \beta^2/y^2},$$

we can easily verify that

[6.19]
$$C(y) = -\frac{\sin \tfrac{1}{2}y}{\tfrac{1}{2}y} \Phi \sin (\tfrac{1}{2}y - \mu) + \frac{\beta}{y} \sin y,$$
$$S(y) = \frac{\sin \tfrac{1}{2}y}{\tfrac{1}{2}y} \Phi \cos (\tfrac{1}{2}y - \mu) - \frac{\beta}{y} \cos y.$$

We then see that $C + iS$ and therefore H can never be zero, and there is no frequency shift for which the measurements are completely independent.

However, from a practical viewpoint, this result is not unduly perturbing since, for the values of ΔK which give $\gamma = 0$ for a square wave, namely,

$$h\Delta K = 2\pi \times \text{integer},$$

γ^2 becomes

$$\frac{\beta^2}{(h\Delta K)^2} = \frac{\beta^2}{4\pi^2 \times (\text{integer})^2}.$$

Since it is unlikely that β will be >1 (ratio of intensities at two ends of the

wave 3:1), the correlation is quite small and a high degree of independence is assured. Once again, too, the correlation is consistently quite small for $h\Delta K > 2\pi$.

A comparison of the results for a rectangular pulse and for one of linearly decreasing (or increasing) intensity is given in Fig. 3.

A second form of modulation which might be considered is one symmetrical about the center point of the pulse:

[6.20] $$\psi(u) = \psi(1 - u).$$

In this case it may be shown immediately that

$$H(h\Delta K) = 2 \int_0^{\frac{1}{2}} \psi(u) \cos h\Delta K(u - \tfrac{1}{2}) \, du.$$

If, on the half-pulse range

$$\psi(u) = 1 + \beta'(\tfrac{1}{4} - u),$$

we get

$$H(h\Delta K) = 2\left[(1 + \tfrac{1}{4}\beta') \frac{1}{h\Delta K} \sin \tfrac{1}{2}h\Delta K - \frac{\beta'}{(h\Delta K)^2}(1 - \cos \tfrac{1}{2}h\Delta K) \right].$$

This is zero whenever

$$h\Delta K = 4\pi n, \qquad (n = \text{integer}).$$

In this case we get *complete* independence for intervals twice as great as those which give it for a rectangular pulse; however, halfway between there is again approximate independence in the sense of the previous paragraph.

7. CONCLUSIONS

Information obtainable about atmospheric disturbances from radar echoes is such that one cannot differentiate between "weak" scattering from an extremely large density of scatterers and "strong" scattering from a smaller density, so long as (number of scatterers) × (intensity per scatterer) is the same. If a drop-size distribution is assumed known, however, the number and size individually can be inferred from the mean intensity scattered from a given region.

To establish the mean scattered intensity with reasonable accuracy requires a considerable number of individual intensity measurements. These may be made over a number of different regions, provided it is known (or assumed) that these regions are homogeneous. If the echo from these regions is investigated by recording the return from a given emitted signal, it is found to be somewhat better to average the echo intensity continuously rather than only at such intervals that the signals are independent.

On the other hand, the mean intensity from the single region which contributes to the echo at a given instant can be estimated by using independent signals from this one region. This is accomplished by varying the frequency of the emitted radiation. For a square wave, or a wave symmetrical about its center point, complete independence can be attained by appropriate variations of frequency. For an arbitrarily shaped wave, provided its intensity variation is not too drastic or rapid, a high degree of independence can be obtained by

varying the frequency by any amount larger than the amount necessary to add another complete wave length or two to an emitted signal of constant total length.

REFERENCES

1. MARSHALL, J. S. and HITSCHFELD, W.   Can. J. Phys. 31: 962.   1953.
2. RAYLEIGH, LORD.   The theory of sound. Vol. I. Dover Publications, New York. 1945. p. 35.
3. SIEGERT, A. J. F.   On the fluctuations in signals returned by many independently moving scatterers. Report 465. Radiation Laboratory, Mass. Inst. of Technology, Publications Office, Cambridge, Mass.   1943.
4. SIEGERT, A. J. F.   Fluctuations in the return signal from random scatterers. Report 773. Radiation Laboratory, Mass. Inst. of Technology, Cambridge, Mass.   1946.

A THEORETICAL INVESTIGATION OF THE NUCLEAR RESO-
NANCE ABSORPTION SPECTRUM OF Al[27] IN SPODUMENE[1]

BY G. LAMARCHE[2] AND G. M. VOLKOFF

ABSTRACT

A theoretical investigation is presented of the energy levels of a nucleus of spin $I = 5/2$, a given magnetic moment μ, and electric quadruple moment eQ, placed in a uniform magnetic field H_0, and a crystalline electrostatic potential ϕ without axial symmetry. The dependence of the energy levels, line frequencies, and transition matrix elements on the dimensionless parameter $R \equiv 4\mu H_0/eQ\phi_{zz}$ is calculated for Al[27] for one orientation of a spodumene crystal in the magnetic field H_0 over the interesting range of the parameter R linking up the pure quadrupole with the Zeeman spectrum. Other orientations of the crystal are discussed briefly.

In a recent paper (7) a summary was given of the various experimental and theoretical studies that have been made to date on the electric quadrupole interaction of non spherically symmetric nuclei (with $I > \frac{1}{2}$) with the electric field gradients existing at the sites of such nuclei in single crystals. It was pointed out that, to date, experiments involving an externally applied static uniform magnetic field H_0 have been performed in two limiting cases: $R \ll 1$ and $R \gg 1$, where $R \equiv 4\mu H_0/eQ\phi_{zz}$ is the ratio of the magnetic interaction energy μH_0 to the quadrupole coupling energy $eQ\phi_{zz}/4$.

A search is being made in this laboratory for a suitable crystal with a field gradient tensor lacking axial symmetry ($\eta \neq 0$) in which the nuclear resonance absorption spectrum might be observed over a sufficiently wide range of values of R to permit an experimental study of the gradual transition from a pure quadrupole spectrum ($R = 0$) to the Zeeman line split into several components by the quadrupole interaction ($R \gg 1$). Experimental data are available in Reference (5) on the quadrupole coupling constant of Al[27] in LiAl(SiO3)2 (spodumene) and on the properties of the electric field gradient tensor ϕ_{ij} at the Al[27] sites. The expected dependence on R of the frequencies and relative intensities of the nuclear resonance absorption lines of Al[27] in spodumene was calculated for one particular crystal orientation to determine whether this crystal could be used for the proposed experimental study of the transition from the pure quadrupole to the Zeeman spectrum. These calculations are briefly summarized below. An attempt to perform the proposed experiment with spodumene is now in progress.

To study the gross line structure in terms of the number and frequency separation of its components, disregarding the line width of the individual components, we may neglect dipole–dipole interactions, and consider each nucleus as being individually acted upon by the given H_0 and the given crystalline field gradient ϕ_{ij}. The Hamiltonian then consists of two parts:

[1]
$$\mathfrak{H} = \mathfrak{H}_Q + \mathfrak{H}_Z.$$

Here $\mathfrak{H}_Q$, the part due to the quadrupole coupling, is given (Refs. (2) and (3)) by

[2]
$$\mathfrak{H}_Q = \frac{eQ\phi_{zz}}{4I(2I-1)}\left[(3\mathbf{I}_z^2 - \mathbf{I}^2) + (\mathbf{I}_x^2 - \mathbf{I}_y^2)\eta\right]$$

where x, y, z are the principal axes of ϕ_{ij} and η is the asymmetry parameter defined as

[3]
$$\eta \equiv (\phi_{xx} - \phi_{yy})/\phi_{zz}.$$

The Zeeman energy $\mathfrak{H}_Z$ is given by:

[4]
$$\mathfrak{H}_Z = -g\beta\mathbf{I}\cdot\mathbf{H}_0.$$

The problem consists in solving the secular determinant of the operator $\mathfrak{H}$

[5]
$$|\mathfrak{H}_{mm'} - E\delta_{mm'}| = 0$$

for the energy levels, and in computing the frequencies and relative probabilities of transition between them. We first of all note that the problem is considerably simplified if H_0 coincides with one of the principal axes of ϕ_{ij}.

When the quadrupole energy matrix $\mathfrak{H}_Q$ is written down in a representation in which the x, y, z axes, to which $\mathbf{I}_x$, $\mathbf{I}_y$, and $\mathbf{I}_z$ are referred, coincide with the principal axes of ϕ_{ij}, as is done above, the only nonvanishing matrix elements, as shown in Ref. (3), are those for which $|m - m'| = 0$ or 2. In a coordinate system that does not coincide with the principal axes, the $|m - m'| = 1$ matrix elements also do not vanish (Refs. 1 and 6).

The magnetic matrix $\mathfrak{H}_Z$ has only diagonal elements if the axis of quantization of spin coincides with the direction of the magnetic field H_0. Otherwise it has nonvanishing $|m - m'| = 1$ matrix elements as well.

Hence if, and only if, H_0 coincides with one of the principal axes of ϕ_{ij} can the $|m - m'| = 1$ matrix elements of both interactions be made to vanish simultaneously. With this choice of the H_0 direction, the only nonvanishing terms of the matrix $\mathfrak{H}$ are those for which $|m - m'| = 0$ or 2. For half integral I the determinant is then readily factored into two determinants each of which leads to a characteristic equation of degree $I + \frac{1}{2}$. The eigenstates defined by each of these two subdeterminants are linear combinations of one of two subsets into which the functions ψ_m which diagonalize $\mathbf{I}_z$ may be subdivided. One set includes ψ_m with $m = \frac{1}{2} + 2n$, and the other with $m = -\frac{1}{2} + 2n$, where n is an integer.

In the most general case when H_0 does not coincide with any of the principal axes of ϕ_{ij}, there will always be the $|m - m'| = 1$ nonvanishing matrix elements present, no matter what representation is used. In this case the determinant does not factor easily, the characteristic equation obtained from equation [5] is of degree $2I + 1$, and each eigenstate may involve all the ψ_m.

To obtain information useful in planning experiments involving Al^{27} in spodumene, we choose $I = 5/2$, $\eta = 0.95$,* and treat the case when H_0 coincides with the z principal axis of ϕ_{ij}. The sixth-order secular determinant then

*The numerical values used in the present paper were taken from the preliminary communication on Al^{27} in spodumene Ref. (4), and differ slightly from those of Ref. (5).

gives rise to two cubic secular equations whose coefficients involve the para-
meters R and η. These two equations are:

[6]
$$-\lambda^3 \mp \frac{3R}{20}\lambda^2 + \frac{1}{400}(13R^2 \mp 24R + 7\eta^2 + 21)\lambda$$
$$+ \frac{1}{1600}[\pm 3R^3 + 8R^2 \mp 15R \pm 3R\eta^2 + 4(1 - \eta^2)] = 0$$

where $\lambda \equiv E/eQ\phi_{zz}$. We have plotted in Fig. 1 λ as a function of R for $0 \leqslant R \leqslant 4$. The λ_i^L and λ_i^M ($i = 1, 2, 3$) are respectively the solutions of equation [6] corresponding to all upper and all lower signs.* The corresponding eigenstates
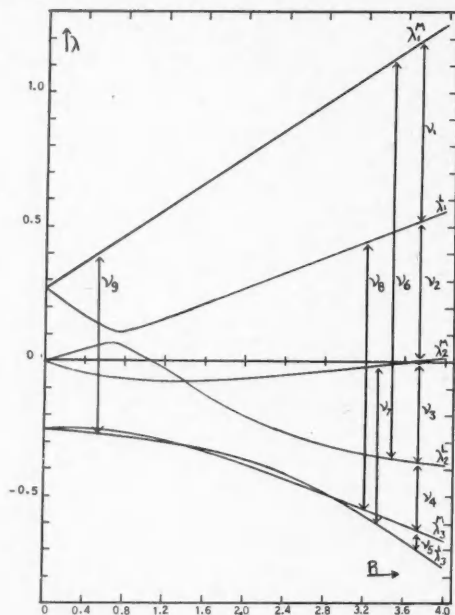
FIG. 1.   Energy values for $I = 5/2$, $\eta = 0.95$ in terms of $\lambda \equiv E/eQ\phi_{zz}$ as a function of $R \equiv 4\mu H_0/eQ\phi_{zz}$, for $0 \leqslant R \leqslant 4$. H_0 is along the z principal axis of ϕ_{ij}. The arrows represent the possible absorption lines, and are numbered from 1 to 9, the first five being the Zeeman transitions for $R \gg 1$.

are of two classes as mentioned above: class L involving ψ_m with $m = -\frac{3}{2}, \frac{1}{2}, \frac{5}{2}$, and class M with $m = -\frac{5}{2}, -\frac{1}{2}, \frac{3}{2}$.

Transitions produced by an r–f. magnetic field placed at right angles to H_0 are only possible between levels of different classes ($\Delta m = \pm 1$). Their frequencies are easily calculated by taking the difference between the eigenvalues λ of Fig. 1 multiplied by the known quadrupole coupling constant of Al^{27} in spodumene $eQ\phi_{zz}/h = 2.960 \pm 0.010$ Mc./sec. They are plotted (in Mc./sec.) in Fig. 2 as a function of R for $0 \leqslant R \leqslant 4$ (or of $H_0 = ReQ\phi_{zz}/4\mu$).

*For large values of R these solutions agree with those obtained by the perturbation theory of Ref. (7).
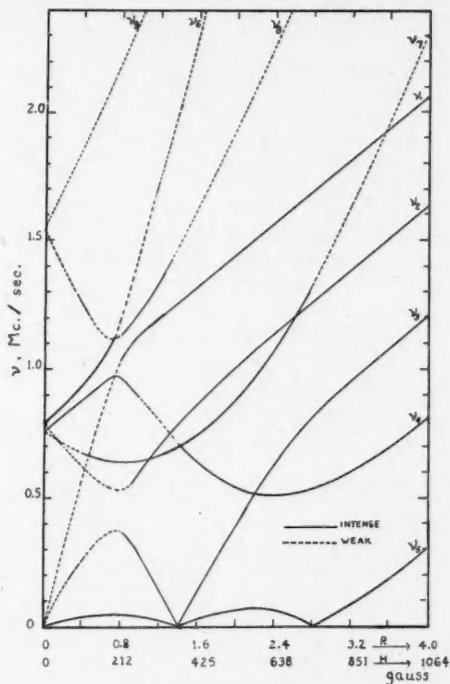
FIG. 2. Transition frequencies ν (in Mc./sec.) as a function of R (or of $H_0 = ReQ\phi_{zz}/4\mu$). Lines have been labelled intense or weak in accordance with relative values of the squares of matrix elements being greater or smaller than unity on the arbitrary scale used in Fig. 3.

Finally, the relative transition probabilities are determined largely by the squares of the absolute value of the matrix elements of the perturbing operator which is proportional to $(\mathbf{I}_x + i\mathbf{I}_y)$. Since the elements of this operator are well known in the ψ_m representation, and since the eigenstates of our problem can be expressed on solving the secular determinant as known linear combinations of ψ_m, the required matrix elements may be easily computed. The squares of these matrix elements are plotted in Fig. 3 in arbitrary units as a function of R. In Fig. 3a we have the squares of the matrix elements corresponding to the Zeeman lines, i.e. transitions between levels which are adjacent for $R \gg 1$, while the others, the so-called "forbidden lines", are given in Fig. 3b.

From these graphs we may note the following. At $H_0 = 0$ the pure quadrupole spectrum will consist of two strong lines of almost the same frequency (0.789 and 0.758 Mc./sec.) plus a much weaker line at the sum of these two frequencies (this line would be absent if $\eta = 0$). As H_0 increases, the spectrum gradually changes as shown in Fig. 2 until eventually the Zeeman line, split into five components by the quadrupole interaction, is established. At intermediate fields (around 260 gauss) there is apparently a chance of finding
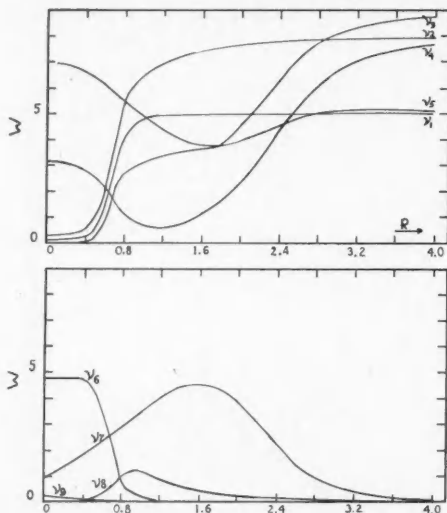
FIG. 3. Squares of the matrix elements of the perturbing operator (in arbitrary units) as a function of $R = 4\mu H_0/eQ\phi_{zz}$.

"extra lines" as shown in Fig. 2 (ν_8 for $200 < H_0 < 400$ gauss and ν_7 for $100 < H_0 < 750$ gauss).

If H_0 coincides with one of the other two principal axes of ϕ_{ij}, the solution of the problem is in principle the same, and differs only in numerical details. The axes can be relabelled, and η and ϕ_{zz} conveniently redefined.

In the more general case where H_0 does not coincide with any of the principal axes of ϕ_{ij}, transitions between any pair of the six levels become possible in principle, so that 15 lines may be expected, although some may again be of too low intensity or too low a frequency to be observable.

REFERENCES

1. BERSOHN, R. J. Chem. Phys. 20: 1505. 1952.
2. DEHMELT, H. G., and KRUGER, H. Z. Physik, 129: 401. 1951.
3. KRUGER, H. Z. Physik, 130: 371. 1951.
4. PETCH, H. E., VOLKOFF, G. M., and CRANNA, N. G. Phys. Rev. 88: 1201. 1952.
5. PETCH, H. E., CRANNA, N. G., and VOLKOFF, G. M. Can. J. Phys. 31: 837. 1953.
6. POUND, R. V. Phys. Rev. 79: 685. 1950.
7. VOLKOFF, G. M. Can. J. Phys. 31: 820. 1953.

THE DELAYED CATHODE GLOW PRODUCED IN A NEON DISCHARGE TUBE AT LOW PRESSURE

BY DONALD J. ECKL

When the light output of the absorption tube used in the measurements of the decay of the populations of neon atoms in the $2p^5 3s$ levels, described elsewhere in this journal,* was examined by observing on an oscilloscope the signal voltage produced by a photomultiplier tube, a satellite pulse was observed. This pulse occurred some time after the original light output produced by the excitation voltage across the discharge tube had dropped to zero. When a baffle was placed so that light from the cathode region of the discharge tube could not reach the photomultiplier, the satellite pulse was no longer observed.

Photographs showing the photomultiplier tube output for the excitation pulse and the accompanying satellite are shown in Fig. 1. A curve of the delay,
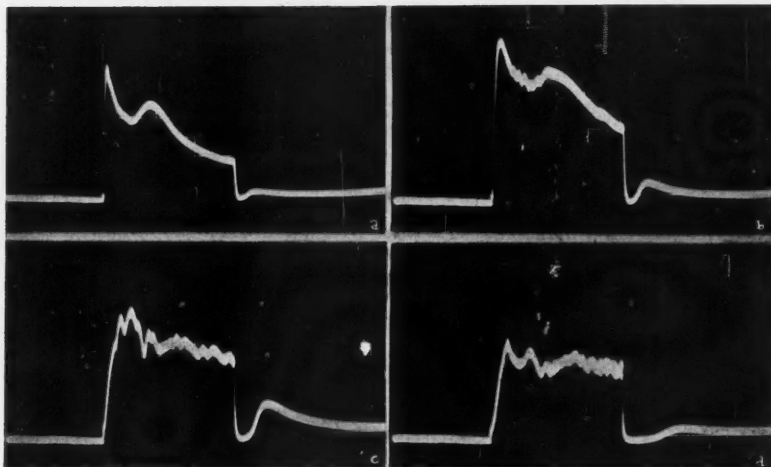
FIG. 1. Light intensity output from absorption tube at various neon pressures obtained with a 931A photomultiplier tube. Duration of pulse is 500 μsec.
  a. Pressure is 2.6 mm. Amplitude is one-half scale of other three figures.
  b. Pressure is 1.9 mm.
  c. Pressure is 1.0 mm.
  d. Pressure is 0.6 mm.

measured as the time between the end of the excitation pulse and the maximum amplitude of the satellite, as a function of pressure is given in Fig. 2 and has the form

$$T = \frac{k}{p} + L, \qquad \begin{aligned} k &= 125 \text{ mm-}\mu\text{sec.} \\ L &= 28 \ \mu\text{sec.} \end{aligned}$$

where T is the delay in microseconds and p is the pressure in millimeters.

* *Can. J. Phys. 31:804. 1953.*
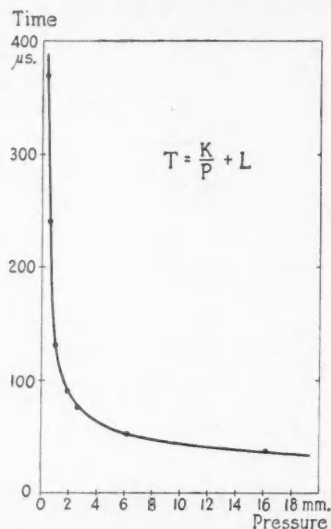
FIG. 2.   Cathode glow delay against pressure.

A spectroscopic check of the light from the satellite shows the presence of spectral lines originating from the $2p^5 3p$ levels. Since all electronic levels above the $2p^5 3s$ levels have extremely short lives, the source of such levels associated with the satellite pulse is probably positive ions. The delay then should be associated with the recombination time for such ions in the neighborhood of the cathode. The light in the satellite pulse would represent a source of light from atoms in an essentially field-free region.

INFLUENCE OF STRIATIONS ON THE PLASTIC DEFORMATION OF SINGLE CRYSTALS OF TIN

BY K. A. JACKSON AND B. CHALMERS

In recent years, much work has been done on substructures formed during plastic deformation. The purpose of this note is to set forth some observations on the effect of an existing substructure on a substructure subsequently formed by deformation.

Single crystals (approximately $\frac{1}{4}$ in. $\times$ 1 in. $\times$ 6 in.) of Chempur tin (99.986%) were grown from the melt by a technique previously described (2). The crystals were grown so that the (001) planes were parallel to the top surface of the crystals, and the [110] direction was parallel to the direction of growth. This is the preferred direction of growth for tin, and produces striations (3) running parallel to the axis of the crystal. Fig. 1 is a Laue back-reflection photograph of such a crystal. The orientation difference between striations corresponds to a rotation of the lattice about the specimen axis. The crystals were deformed in tension on a Hounsfield tensometer.

The two planes of maximum resolved shear stress in these crystals approximated to the (100) and (010) planes, which slip lines indicated to have been the active slip planes. The crystals had therefore deformed by conjugate slip. Fig. 2 shows the appearance of the top surface of an etched crystal that had been deformed in this way. The banded structure is typical. Laue back-reflection photographs showed that the bands were regions of different orientation, the orientation difference being a rotation about the C-axis of the lattice in one band with respect to the lattice of an adjacent band. Fig. 3 is a Laue back-reflection photograph of a crystal after deformation, taken at the boundary between two bands. The splitting of the X-ray spots due to striations is a vertical displacement on the photograph corresponding to a rotation about the [110] axis. The additional splitting of the X-ray spots corresponding to a rotation of the lattice about the [001] direction is due to the deformation bands. This orientation difference between the deformation bands increased with increasing deformation. For elongations up to 5% each band deformed homogeneously, shown by the absence of asterism in Laue photographs taken on single bands. For elongations greater than 10%, asterisms in the X-ray photographs showed that the lattice in the bands had become distorted.

The boundaries of the deformation bands followed the striation boundaries wherever possible. This is shown in Fig. 2, taken of a crystal extended 37% to show up the bands. The band boundaries did not change appreciably from their initial positions with increased deformation, but the greater orientation difference between the bands makes them more readily seen and photographed. Fig. 4 is a photomicrograph showing the coincidence of a deformation band boundary and a striation boundary. In many cases the deformation bands were larger than the striations, and more than one striation was contained in a single deformation band. The lateral boundaries of the bands were quite jagged, since there were no striation boundaries to follow; and in a crystal

grown so that there was an area free of striations, the deformation bands formed in this region had quite irregular boundaries.

Barrett and Levenson (1) attribute the formation of deformation bands to the operation of different sets of slip systems in different band-shaped regions. The observed orientation difference between bands can be explained in these terms. The two predominant slip planes are the (100) and the (010) planes. Slip on the (100) planes predominates in some bands, and on the (010) planes in the other bands. The local lattice rotation thus produced is such that there is no change in the mean orientation of the specimen as a whole, a condition which is imposed by the grips on the tensile machine.

The striations running parallel to the crystal axis are attributed to arrays of dislocations formed during solidification from the melt (3). These low angle boundaries will impede the motion of dislocations through the crystal. The dislocation can pass through these boundaries in some cases, and so more than one striation can be contained in a single deformation band. Since the deformation bands will form independently of the existence of available striations, the presence of striation boundaries will constitute a natural place for the deformation band boundaries to form. Thus, in deformed striated crystals, most of the deformation band boundaries coincide with the striation boundaries.

1. BARRETT, C. S. and LEVENSON, L. H.   Trans. Am. Inst. Mining Met. Engrs. 135: 327.
        1939; 137: 112.   1940.
2. CHALMERS, B.   Can. J. Phys. 31: 132.   1953.
3. TEGHTSOONIAN, E. and CHALMERS, B.   Can. J. Phys. 29: 30.   1951; 30: 388.   1952.

DEPARTMENT OF METALLURGICAL ENGINEERING,
UNIVERSITY OF TORONTO,
TORONTO, ONT.

PLATE I
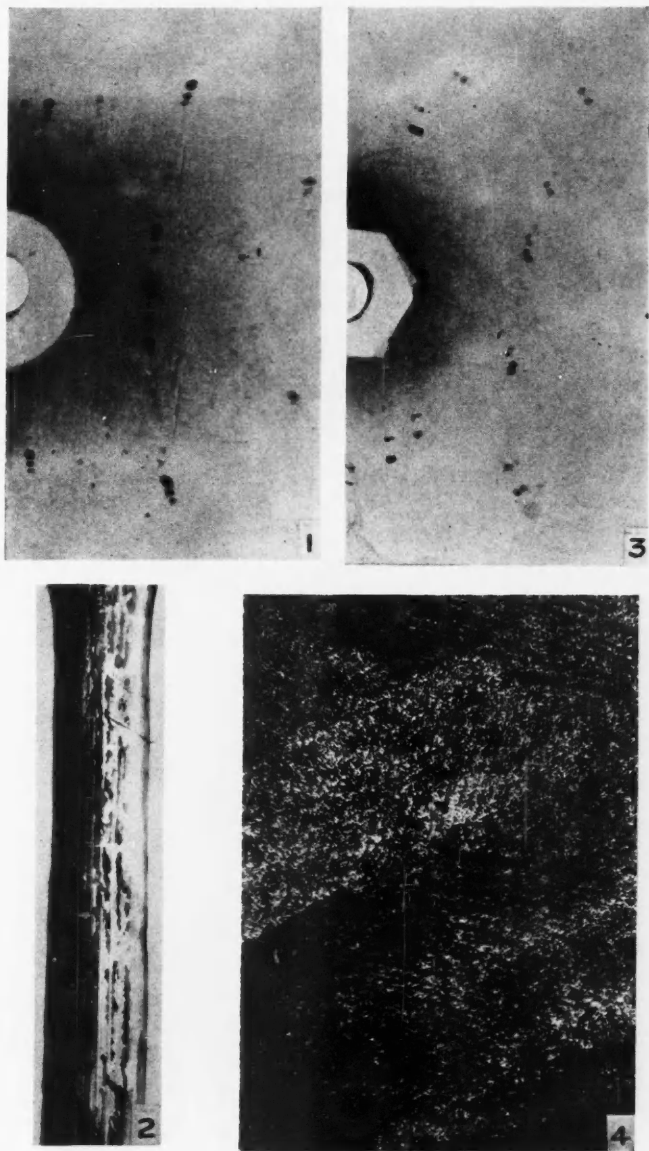
FIG. 1. Laue back-reflection X-ray photograph of a striated crystal.

FIG. 2. A deformed and subsequently etched crystal photographed under oblique illumination, $\times \frac{3}{4}$.

FIG. 3. Laue back-reflection photograph of a deformed crystal showing orientation difference between deformation bands.

FIG. 4. Photomicrograph of an etched crystal showing the coincidence of a striation boundary and a deformation band boundary, $\times 500$.

THE CALCULATION OF VIBRATIONAL TRANSITION PROBABILITIES OF DIATOMIC MOLECULES

By R. W. Nicholls, W. R. Jarmain, and P. A. Fraser

The intensity of a band of a diatomic molecular band system is controlled in part by the square of an integral of the form (2)

$$\int \psi_1^{(v')} R_e \, \psi_2^{(v'')} \, dr \equiv (v', R_e \, v'').$$

$\psi_1^{(v')}$ and $\psi_2^{(v'')}$ are vibrational wave functions and $R_e(r)$ is the electronic transition integral. The form of $R_e(r)$ is unknown in general and as a first approximation is assumed to be slowly varying in the important range of r so that it may be replaced by an average value, $\bar{R}_e$, for the whole band system and may thus be taken outside the integrals; $(v', R_e \, v'') \simeq \bar{R}_e(v', v'')$. Relative approximate vibrational transition probabilities, $p(v', v'')$, may then be defined by

$$p(v', v'') \equiv (v', v'')^2.$$

Accordingly, an extended numerical and analytic study of integrals of the form (v', v'') has recently been made and applied to molecular transitions of astrophysical interest. The integrals $(v', r \, v'')$ and $(v', r^2 \, v'')$ have also been studied for eventual use with experimental intensity measurements in the determination of a linear or quadratic form for $R_e(r)$.

Since the Morse potential combines the merits of relative accuracy and relative simplicity, the principal work up to the present has been with vibrational wave functions in Morse potentials. In the Morse potential $U_i(r) = D_i[1 - \exp{-\alpha_i(r - r_{ei})}]^2$, appropriate to the electronic state i, where the symbols have their conventional meaning (2), the vth normalized vibrational wave function is given by (4)

$$\psi_i^{(v)} = N_i^{(v)} \, (\exp{-\tfrac{1}{2}z_i}) \, z_i^{(K_i - 2v - 1)/2} \, L_{K_i - v - 1}^{K_i - 2v - 1}(z_i)$$

ignoring the phase factor, and the vibrational energy by

$$E_i^{(v)} = (\omega_e)_i(v + \tfrac{1}{2}) - (\omega_e x_e)_i(v + \tfrac{1}{2})^2.$$

$z_i = K_i \exp{-\alpha_i(r - r_{ei})}$, $L_{K_i - v - 1}^{K_i - 2v - 1}(z_i)$ is the generalized Laguerre polynomial of degree v in z_i, and $K_i = (\omega_e)_i/(\omega_e x_e)_i$.

Numerical evaluation of the appropriate exact wave functions and numerical integration of (v', v''), etc., has been performed for the First and Second Positive band systems of nitrogen, and extensive tables obtained. For higher quantum numbers the Laguerre polynomials exhibit much cancellation, and are very difficult to evaluate. A type of recursion relation has been found that relates any one of the polynomials to all those of lower degree. This was used since the excessive cancellation was thus avoided. The relation is as follows, where $L_v(z) \equiv L_{K-v-1}^{K-2v-1}(z)$:

$$L_v(z) = [z - (K - 2v)] \, L_{v-1}(z)$$
$$- (v - 1)(K - 2v) \sum_{k=2}^{v} \frac{(2k - 2)!}{k!(k - 1)} \binom{v - 2}{k - 2} L_{v-k}(z).$$

The numerical work, even with this form of recursion relation, is long and tedious.

Consequently an approximation was sought and one has been found that allows analytic evaluation of the overlap and other integrals, and which does not break down for higher quantum numbers, as would previous approximations (5, 1). Essentially, the approximation involves a slight change in description of the original vibrational states that allows analytic integration. The α_1 and α_2 of the Morse potentials appropriate to the electronic states between which the transition takes place are each replaced by a mean α, say $\alpha = (\alpha_1 + \alpha_2)/2$, and compensating adjustments made in all constants depending on α_1 and α_2. Thus normalization and consistency of approximation is maintained throughout. This change in description involves a small distortion of the potentials and a second order change in the vibrational energy, and means that the new potentials and wave functions are probably as adequate as the originals for calculation of approximate transition probabilities, bearing in mind that the Morse potential is not the 'true' potential.

A working rule, derived partly from theory and partly from experience, indicates that the maximum absolute difference between the values of an overlap integral calculated using this approximation and by numerical methods is roughly given by $\frac{1}{5} \mid \delta\alpha/\alpha \mid$, where $\delta\alpha = (\alpha_1 - \alpha_2)/2$, when the overlap of the potentials is considerable, and by an even smaller fraction of $\mid \delta\alpha/\alpha \mid$ when the overlap is small. This indicates clearly the applicability of the approximation to a particular transition, and inspection of tables of molecular data (2) shows that the method may be widely used. When not strictly applicable, the approximation will at least lead to correct trends. An improvement designed for such cases, i.e., $\mid \delta\alpha/\alpha \mid > 5\%$, has given results in excellent agreement with results of numerical integration. This improvement involves a horizontal shift of the 'new' potentials to bring the 'new' wave functions approximately into line with the 'old' wave functions, a different shift being necessary for each band. This technique approximately doubles the work, but the method is still much more rapid than the numerical method.

The only limiting factor on the extent of a table of $(v', v'')^2$ calculated using this approximation is the digit capacity of the desk calculator available, because of the wholesale cancellation that arises in evaluation of the formulae, the cancellation increasing with $(v' + v'')$. This cancellation is intrinsic in the problem, and can be traced back to the Laguerre polynomials. For example, using a 10 digit capacity calculator, one may calculate (v', v'') for values of $(v' + v'') \leqslant 6$ for the First Positive system of nitrogen, while for the Vegard-Kaplan bands, the table may be extended to $(v' + v'') \leqslant 9$, the cancellation being less severe owing to the smallness of the $(0, 0)$ overlap. Formulae have been derived for bands which have one of the quantum numbers equal to 0, 1, 2, or 3, in which the cancellation is carried out algebraically, the remainder exhibiting no cancellation. Work is continuing on these 'remainder' formulae for other quantum numbers since their use allows great extension of the tables.

A sample formula, resulting from the approximation made, before the

cancellation has been algebraically carried out, is shown below mainly to demonstrate the type of numerical work involved in final evaluation. For example,

$$\frac{(0,2)}{(0,0)} = \frac{N_2^{(2)}}{N_2^{(0)}}\left\{1 - 2\,\rho_2\,\frac{(K_2-3)}{(K-2)} + \rho_2{}^2\,\frac{(K_2-3)(K_2-4)}{(K-2)(K-3)}\right\},$$

with

$$(0,0) = \left(\frac{1}{\rho_1}\right)^{\frac{1}{2}(K_1-1)}\left(\frac{1}{\rho_2}\right)^{\frac{1}{2}(K_2-1)}\frac{\Gamma(K-1)}{\sqrt{[\Gamma(K_1-1)\,\Gamma(K_2-1)]}}.$$

Taking the ratio of (v', v'') to $(0, 0)$ provides a great simplification in computation; the only gamma functions that have to be evaluated are then those in the $(0, 0)$ integral. Even this can be avoided. Similar formulae give $(v', r\,v'')/(0, r\,0)$ and $(v', r^2\,v'')/(0, r^2\,0)$.

TABLE I

N_2, $B^3\Pi_g \rightarrow A^3\Sigma_u^+$, FIRST POSITIVE

$p(v', v'') = (v', v'')^2$

v' \ v''	0	1	2
0	$.33_7$ $(.34_0)$	$.32_4$ $(.32_3)$	$.19_0$ $(.19_0)$
1	$.40_6$ $(.40_6)$	$.00_3$ $(.00_2)$	$.10_2$ $(.10_3)$
2	$.19_8$ $(.20_0)$	$.20_9$ $(.21_2)$	$.11_5$ $(.11_3)$

p-Values (i.e., $(v', v'')^2$) have been computed using this approximation for 11 transitions some of which are in process of publication (3). In the table are shown a few such p-values for the First Positive System of N_2, $B^3\Pi_g \rightarrow A^3\Sigma_u^+$. This table contains but a portion of the triangle of 28 bands, $(v' + v'') \leqslant 6$, that have been obtained by this method, as mentioned above. Values obtained by numerical integration of 'exact' wave functions are also shown, for comparison, in parentheses. Agreement is not always so completely satisfactory, but is most often completely adequate for the purposes to which these numbers are put. A program of computing p-values by this approximate and rapid method for many transitions of astrophysical interest is now under way (3), the justification being the validity of the approximation as shown in those transitions for which comparison with numerical integrations has been possible. Molecules so far studied are: N_2, N_2^+, NO, O_2^+, CN, O_2, and C_2; and those under course of study include: OH, CH, CO, and CO^+.

1. BOUIGUE, R.   Compt. rend. 232: 2401.   1951.
2. HERZBERG, G.   Spectra of diatomic molecules.   D. Van Nostrand Co., Inc., New York.
      1950.
3. JARMAIN, W. R., FRASER, P. A. and NICHOLLS, R. W.   Astrophys. J.   In press.
4. MORSE, P.   Phys. Rev. 34: 57.   1929.
5. WU, TA-YOU.   Proc. Phys. Soc. (London), A, 65: 965.   1952.

DEPARTMENT OF PHYSICS,
UNIVERSITY OF WESTERN ONTARIO,
LONDON, ONTARIO.

"Phosphorescent" Effect in Lead Selenide

During recent work on the photoconductive properties of lead selenide, it was observed that this substance exhibited a very strong "phosphorescent" effect when cooled to liquid air temperatures. The lead selenide was obtained in the form of a thin layer by evaporating it *in vacuo* onto the end of the inner wall of a small Dewar. Aquadag electrodes were previously painted on this surface so that only a small area 8×1 mm.^{2} was used for the experiments. Connections to the electrodes were made by means of 1 mm. diameter tungsten leads which were brought out at the top of the Dewar. The outer wall consisted of a periclase window opposite the electrodes, and a graded seal 1 in. in diameter. Periclase is transparent to infrared radiation out to 8 microns and may be sealed directly to soft glass (3). The graded seal was used for joining this soft glass to the pyrex glass at the top of the Dewar.

Fig. 1 gives the results of measurements on the conductivity of the layer plotted on a log scale against the inverse of the temperature. To obtain the various temperatures a small quantity of mercury was placed in the Dewar. The mercury was then frozen using liquid air to 90° K., and then gradually allowed to warm up by means of a small air jet. The temperature was measured using a copper–constantan thermocouple immersed in the mercury.
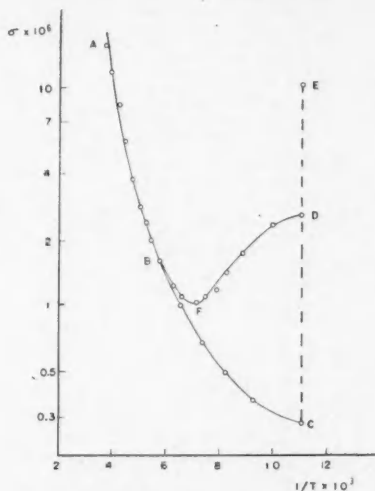
Fig. 1. Conductivity of lead selenide.

The curve ABC is that normally obtained for a semiconductor such as lead selenide, the point C corresponding to 90° K. The first part of the curve AB is linear, conforming to the usual equation $\sigma = \sigma_0 \exp{-\epsilon/2KT}$. The curved part BC may be ascribed to impurities and photoconductive effects due to room temperature radiation (2). On illuminating the layer with a small tungsten lamp the conductivity changes to the point E. If this illumination is now removed the conductivity returns to the point D, and not to C as would be expected. Allowing the layer to warm up gradually, the conductivity curve follows DFB, joining the original curve at B, and on recooling the conductivity retraces the curve BC. Along FD, lead selenide there-fore behaves as a metal. Keeping the temperature constant at 90° K. the conductivity is observed to remain at D for at least one hour without any noticeable change. This effect does not appear to depend on the amount of impurities present since it has been observed in layers of very different sensitivity. A similar effect has been observed for lead sulphide by Chasmar

1023

and Gibson (1) who ascribed it as due to transitions to metastable levels by the photoelectron s. The curve DFB shows the way in which these trapped electrons are thermally released, if this is assumed to be the correct interpretation of this effect.
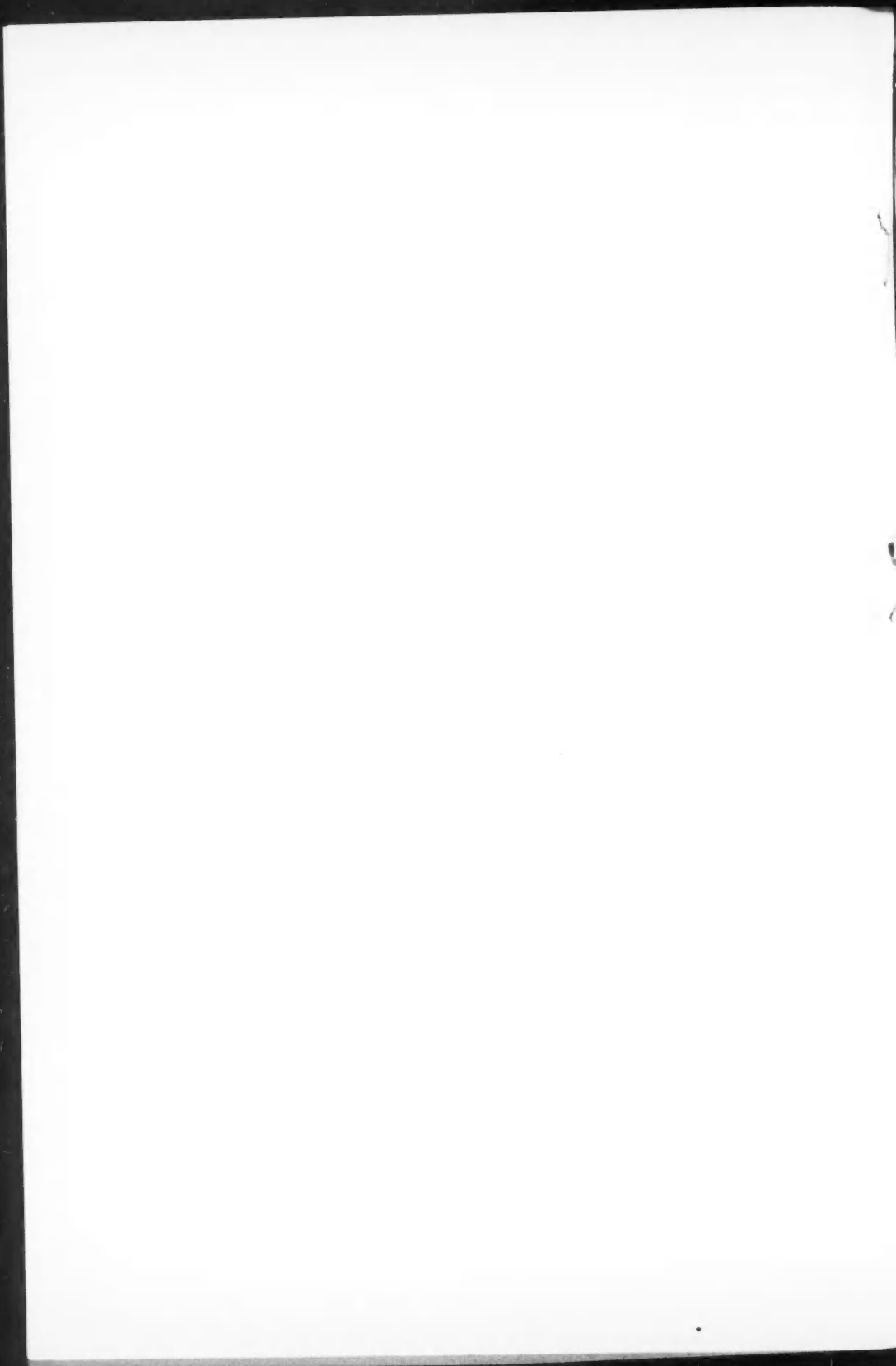
1. CHASMAR, R. P. and GIBSON, A. F.   Proc. Phys. Soc. (London), B, 64: 595.   1951.
2. WATTS, B. N.   Proc. Phys. Soc. (London), A, 62: 456.   1949.
3. YOUNG, A. S.   J. Sci. Instr. 28: 207.   1951.

RECEIVED JULY 20, 1953.
DEPARTMENT OF PHYSICS,   P. A. LEE
UNIVERSITY OF BRITISH COLUMBIA,
VANCOUVER, B.C.

CANADIAN JOURNAL OF PHYSICS

Notice to Contributors

GENERAL: Manuscripts should be typewritten, double spaced, and the **original and one extra copy** submitted. Style, arrangement, spelling, and abbreviations should conform to the usage of this Journal. Names of all simple compounds, rather than their formulas, should be used in the text. Greek letters or unusual signs should be written plainly or explained by marginal notes. Superscripts and subscripts must be legible and carefully placed. Manuscripts should be carefully checked before being submitted, to reduce the need for changes after the type has been set. If authors require changes to be made after the type is set, they will be charged for changes that are considered to be excessive. **All pages, whether text, figures, or tables, should be numbered.**

ABSTRACT: **An abstract of not more than about 200 words, indicating the scope of the work and the principal findings, is required.**

ILLUSTRATIONS:

(i) *Line Drawings:* All lines should be of sufficient thickness to reproduce well. Drawings should be carefully made with India ink on white drawing paper, blue tracing linen, or co-ordinate paper **ruled in blue only**; any co-ordinate lines that are to appear in the reproduction should be ruled in black ink. Paper ruled in **green, yellow, or red should not be used** unless it is desired to have all the co-ordinate lines show. Lettering and numerals should be neatly done in India ink preferably with a stencil (**do not use typewriting**) and be of such size that they will be legible and not less than one millimeter in height when reproduced in a cut three inches wide. All experimental points should be carefully drawn with instruments. Illustrations need not be more than two or three times the size of the desired reproduction, but the ratio of height to width should conform with that of the type page. **The original drawings and one set of small but clear photographic copies are to be submitted.**

(ii) *Photographs:* Prints should be made on glossy paper, with strong contrasts; they should be trimmed to remove all extraneous material so that essential features only are shown. Photographs should be submitted **in duplicate**; if they are to be reproduced in groups, one set should be so arranged and mounted on cardboard with rubber cement; the duplicate set should be unmounted.

(iii) *General:* The author's name, title of paper, and figure number should **be written in the lower left hand corner (outside the illustration proper) of the sheets on which the illustrations appear.** Captions should not be written on the illustrations, but typed together at the end of the manuscript. All figures (including each figure of the plates) should be numbered consecutively from 1 up (arabic numerals). **Each figure should be referred to in the text.** If authors desire to alter a cut, they will be charged for the new cut.

TABLES: Each table should be typed on a separate sheet. Titles should be given for all tables, which should be numbered in roman numerals. Column heads should be brief and textual matter in tables confined to a minimum. **Each table should be referred to in the text.**

REFERENCES: **These should be listed alphabetically by authors' names, numbered in that order, and placed at the end of the paper.** The form of literature citation should be that used in this Journal. **Titles of papers should not be given.** The first page only of the references cited should be given. **All citations should be checked with the original articles.** Each citation should be referred to in the text by means of the key number.

REPRINTS: A total of 50 reprints of each paper, without covers, are supplied free to the authors. Additional reprints will be supplied according to a prescribed schedule of charges. On request, covers can be supplied at cost.

Approximate charges for reprints may be calculated from the number of printed pages, obtained by multiplying by 0.6 the number of manuscript pages (double-spaced typewritten sheets, $8\frac{1}{2}$ in. by 11 in.) and making allowance for space occupied by line drawings and half-tones (not inserts). The cost per page is tabulated at the back of the reprint request form sent with the galley.

Contents